2008

Interfacial reactions between Sn-3.0Ag-0.5Cu Solder and Cu-coated PCB coatings

Minerva Mesa Cruz

San Jose State University

INTERFACIAL REACTIONS BETWEEN Sn-3.0Ag-0.5Cu SOLDER AND Cu-COATED PCB COATINGS

A Thesis

Presented to

The Faculty of the Department of Chemical and Materials Engineering

San Jose State University

In Partial Fulfillment

of the Requirements for the Degree

Master of Science

by

Minerva Mesa Cruz

May 2008

SAN JOSE STATE UNIVERSITY

Interfacial Reactions Between Sn-3.0Ag-0.5Cu Solder and Cu-Coated PCB Coatings

By Minerva Mesa Cruz

APPROVED FOR THE DEPARTMENT OF CHEMICAL

AND MATERIALS ENGINEERING

Guna Selvaduray — 4/4/08

Dr. Guna S. Selvaduray — Date

Fred Barez — 4/4/08

Dr. Fred Barez — Date

Russell T. Winslow — 4/4/08

Mr. Russell T. Winslow, Six Sigma — Date

APPROVED FOR THE UNIVERSITY

Rhea I. Williamson — 04/30/08

Date

ABSTRACT

INTERFACIAL REACTIONS BETWEEN Sn-3.0Ag-0.5Cu SOLDER AND Cu-COATED PCB COATINGS

by Minerva Mesa Cruz

The interfacial reactions that form between Sn-3.0Ag-0.5Cu solder and Immersion Silver (ImAg), Electroless Nickel/Immersion Gold (ENIG), and Organic Solderability Preservative (OSP) coatings on Cu pads of printed circuit boards after reflow and aging, were investigated. Bonding between the solder ball and Cu pad was characterized by ball shear test. Reflow was done at a peak temperature of 240°C for 62 seconds above liquidus, and aging at 150°C for 5, 10, 20, and 30 days. Metallography and SEM analysis revealed scallop-like Cu_6Sn_5 intermetallic compounds for the ImAg and OSP-coated specimens, while scallop-like $(Cu,Ni)_6Sn_5$ IMCs were seen for ENIG-coated specimens after reflow. Cu_3Sn and $(Cu,Ni)_3Sn$ IMC layers were detected after 20 days of aging. Ball shear test results varied for each coating type. While there was no change in shear strength for the ImAg-coated specimens, a 15% linear decrease for the ENIG and an asymptotic decrease for the OSP-coated specimens were found.

ACKNOWLEDGEMENTS

The author wishes to thank her advisor, Dr. Guna Selvaduray, for his support, guidance, and perseverance throughout her thesis process. The author is also grateful to her reading committee members, Dr. Fred Barez from the Department of Mechanical and Aerospace Engineering, SJSU, for his valuable inputs and Mr. Russell Winslow, Founder and President of Six Sigma, for his technical guidance and mentoring, and for providing the facilities needed for the completion of this research.

The author wishes to express her gratitude to her family (Ma, Papang, Dad, and Auntie) for their continued support. And finally, the author acknowledges Ron Bulanadi for his unending support and encouragement throughout this process.

TABLE OF CONTENTS

LIST OF FIGURES

LIST OF TABLES

CHAPTER 1

INTRODUCTION

Soldering plays a very important role in the interconnection and assembly of electronic components. Sn-Pb solders have historically been used for metal bonding in microelectronics packaging because of their ease of handling, low melting temperature, good wetting on commonly-used substrates, good ductility and workability, and low cost [1]. However, due to the toxicity of lead, environmental regulations forbid its further use in electronic packaging as well as in other applications, especially in Europe [2]. This has led to the research and development of lead-free solders in Japan and the United States. The need for an advanced soldering technology with processing temperatures close to that of Sn-Pb, and capable of fine pitch connection processes, with pitch < 0.5 mm, as well as the customers' desire for "green" electronic products has contributed to the significant efforts to further the research in lead-free solders and their usability [3].

The European Union officially set July 1, 2006 as the date for the implementation of the Directive on the Restriction of Hazardous Substances (RoHS), which resulted in the ban of the use of six hazardous substances in electrical and electronic equipment products (both domestic and export), namely, cadmium (Cd), hexavalent chromium (Cr (VI)), lead (Pb), mercury (Hg), polybrominated biphenyls (PBBs), and polybrominated diphenyl ethers (PBDEs) [4]. As a result, several lead-free solders have already been proposed and are being used as replacements for Sn-Pb solders. The performance of these solders need to be at par with their lead-containing counterparts and must satisfy

several requirements, such as good wetting, process-suitable melting temperature, good mechanical, chemical, metallurgical and electrical properties, good resistance to thermal fatigue and corrosion, easy availability, and low cost [5]. All of the proposed alternatives to the Sn-Pb solders, at this time, consist of tin-based alloys that have more than 90 weight % tin, in combination with various amounts of copper, silver, bismuth, antimony or zinc [6]. Some of the major lead-free solder candidates are Sn-based binary alloys (Sn-Ag), ternary alloys (Sn-Ag-Cu), and quaternary alloys (Sn-Ag-Cu-Sb).

During the conversion to these lead-free solders, it is very important to fully understand the interaction of the solder with the existing assembly materials and technology. In particular, it is crucial that the correlations among diffusion, interfacial reactions, and solder joint reliability be thoroughly understood [6]. Several researchers have stated that interfacial reaction products between substrates and solder alloys, such as intermetallic compounds (IMCs), have a major effect on the mechanical properties and reliability of the solder joints, owing to the brittle nature of the intermetallic compounds [1, 6-8]. Others have found that the strength of these lead-free solders decreases with increasing intermetallic compound layer thickness [6-8], although conflicting IMC thickness and solder strengths have been reported, with no resolution to date.

It took decades for researchers to study and understand the metallurgical, physical, mechanical, and chemical behavior of the binary Sn-Pb solders. In contrast, many of the properties of lead-free solders are still unknown. In particular, the behavior of these solders when in contact with other materials, such as the exposed metallization of the substrates, are still not well understood. Some of the major interfacial reactions

include dissolution of the base metal, formation of intermetallic compounds, spalling, and voiding [9-12]. To ensure that the best-quality electronic equipment with high reliability are used by consumers, it is crucial to have a better understanding of the reactions that control or affect the reliability of the solder/substrate interfaces [13].

In Chapter 2, the background of Sn-Ag-Cu solders and a general overview of the interfacial reactions that form between these solders and different coated substrates are presented. In Chapter 3, the research objectives are discussed. In Chapter 4, the experimental methodology utilized in this research is described and explained. Chapters 5 and 6 contain the results obtained in this research and the discussion of these results. The conclusions are stated in Chapter 7, and Chapter 8 contains recommendations for future work.

CHAPTER 2

LITERATURE REVIEW

Solder alloy alternatives must satisfy the following main requirements: (a) a low melting point to avoid thermal damage to the assembly components during processing conditions, (b) a strong bond, including good wettability, between the solder and the base/substrate material, (c) adequate supply, (d) low cost, and most important, (e) non-toxic [3]. They also need to be highly reliable, and must meet the expected levels of mechanical performance [14]. None of the Pb-free solder alloys currently available can meet all the requirements, especially if the liquidus temperature is required to be close to that of eutectic Sn-Pb solder, which is 183°C [3].

Some of the leading solder alloy candidates are the Sn-Ag, Sn-Cu, and Sn-Ag-Cu alloys. However, these alloys also have their issues, such as the possible formation of excessive intermetallic compounds between the solder and the substrate, dissolution of the base metal, spalling, voiding, and whiskering, all of which can affect the long-term reliability of the solder joint [15]. The search for the perfect solder alloy, one that will satisfy commercial, environmental, processing, and reliability requirements is still ongoing.

2.1 Interfacial Reactions and Morphology of Pb-free Solders

There are several lead-free solder alloy candidates in the market, most of which are binary, or ternary alloys with some quaternary alloys. However, since an increase in the ternary or quaternary elements in the alloy means an increase in cost, especially for

alloys with indium, the National Center for Manufacturing Sciences (NCMS) has recommended that the solders used have a maximum of three elements [16]. Sn-Ag, Sn-Ag-Cu, and Sn-Cu solders have been recommended as promising lead-free solders [17].

2.1.1 Formation of Intermetallic Compounds

Intermetallic compounds (IMCs) are compounds that are formed between two metals. These compounds are usually found at the solder-lead frame interface, at the solder ball-substrate pad interface, or at the solder ball-component interface [18]. Depending on the composition of the materials in contact and the processing conditions employed, different intermetallic compounds are formed. The intermetallic compounds that form between two metallic materials can be predicted by referring to the appropriate binary or ternary phase diagrams. If the ternary phase diagram is not available, they can be inferred from the appropriate binary phase diagram. All the possible IMCs when Sn-Ag-Cu solders are placed in contact with Cu substrates and NiP surface finish or substrates are listed in Table 1. The reaction between Au and the solders was not included since the Au coating on the pad is usually extremely thin (~ 10 nm), and when dissolved into the molten solder during processing is below its solubility limit in Sn. Thus, any Au that is present does not form intermetallic compounds, but rather stays as a solute in the solidified solder alloy.

Table 1. Intermetallic compounds that form between Sn-Ag-Cu solders and Cu and Ni-P substrates.

Solder Composition	Substrate	Intermetallic Compounds
Sn-Ag-Cu	Cu	Cu_6Sn_5, Cu_3Sn, Ag_3Sn
Sn-Ag-Cu	Ni-P	$(Cu,Ni)_6Sn_5$, $(Ni,Cu)_3Sn_4$, Ag_3Sn

2.1.1.1 Intermetallic Compounds between Sn-Ag-Cu Solders and Cu

Copper is the most commonly used conductor due to its good electrical conductivity and wettability by molten solder. Some of the published experimental results on the intermetallic compounds that form between Sn-Ag-Cu solders and Cu substrate are shown in Table 2.

Kim *et al.* [19] found that scallop-type Cu_6Sn_5 phases were found when Sn-3.0Ag-0.5Cu solder was reflowed with Cu at 260°C. However, long, hexagonal faceted Cu_6Sn_5 intermetallic compounds were seen when Sn-3.9Ag-0.6Cu solder was used. Large plate-type Ag_3Sn intermetallics were also found in the interface and in the bulk solder.

Islam *et al.* [20] determined the interfacial reactions between the Cu pad of a 11-13 μm thick flexible BGA substrate and Sn-3.5Ag-0.5Cu solder. The study was conducted using 3 reflow temperatures of 230°C, 240°C, and 250°C, and reflow times of 1 min, 5 min, 10 min, and 20 min for each reflow temperature. Scallop-like Cu_6Sn_5 grains started to form at the solder/substrate interface after reflowing for 1 min at the lowest reflow temperature, and became thicker as the reflow time was increased. Ag-Sn intermetallics were also found at the bulk solder, but the composition was not verified. The Cu_3Sn intermetallic layer was found between the Cu_6Sn_5 and the Cu substrate only

after reflowing at 250°C for 20 min. The total intermetallic layer, Cu_6Sn_5 + Cu_3Sn, increased as the reflow temperature and reflow time were increased.

Table 2. Intermetallic compounds between Sn-Ag-Cu solders and Cu substrate.

Solder Composition	Processing Conditions	IMC(s) Found	Reference
Sn-3.0Ag-0.5Cu	Reflow at 260°C	Scallop-type Cu_6Sn_5	[19]
Sn-3.5Ag-0.5Cu	Reflow at 230°C, 240°C, and 250°C for 1, 5, 10, and 20 min	Scallop-like Cu_6Sn_5 grains	[20]
	Reflow at 250°C for 20 min	Cu_3Sn layer	
Sn-3.5Ag-0.5Cu	Reflow at 230°C for 1, 2, 5, and 10 min	Scallop-like Cu_6Sn_5	[21]
Sn-3.5Ag-0.7Cu	Dipping at 250°C for 15 sec	Pebble-shaped Cu_6Sn_5, needle-shaped Ag_3Sn	[22]
	Aging samples at 150°C for 144 hrs	Cu_3Sn	
Sn-3.5Ag-0.7Cu	Reflow at 230°C for 15 sec	Scallop-like Cu_6Sn_5	[2]
	Aging at 125°C and 150°C for 500 hrs	Cu_3Sn layer at Cu_6Sn_5/Cu interface	
Sn-3.5Ag-0.75Cu	Reflow at 260°C	Round, scallop-like Cu_6Sn_5	[23]
	Aging for several temperatures and days	Layered type Cu_6Sn_5	
Sn-3.9Ag-0.6Cu	Reflow at 260°C	Large plate-type Ag_3Sn in interface and bulk solder and long, hexagonal faceted Cu_6Sn_5	[19]

Sharif and Chan [21] found that only the Cu_6Sn_5 intermetallic layer was formed in the Sn-3.5Ag-0.5Cu solder/Cu substrate interface after reflowing at 230°C for 1, 2, 5, and

10 min. Cu_6Sn_5 intermetallic layers were also found in the bulk solder after reflow for 2 min at 240°C and the authors stated that the amount of Cu_6Sn_5 in the bulk solder is much greater than those at the solder/substrate interface. No Cu_3Sn intermetallic was found.

Chuang and Lin [22] found Cu_6Sn_5 when a 200 μm-thick Cu plate was dipped in Sn-3.5Ag-0.7Cu solder for 15 sec at 250°C. Unlike the scallop morphology usually observed for the Cu_6Sn_5, the Cu_6Sn_5 observed in this case between the solder and the substrate was pebble-shaped. Ag_3Sn needle-like microstructures were also found in the solder matrix, and identified with an electron probe microanalyzer. The Cu_3Sn intermetallic layer was found only after aging the samples for 144 hours at 150°C. This intermetallic layer did not appear at aging temperatures below 120°C and at aging times shorter than 500 hours.

Hirose and his colleagues [2] found scallop-like Cu_6Sn_5 intermetallic compounds when Sn-3.5Ag-0.7Cu solder was reflowed on a Cu sheet at 230°C for 15 sec. The Cu_3Sn intermetallic layer was found in the Cu_6Sn_5/Cu interface when aging was done at 125°C and 150°C for 500 hrs. No Cu_3Sn layer was found for samples that were aged for up to 1500 hrs at 80°C.

When Sn-3.5Ag-0.75Cu solder was reflowed with Cu substrates, round, scallop-type Cu_6Sn_5 intermetallic compounds were found by Yoon and his colleagues, and this changed to a layered morphology after aging at 100°C -200°C for 15 days [23]. The Cu_3Sn intermetallic was absent at all aging time periods at the aging temperature of 100°C. Isothermal aging above 120°C for 15 days revealed the co-existence of Cu_6Sn_5 and Cu_3Sn intermetallics in the solder/substrate interface, with Cu_6Sn_5 near the bulk

solder and the Cu_3Sn near the Cu substrate. For the samples that were aged at 200°C, both of these intermetallics were found at aging times of 3, 6, 15, and 30 days, with the total IMC thickness increasing with increasing aging time. Ag_3Sn particles were also found embedded in the Cu_6Sn_5 intermetallic compound and in the bulk solder. These Ag_3Sn particles became more prevalent in the Cu_6Sn_5 intermetallic as aging time was increased.

The common intermetallic compound that was identified was Cu_6Sn_5, regardless of the solder composition. This intermetallic compound became thicker with increasing reflow temperature and reflow time. The presence of needle-like Ag_3Sn intermetallic compounds in the bulk solder was also a commonality among these investigations. However, there is variation in the detection of the Cu_3Sn IMC layer. In some cases, it was found only when a higher reflow temperature and/or longer reflow time were used. It was also detected after isothermal aging, but only if the aging temperature was above 80°C. However, when Cu_3Sn is detected, it is normally found between the Cu_6Sn_5 intermetallic compound and the Cu substrate. It is worth noting that many investigations do not represent industrial reflow conditions, which are 240°C - 265°C for 60-150 seconds. As such, the interfacial reactions reported in the literature that was reviewed may not be representative of the reactions that would occur if conventional reflow conditions were used.

2.1.1.2 Intermetallic Compounds between Sn-Ag-Cu Solders and Ni

Cu leads and pads are sometimes coated with nickel. It is used as a diffusion barrier between Sn and Cu, owing to its slower reaction rate with liquid Sn compared to

Cu [13]. Shown in Table 3 are the intermetallic compounds that formed between Sn-Ag-Cu and Ni, as identified by other researchers.

Table 3. Intermetallic compounds between Sn-Ag-Cu and Ni.

Solder Composition	Processing Conditions	IMC(s) Found	Reference
Sn-3.0Ag-0.5Cu	Reflow at 243°C for 40 sec	Scallop-like $(Cu,Ni)_6Sn_5$	[24]
	Aging at 85°C for 1000 hrs	Cu_3Sn layer	
Sn-3.5Ag-0.5Cu	Reflow at 260°C for 1 min	$(Cu,Ni)_6Sn_5$ and Ni_3P	[6]
	Reflow at 260°C for 1 min (20 cycles)	Spalling of $(Cu,Ni)_6Sn_5$ and Cu_3Sn layer under Ni_3P layer	
Sn-3.5Ag-0.5Cu	Reflow at 250°C for 5 min	$(Cu,Ni)_6Sn_5$	[17]
	Reflow at 250°C for 120 min	Spalling of $(Cu,Ni)_6Sn_5$ and voiding in the P-rich Ni layer	
Sn-3.5Ag-0.5Cu	Reflow at 250°C for 1 min	$(Cu,Ni)_6Sn_5$	[25]
	12-day aging at 190°C	Transformation of $(Cu,Ni)_6Sn_5$ to $(Ni,Cu)_3Sn_4$	
	16-day aging at 190°C	Ni layer fully consumed; existence of Cu_6Sn_5 and Cu_3Sn IMC	
Sn-3.5Ag-0.7Cu	Dipping at 250°C for 90 sec	Column-shaped and stick-shaped $(Cu,Ni)_6Sn_5$	[26]
Sn-3.8Ag-0.7Cu	Reflow at 240°C for 50 sec	$(Cu,Ni)_6Sn_5$	[27]
	Reflow at 240°C for 50 sec (5 cycles)	Precipitation of $(Ni,Cu)_3Sn_4$ from $(Cu,Ni)_6Sn_5$	
Sn-3.9Ag-×Cu	Dipping at 250°C for 10 min and 25 hrs	$(Cu,Ni)_6Sn_5$ and/or $(Ni,Cu)_3Sn_4$	[28]

Scallop-like $(Cu,Ni)_6Sn_5$ IMCs were found by Sundelin and his colleagues when Sn-3.0Ag-0.5Cu solder pastes were reflowed with ENIG-coated Cu pads, at a reflow peak temperature of 243°C for 40 sec [24]. In the as-reflowed condition, the thickness of these IMCs was between 1 and 2 μm, and were smaller than the Cu_6Sn_5 IMCs that they found when OSP-coated Cu pads were used. After aging for 1000 hrs at 85°C, the IMCs grew slightly, but were still smaller than the Cu_6Sn_5. The authors stated that these $(Cu,Ni)_6Sn_5$ IMCs came from the bulk solder since the 5 μm-thick Ni barrier prevented the diffusion from the Cu pad. A very thin Cu_3Sn layer, less than 0.1 μm, had also formed after aging. The authors did not state if the Ni layer was still present after reflow.

Chan and his colleagues conducted several studies on the interfacial reactions between Sn-Ag-Cu solders and Au/Ni metallization [6, 17, 25]. In all the studies, 760 μm Sn-3.5Ag-0.5Cu solder balls were utilized. Electroless nickel, Au/NiP (or ENIG), was used in two studies [6, 17] and electrolytic nickel, Au/Ni, in another [25]. The thickness of the Ni layer was between 3.5 and 5 μm. The IMC that formed at the solder ball/Ni interface was found to be $(Cu,Ni)_6Sn_5$, regardless of the reflow temperature, reflow time, and surface finish composition (Au/Ni or Au/NiP). For the electroless Ni finish, a very thin layer of Ni-P intermetallic was found between the $(Cu,Ni)_6Sn_5$ and NiP layers. The IMC thickness increased as reflow/aging time was increased. Spalling of the $(Cu,Ni)_6Sn_5$ was observed after reflowing at 260°C for 1 min for 40 times. Voids were also observed on the P-rich Ni layer. The entire NiP layer was fully consumed after reflow at 250°C for 180 min. The Cu_3Sn layer was found after 30 cycles of reflow or extended reflow for 180 min. In the case of the electrolytic Ni finish, the same

$(Cu,Ni)_6Sn_5$ IMC was found after reflow; this IMC transformed to $(Ni,Cu)_3Sn_4$ after aging for 12 days at 190°C. The authors deduced that this IMC started to form when the Cu content of the solder ball was reduced. The growth rate of the $(Cu,Ni)_6Sn_5$ was faster than that of the $(Ni,Cu)_3Sn_4$. After aging for 16 days at 190°C, the Ni layer was fully consumed, and Cu_6Sn_5 IMC was found instead. Between the Cu_6Sn_5 and the Cu layer, Cu_3Sn was found.

Yu and his colleagues [26] found facet-like, column-shaped, and stick-shaped IMCs at the solder/substrate interface when pure Ni coupons were dipped in Sn-3.5Ag-0.7Cu solder for 90 sec. The composition, $(Cu,Ni)_6Sn_5$, was the same regardless of the IMC morphology. The Ni content was highest for facet-like IMCs and lowest for stick-shaped IMCs. Several Ag_3Sn particles were also reported to form on top of the $(Cu,Ni)_6Sn_5$ IMCs. Increasing the dipping time had little effect on the size of these particles.

Vuorinen *et al.* [27] studied the phase formation between Sn-3.8Ag-0.7Cu solders and 2 μm thick-NiP finishes by reflowing five times at 240°C. After reflow, the $(Cu,Ni)_6Sn_5$ IMC was found at the interface. The $(Ni,Cu)_3Sn_4$ compound was found between the $(Cu,Ni)_6Sn_5$ and Ni-P substrate after five reflows. Using transmission electron microscopy (TEM), the authors stated that the first phase to form was the metastable nanocrystalline NiSnP layer, which served as the site for the formation of $(Cu,Ni)_6Sn_5$. The elemental composition of this phase was unknown. The absence of the metastable NiSnP phase after reflow led the authors to deduce that during cooling or subsequent reflows, the SnNiP transformed into Ni_3P. The Ni_3P composition was

verified from the electron diffraction pattern. This Ni_3P later transformed into Ni_5P_2 after further annealing at 170°C, which implies that more Ni had diffused into the solder.

Ho *et al.* [28] determined the reaction between Sn-3.9Ag-×Cu solders, with × varying between 0.2 and 3.0 wt%, and pure Ni disks at 250°C for 10 min and 25 hours. At the reaction time of 10 min, the $(Ni_{1-x}Cu_x)_3Sn_4$ IMCs were continuous layers with a particle-like grain structure, for low Cu content. At a Cu concentration of 0.4, the $(Ni_{1-x}Cu_x)_3Sn_4$ became round and particle-like and a second IMC, $(Cu_{1-y}Ni_y)_6Sn_5$, appeared and was cylindrical with pointed tips and hexagonal cross-sections. At 0.6 wt% Cu, the $(Ni_{1-x}Cu_x)_3Sn_4$ IMC disappeared and only a continuous layer of $(Cu_{1-y}Ni_y)_6Sn_5$ was left on the interface. For the solders and Ni disks that were reacted for 25 hrs, the composition of the reaction products did not differ much from those reacted for 10 min, except for the increased thickness.

The reflow of Sn-3.8Ag-0.7Cu solders with 2 μm-thick NiP at 240°C for 50 sec was also conducted [29]. Ag_3Sn crystals and very small Cu_6Sn_5 crystals were observed in the solder matrix. The authors postulated the existence of $(Cu,Ni)_6Sn_5$; however, Ni was embedded in the solder matrix, hence, only Cu_6Sn_5 was observed.

There is no uniformity on the composition of the intermetallic compound that was found at the solder/Ni interface after reflow. Some researchers found $(Cu,Ni)_6Sn_5$, others found $(Ni,Cu)_3Sn_4$, while some authors detected Cu_6Sn_5. The $(Cu,Ni)_6Sn_5$ intermetallic compound is the most prevalent composition identified by the researchers. These IMCs were found to be slightly smaller than the Cu_6Sn_5 IMCs found in the bulk solder.

2.1.2 Dissolution of Base Metal

Copper is widely used in electronic packaging as a substrate metallization due to its good electrical conductivity. Electrical conductivity is an intrinsic property of a material and is proportional to electrical conductance (which is inversely proportional to cross-sectional area). With the increasing demand for smaller devices, any small change in the electrical conductivity may play a critical role in the reliability of the device.

As a result of the reaction between the molten solder and the substrate, some of the substrate is dissolved, forming an intermetallic layer. The dissolution of the substrate at the solder/substrate interface promotes the formation and the growth of the intermetallic compounds [19]. Cu readily reacts with Sn-Ag-Cu to form intermetallic compounds, which according to some researchers, can affect the reliability of the solder joints due to the brittle nature of the intermetallic layer. As a result, nickel is used as a protective layer to prevent the rapid interfacial reaction between the solder and the Cu conductor [30]. Even though Ni reacts with the solder, the rate of reaction is slower than that between the Cu and the solder. As a result, a thin Ni_3Sn_4 layer is formed when Ni reacts with Sn-rich solders, which according to Kang [3] is insufficient to act as a reaction barrier during the soldering reaction. Kang and his colleagues found that the lower the Cu content in the Sn-Ag-Cu solder, the slower the dissolution rate of NiP. However, no explanation for this finding was provided. They also noted that the rate of substrate dissolution was lower than the intermetallic layer growth rate. In addition, the rate of dissolution for both electroplated Ni and electroless NiP in Sn-Ag-Cu was about the same, but the rate of intermetallic growth was three times smaller in the former.

Sharif and his colleagues [25] also found that the thickness of the consumed Ni layer decreased with decreasing Cu content when the samples were aged for several days at 190°C, after reflow at 250°C for 1 min. The same $(Cu_{1-x}Ni_x)_6Sn_5$ compound was found in both experiments. However, multiple reflows alone led to a fast NiP dissolution rate in the low-Cu solders [6].

The common finding on this issue is that the amount of dissolved base metal increased with increasing reflow time and reflow cycles.

2.1.3 Spalling

Spalling is described as the phenomenon where scallop-like Cu_6Sn_5 intermetallic compounds become spheroidal in shape, leave the substrate, and migrate into the solder [9]. As the metallization of the substrate, e.g., Cu, is consumed, the reaction between the solder and Cu stops, but the scallop-like intermetallic compounds which already formed at the solder ball/Cu interface continue to grow, and are later transformed into spheroids. Kang *et al.* [3] showed that the absence of Cu in the Sn-Ag solder led to the spalling of the intermetallic compounds from the solder/substrate interface after reflow at 250°C for 20 min. Sn reacts with the NiP layer, forming the Ni-Sn intermetallic layer. However, since the rate of reaction of Ni with Sn is slower than that of Cu with Sn, and the amount of the substrate is limited but the intermetallic layer still undergoes ripening, the Ni-Sn layer spalls from the solder/substrate interface.

Spalling was also observed in Cu-containing Sn-rich solders by Tu *et al.* [9], Islam and Chan [17], and Chen *et al.* [31]. It appears that spalling is affected by both intermetallic compound formation and base metal dissolution. These authors have

proposed different theories for the occurrence of this phenomenon, with no resolution to date.

2.1.4 Voiding

A void is an agglomeration of vacancies or missing atoms. It has been found that Pb-free solders are more prone to voiding than their Pb-containing counterparts. Chen *et al.* [31] studied the interfacial reactions between Sn-3.5 Ag solder and electrolytic Ni and electroless Ni (ENIG or NiP), by reflowing the solder wires on the Ni-based Under-Bump-Metallizations (UBMs) at 251°C for 5 sec to 5 hrs. They found that when electrolytic Ni UBM was used, no voids were observed, whereas voids were found when NiP UBM samples were employed. The authors stated that the introduction of P in the UBM led to the formation of voids in the interface between the NiP layer and the Ni_3Sn_4 intermetallic compound. These voids were also found in the intermetallic layers between the solder/substrate interface, after the sample was thermally-aged for long periods at 150°C, and shorter periods at higher aging temperatures [32]. The authors also found an increase in voiding when aging time was increased. They postulated that the unbalanced interdiffusion between Sn in the solder and Ni in the UBM could be the reason for this phenomenon.

The occurrence of voids is attributed to three major factors: (a) flux entrapment, (b) dissolved gas in raw materials, and (c) solder shrinkage during solidification [33]. In the first case, O'Hara's "Flux-exclusion-rate Model" is utilized, which states that a solvent with a lower boiling point would have a greater potential for flux entrapment and voiding. This model will dominate if the process temperature is lower than the boiling

point of the solvent. The trapped flux in the molten solder outgases, hence, causing voids.

Gases dissolve in liquids. According to Sievert's Law, the amount of the dissolved gas in the molten solder, [H], is proportional to the square root of the partial pressure, P_{H2}, of a diatomic gas, that is, $[H] = k (P_{H2})^{1/2}$ [34]. At T = 760°C, the solubility of oxygen in liquid tin is 0.05 at % [35], while the solubility of hydrogen was found to be 0.06 ppm at T = 425°C in 50 wt % Pb-50 wt% Sn solder alloys [36]. During processing of the raw solder material, gases such as oxygen and hydrogen can dissolve in the molten solder, and these dissolved gases, in their monatomic forms, are trapped in the solid solder upon cooling. During the reflow process, the solder is brought to its eutectic temperature and the dissolved gases near the molten solder surface diffuse out, while the gases that were trapped inside the solder remains inside the solder, and coalesce to their molecular form [33]. Hence, these trapped gases cause voiding.

Voids might also form due to solder shrinkage during solidification [33]. If the contact force between the solder and the pad is greater than the solder shrinkage force due to solidification, voids in the solder matrix and between the solder and pad might form.

2.2 Thermodynamics and Kinetics of Solder-Substrate Interfacial Reactions

The formation of intermetallic compounds is the most well-understood among the solder/substrate interfacial reactions. As such, only the formation of intermetallic compounds will be discussed in this Section.

2.2.1 Thermodynamics

To determine if a reaction is likely to occur, the Gibbs free energy change, ΔG [37], is utilized, expressed mathematically as:

$$\Delta G = \Delta H - T\Delta S \qquad \text{Equation 1}$$

where: ΔH is the enthalpy change

ΔS is the entropy change

T is the absolute temperature

If $\Delta G > 0$, the reaction is not thermodynamically favorable. On the other hand, if $\Delta G < 0$, the reaction is spontaneous, that is, the reaction will proceed in the forward direction, as written.

The first intermetallic compound that forms at the solder/substrate interface can be predicted using the following equation [38]:

$$Q \propto \frac{\gamma_{SL}}{(\Delta G_v)^2} \qquad \text{Equation 2}$$

where: Q is the nucleation activation energy

γ_{SL} is the interfacial energy

ΔG_v is the volume free energy change

Intermetallic compounds form as a consequence of good bonding between two metallic materials. One can predict if an intermetallic compound will form between these metals by looking at the phase diagram of the binary alloys. There are two types of intermetallic compounds – stoichiometric (line compounds) and non-stoichiometric

compounds [39]. Line compounds are vertical lines in the phase diagram that have fixed compositions and definite stoichiometries. On the other hand, non-stoichiometric compounds, also called intermediate phases, have a broader composition range compared to the stoichiometric compounds. In the case of Sn-Ag-Cu alloys that come into contact with a Cu substrate, the intermetallic compounds that form are the Cu_6Sn_5, Cu_3Sn, and Ag_3Sn. The phase diagrams of these binary alloy systems are discussed below.

2.2.1.1 The Cu-Sn Binary Alloy System

The phase diagram for the Cu-Sn binary alloy system is shown in Figure 1 [40]. The two prominent intermetallic compounds that are normally found after reflow are Cu_6Sn_5 and Cu_3Sn.

The Cu_6Sn_5 intermetallic compound has two forms – the high-temperature η phase, which is stable above 187°C, and the low-temperature η' phase, which is found at room temperature [41]. The crystal structure of η-Cu_6Sn_5 was reported to be of the NiAs ($B8_1$)-type with lattice constants a = 4.2 Å and c = 5.09 Å [42]. Bernal found that this Cu_6Sn_5 compound can be regarded as a superlattice* with a = 20.85 Å and c = 25.1 Å, with the unit cell containing 230-250 Sn atoms and 280-300 Cu atoms, which corresponds to the composition Cu_6Sn_5 [43-45].

* A superlattice can be regarded as an ordered solid solution where solute atoms take up an orderly, periodic arrangement while still remaining on the lattice points of the solvent [48]

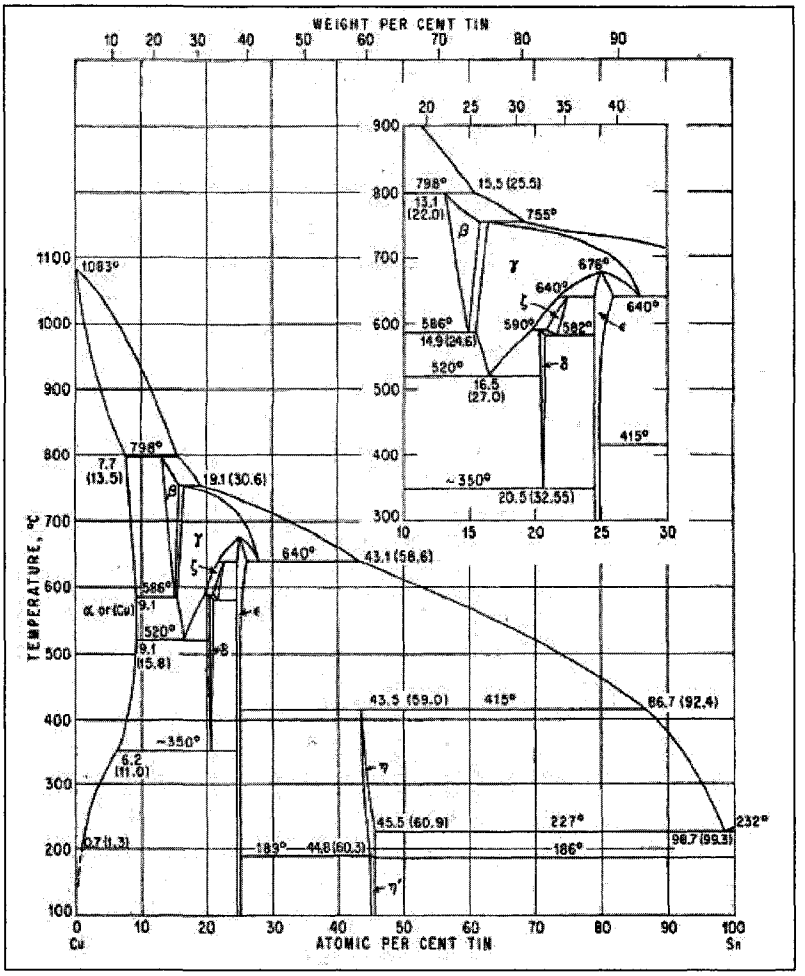

Figure 1. Cu-Sn binary phase diagram [40].

In the hexagonal NiAs structure, the larger atomic species or main group elements are located in the hexagonal close-packed sites, while the smaller atomic species or transition metals occupy the octahedral interstitial sites [46]. The schematic of the η-Cu_6Sn_5 based on the NiAs ($B8_1$)-type structure is shown in Figure 2. The Cu atoms occupy the octahedral interstitial sites while the Sn atoms are at the hexagonal close-packed sites.

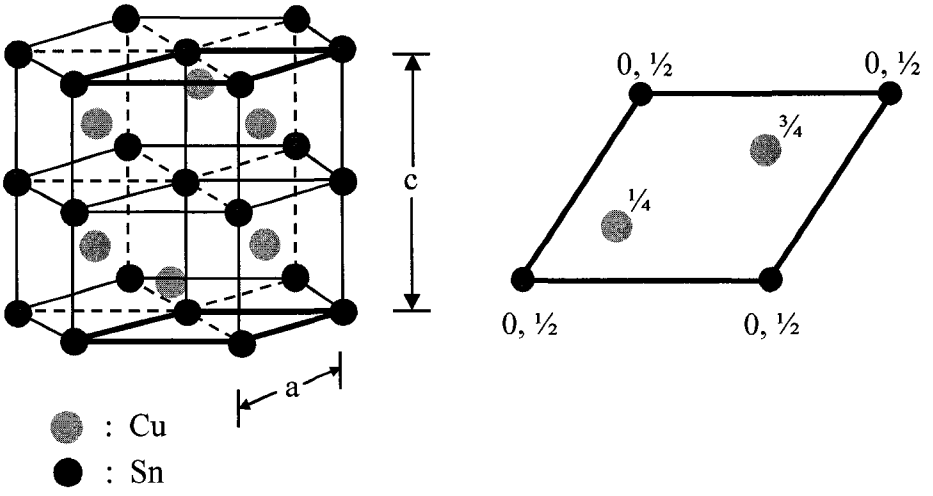

Figure 2. Schematic of η-Cu_6Sn_5 crystal structure based on NiAs ($B8_1$)-type structure.

Gangulee found that the η-Cu_6Sn_5 phase was of the hexagonal NiAs-type structure with $a = 4.192 \pm 0.002$ Å and $c = 5.037 \pm 0.002$ Å; however, additional reflections were found in the diffraction pattern of the η'-Cu_6Sn_5 phase, with $a = 20.870 \pm 0.002$ Å and $c = 25.081 \pm 0.002$ Å [42]. In this study, he and his colleagues were able to establish that the η-η' transition in the Cu_6Sn_5 phase was due to a simple superlattice η ⇌ long-period superlattice* η' transformation, which is accompanied by a 0.4% contraction in the principal lattice directions. There are some researchers, however, who report η'-Cu_6Sn_5 to have a monoclinic lattice [41]. The difference in finding may be attributed to the sample type used. Ideally, single crystal Cu_6Sn_5 intermetallic compounds are preferred for X-ray diffraction analysis. However, since the preparation of single crystal intermetallic phases is difficult, powder samples are utilized instead [47].

* A long-period superlattice can be described as the periodic arrangement of two identical unit cells that become different in phase when referred to some common origin [42]

With superstructures like the Cu_6Sn_5 phase, the superstructure or satellite reflections are difficult to observe in powder diffraction measurements since the intensities of these reflections are only about a tenth of the main reflections [48]. Intermetallic compounds also have a high absorption coefficient; hence, these weak satellite reflections are often ignored and considered as an impurity [47]. This poses a problem in the correct indexing of the diffraction peaks.

The ε-Cu_3Sn phase is a "near-stoichiometric" intermetallic compound. Its stoichiometric composition of 75 at % (61.63 wt %) Cu and 25 at % (38.37 wt %) Sn remains the same from room temperature to about 670°C. The ε-Cu_3Sn phase has an orthorhombic symmetry having the orthorhombic Cu_3Ti-type crystal structure [49], with 64 atoms per unit cell and lattice constants of a = 4.33 Å, b = 5.55 Å, and c = 38.1 Å [43-44]. A schematic diagram of the ε-Cu_3Sn phase is shown in Figure 3.

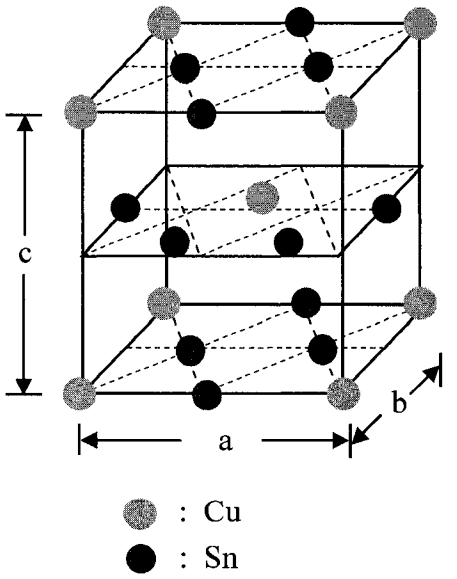

Figure 3. Schematic of Cu_3Sn crystal structure based on Cu_3Ti-type structure (adapted after the schematic in [49]).

2.2.1.2 The Ag-Sn Binary Alloy System

The most prominent intermetallic compound in the Ag-Sn phase diagram is Ag_3Sn, as shown in Figure 4 [50]. This near-stoichiometric intermetallic compound is a precipitation by-product of Ag and Sn. For Sn-rich Pb-free solders that contain Ag, at temperatures below 221°C, the Ag_3Sn phase will have a fixed composition of 75 at % (73.2 wt %) Ag and 25 at % (26.8 wt %) Sn.

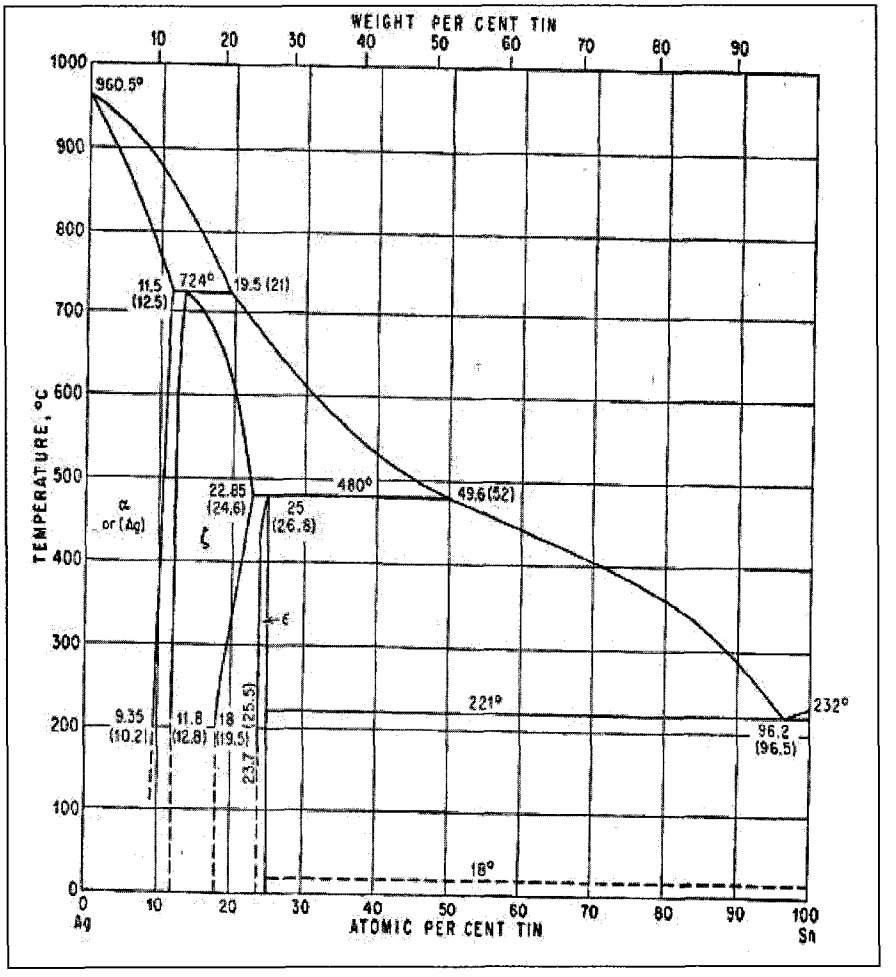

Figure 4. Ag-Sn binary phase diagram [50].

2.2.1.3 The Cu-Ni Binary Alloy System

Cu-Ni is an isomorphous alloy system, that is, Cu and Ni are completely soluble in each other in both the solid and liquid states. No intermetallic compounds form between Cu and Ni. The Cu-Ni phase diagram is shown in Figure 5 [51]. The amount of each element present depends on the temperature and chemical composition of the alloy.

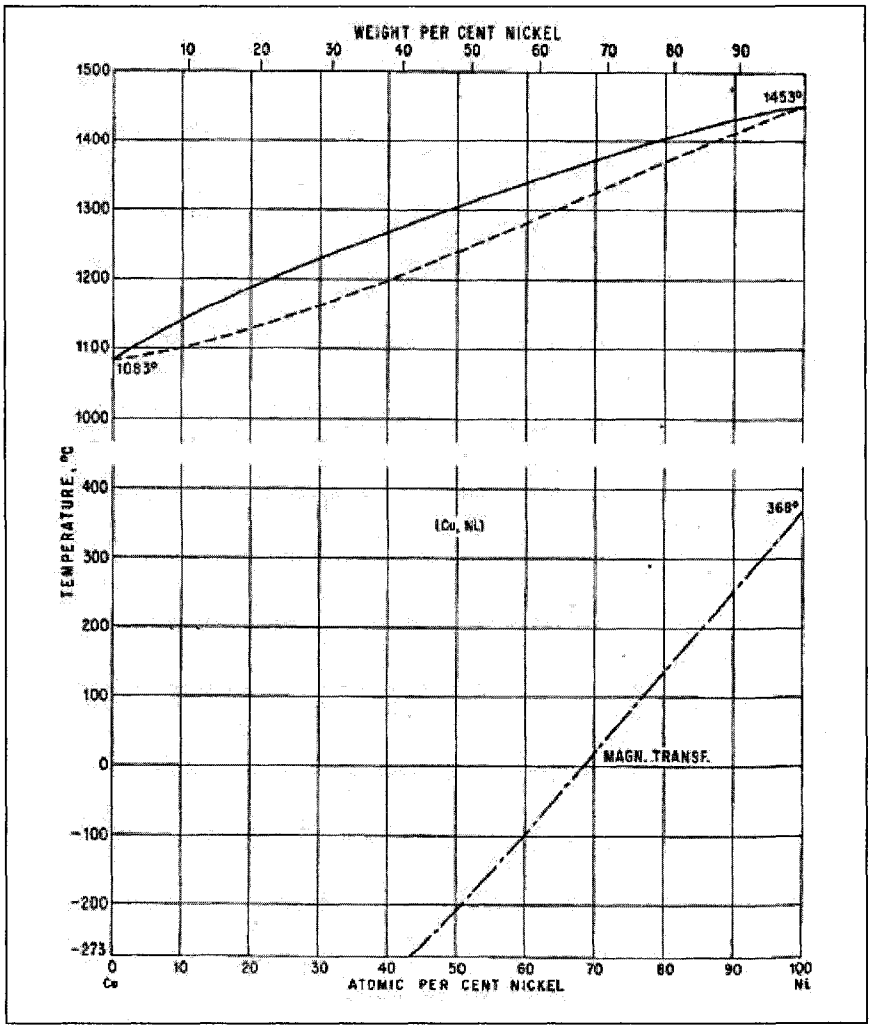

Figure 5. Cu-Ni binary phase diagram [51].

2.2.1.4 The Ni-Sn Binary Alloy System

The Ni-Sn phase diagram is shown in Figure 6 [52]. This system has three intermetallic compounds, namely, Ni_3Sn, Ni_3Sn_2, and Ni_3Sn_4. Of these IMCs, only Ni_3Sn_4 is normally found after reflow. The composition of Ni_3Sn_4 is practically constant from room temperature to 600°C [52].

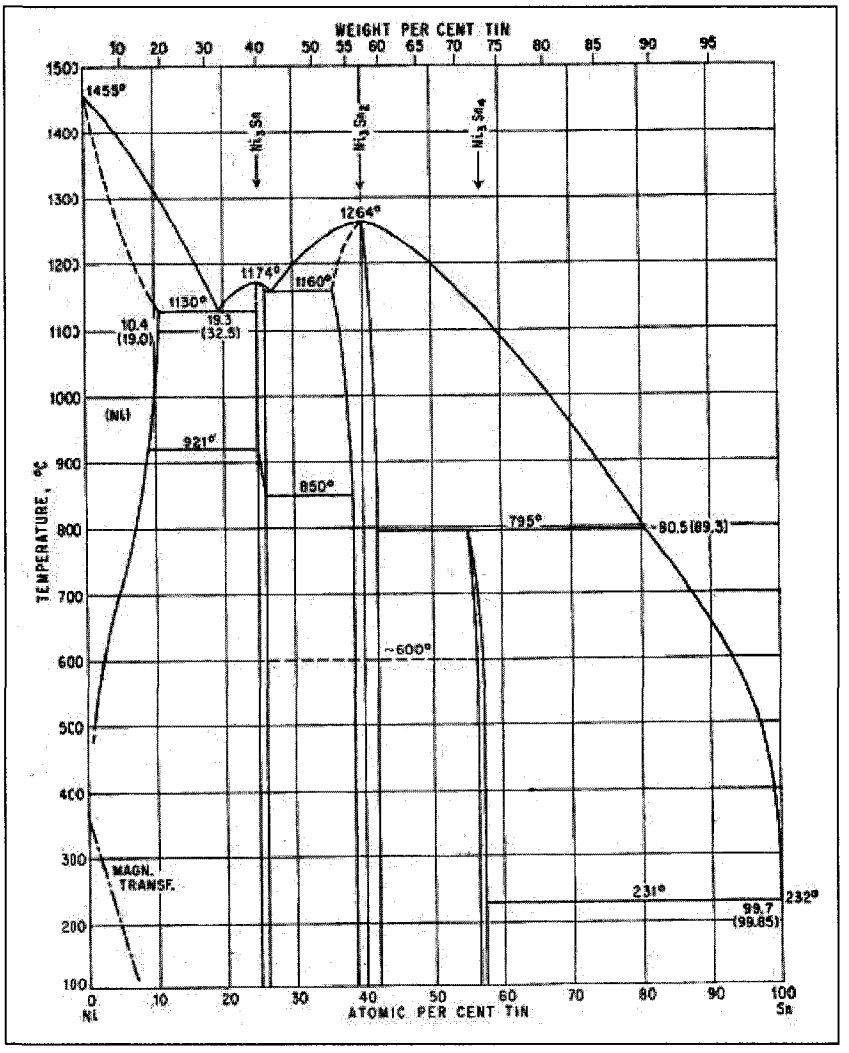

Figure 6. Ni-Sn binary phase diagram [52].

2.2.1.5 The Ag-Cu Binary Alloy System

The Ag-Cu system exhibits eutectic behavior, with no intermetallic compound formation, as shown in Figure 7 [53].

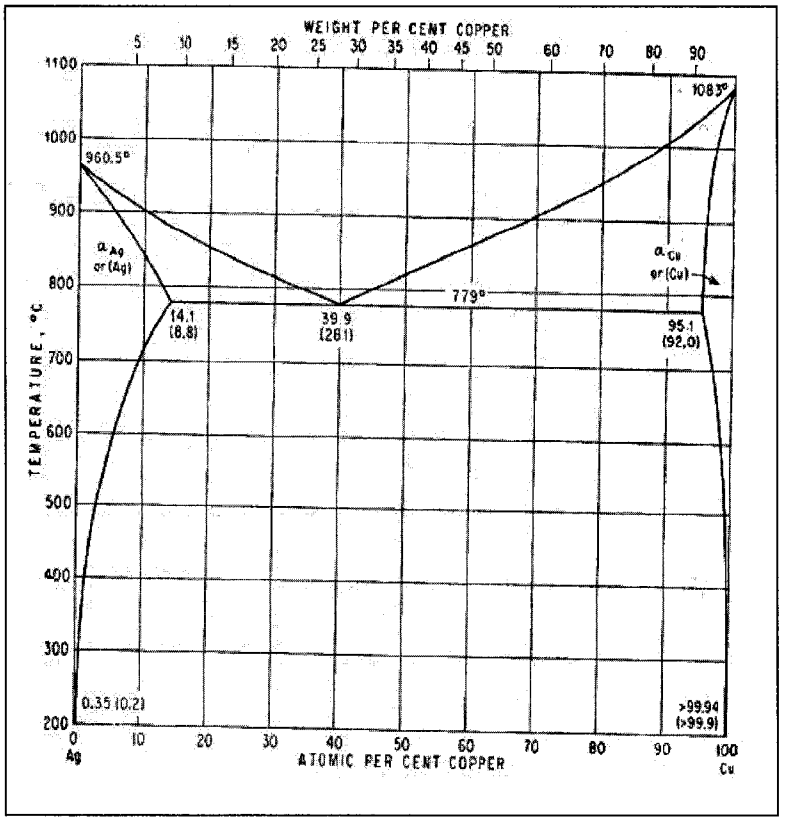

Figure 7. Ag-Cu binary phase diagram [53].

2.2.1.5 The Ag-Ni Binary Alloy System

The Ag-Ni system is distinctly different from the other binary systems in that it exhibits immiscibility in both the solid and liquid forms. The solid solubility of Ni in Ag is 0.102 % at 922°C, and the solid solubility of Ag in Ni, at temperatures below 960°C is extremely small, and no quantitative data are available [54]. The phase diagram for this binary system is shown in Figure 8 [54].

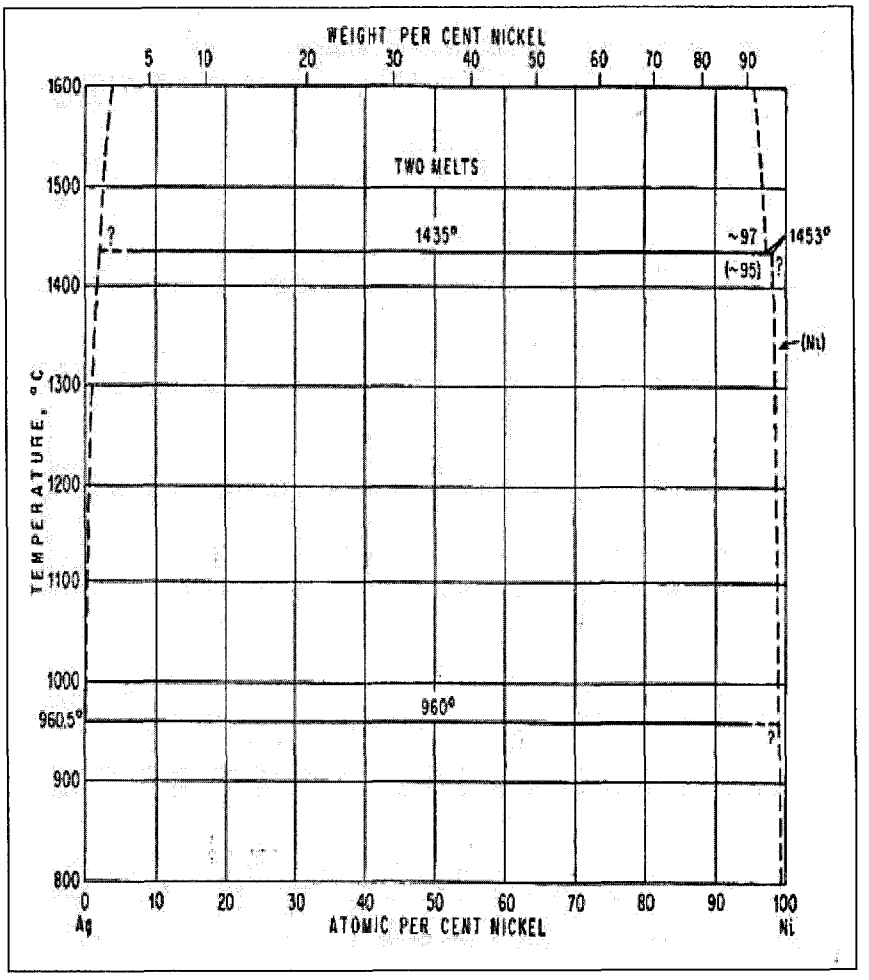

Figure 8. Ag-Ni binary phase diagram [54].

2.2.2 Kinetics

Most of the data available in the literature are related to the growth kinetics of the intermetallic compounds, as a function of growth temperature. One of the assumptions frequently made is the parabolic relationship between the IMC thickness and growth time. The relationship can be expressed as [32]:

$$\delta = \delta_o + k\sqrt{t} \qquad \text{Equation 3}$$

where: δ is the thickness of the IMC at time t

δ_o is the thickness of the IMC at time zero

k is the growth rate constant at the temperature considered

and $$k = A\exp\left(\frac{-Q}{RT}\right) \qquad \text{Equation 4}$$

where: A is a constant

T is the absolute temperature

R is the universal gas constant

Q is the activation energy required for the reaction

From Equation 4, it can be deduced that IMC growth during solid-state aging is much slower than during high-temperature reflow because the aging temperatures are lower than reflow temperature. This is why intermetallic compounds that grow during reflow are thicker than those that form during aging. In addition, Equation 3 supports the experimentally observed data that the IMC thickness increases with increasing aging time and reflow time, which is consistent with theory. This would also apply to increasing reflow temperature. Hence, in order to create the thickest IMC, reflow must be performed first, followed by aging for a long time.

Most researchers found that the Cu_6Sn_5 intermetallic compound formed first before the Cu_3Sn intermetallic compound. From Equation 4, the most stable phase, and

hence, the phase that forms first is the one with the lowest activation energy* requirement, Q. Shown in Table 4 [21] are the apparent activation energies of the intermetallic compounds that formed between different solder compositions and Cu. For the Sn-3.5Ag-0.75Cu/Cu samples, Sn-3.5Ag-0.75Cu solder sheets were reflowed on Cu substrates at 40°C above the liquidus temperature of the solder. The samples were then aged at 100°C-200°C up to 60 days. The Sn-3.8Ag-0.7Cu/Cu samples were prepared by reflowing solder paste on Cu sheets twice at 240°C for 60 seconds. The samples were then annealed at 120°C, 150°C, and 170°C for 500, 1000, and 1500 hours. From Table 4, the activation energies of Cu_6Sn_5 are lower than those of Cu_3Sn. This explains why Cu_6Sn_5 forms before Cu_3Sn when Sn-Ag-Cu solders are reacted with Cu.

Table 4. Activation energies of intermetallic compounds [21].

Solder Substrate	Intermetallic Compound	Activation Energy (kJ/mol)
Sn-3.5Ag-0.75Cu/Cu	Cu_6Sn_5	49.1
Sn-3.5Ag-0.75Cu/Cu	Cu_3Sn	80.1
Sn-3.8Ag-0.7Cu/Cu	Cu_6Sn_5	83.9
Sn-3.8Ag-0.7Cu/Cu	Cu_3Sn	102

From experimental results, a scallop-like morphology is normally observed for the Cu_6Sn_5 IMC. There is no explanation as to why it transforms into a "scallop" after reflow. A group of authors, however, attributed this phenomenon to Jackson's parameter, α [55]. This parameter indicates the atoms' degree of attachment to the interface, and determines whether the interface is scallop-like ($\alpha < 2$) or faceted ($\alpha > 2$).

* Activation energy is the energy barrier that must be overcome for a chemical reaction to occur

Tu *et al.* [9] proposed that the average radius of each scallop can be expressed as:

$$\langle R \rangle \cong 0.913(kt)^{1/3} \qquad \text{Equation 5}$$

where: R is the average radius of each scallop

k is the rate coefficient ($\approx 4 \times 10^{-13}$ cm^3/s)

t is the aging time

This equation supports the idea that the average radius of each scallop increases with increasing aging time, consistent with experimental observations.

2.3 Effects of Interfacial Reactions on the Shear Strength of Pb-free Solder Joints

Interfacial reactions between the solder and the substrate can greatly affect the mechanical properties, and hence the reliability, of the solder joint. With Pb-free solders being new on the market, it is very important that the long-term reliability of the solder joints formed with these alloys be thoroughly understood. One common method of determining the strength of these solder joints is by shear test.

Shown in Figure 9 are the shear strengths of Sn-3.0Ag-0.5Cu (hypoeutectic), Sn-3.8Ag-0.7Cu (eutectic), and Sn-4.0Ag-0.5Cu (hypereutectic) solder paste/Cu substrate joints with OSP and ENIG as surface finish, tested at a shear rate of 2000 μm/min [26]. The solder joints were made from single-overlap shear specimens. Each specimen consisted of two fiber-reinforced PCBs. The lower PCB had a 2 mm-diameter Cu pad, and solder paste was then hand-printed on this Cu pad. The upper PCB was then carefully laid on the lower PCB, and these two PCBs were reflowed at 243°C for 40

seconds. After reflow, some specimens were sheared, while some were sheared after further aging at 85°C for 1000 hours.

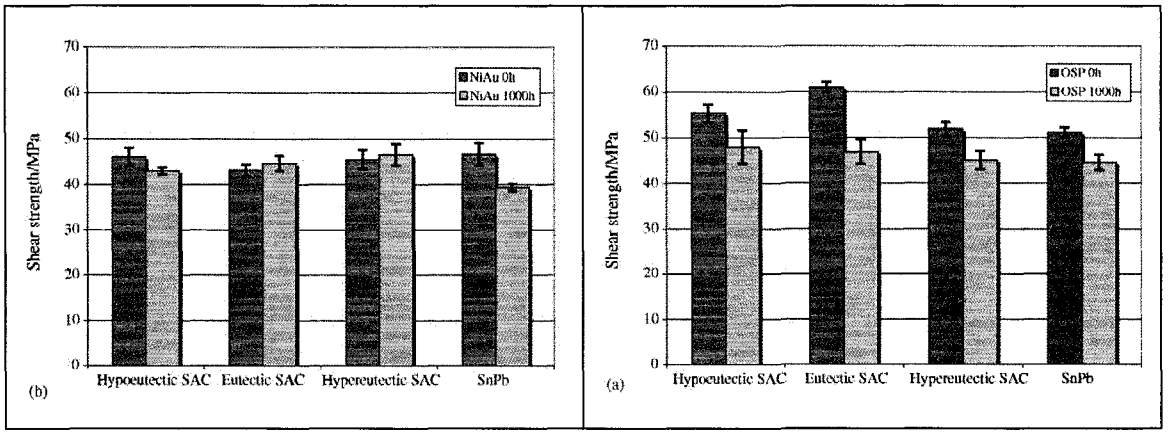

Figure 9. Shear strength of Sn-Ag-Cu/Cu solder joint with (a) OSP and (b) ENIG finishes [26]. (Reprinted from Mat. Sci. and Eng: A, Vol 420, J. Sundelin, S. Nurmi, T.Lepisto and E. Ristolainen, *Mechanical and microstructural properties of SnAgCu solder joints*, 55-62, © 2006, with permission from Elsevier).

The shear strengths of the solder joint specimens with OSP finish were higher than the specimens with ENIG finish after reflow, but were approximately the same after aging. For the OSP finish, the Sn-3.8Ag-0.7Cu/Cu joint had the highest shear strength while the Sn-4.0Ag-0.5Cu/Cu solder joint had the lowest strength, after reflow. A significant decrease in shear strength was found after isothermal aging at 85°C for 1000 hrs. The decrease was as much as 23% for Sn-3.8Ag-0.7Cu/Cu and about 13% for Sn-3.0Ag-0.5Cu/Cu and Sn-4.0Ag-0.5Cu/Cu joints.

For the ENIG finish, the Sn-3.0Ag-0.5Cu/NiP joint had the highest shear strength after reflow, but only slightly higher than that of the other solder joint specimens. It is approximately 3 MPa higher than the Sn-3.8Ag-0.7Cu/NiP joint, and approximately 1

MPa higher than the Sn-4.0Ag-0.5Cu/NiP joint. After aging, there was a decrease of approximately 9% in the shear strength of the Sn-3.0Ag-0.5Cu/NiP solder joint. However, shear strength increases of 5% and 2% were found for the Sn-3.8Ag-0.7Cu/NiP and Sn-4.0Ag-0.5Cu/NiP joints, respectively.

In a study by Sharif *et al.* [27], shear test was done on Sn-3.5Ag-0.5Cu/Ni solder joints. The samples were flexible-substrate BGA packages, with 760 μm-diameter solder balls and 5 μm-thick electrolytic nickel surface finish. The samples were reflowed at 250°C for 60 sec and then aged at 190°C for 2-16 days. The shear test was conducted at a shear rate of 550 μm/sec and a shear height of 100 μm. The results are shown in Figure 10. The shear strength of the solder ball/Ni joint was found to decrease with increasing aging time.

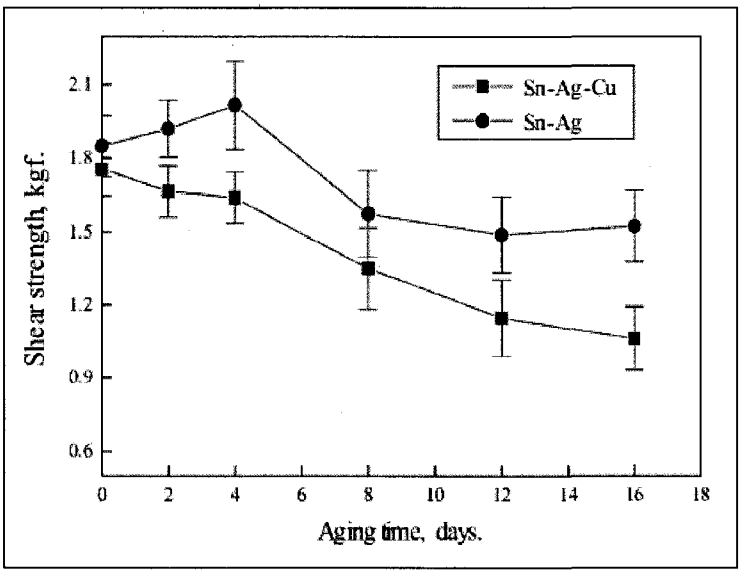

Figure 10. Shear strength of Sn-3.5Ag-0.5Cu/Ni solder joint as a function of aging time [27]. (Reprinted from Mat. Sci. and Eng: B, Vol 113, A. Sharif, M.N. Islam and Y.C. Chan, *Interfacial reactions of BGA Sn-3.5%Ag-0.5%Cu and Sn-3.5%Ag solders during high-temperature aging with Ni/Au metallization*, 184-189, © 2004, with permission from Elsevier).

Hirose *et al.* [2] used disc-type solder joint samples to determine the shear strength of Sn-3.5Ag-0.7Cu/Cu solder joints. The samples were made by reflowing 100 μm-thick solder foils with pure Cu discs at 230°C for 15 sec, then aging the samples at 125°C and 150°C for 500, 1000, and 1500 hrs. The results are shown in Figure 11. The authors stated that there was no decrease in shear strength as aging time was increased. Instead, the shear strength increased after 1500 hrs of aging at 150°C.

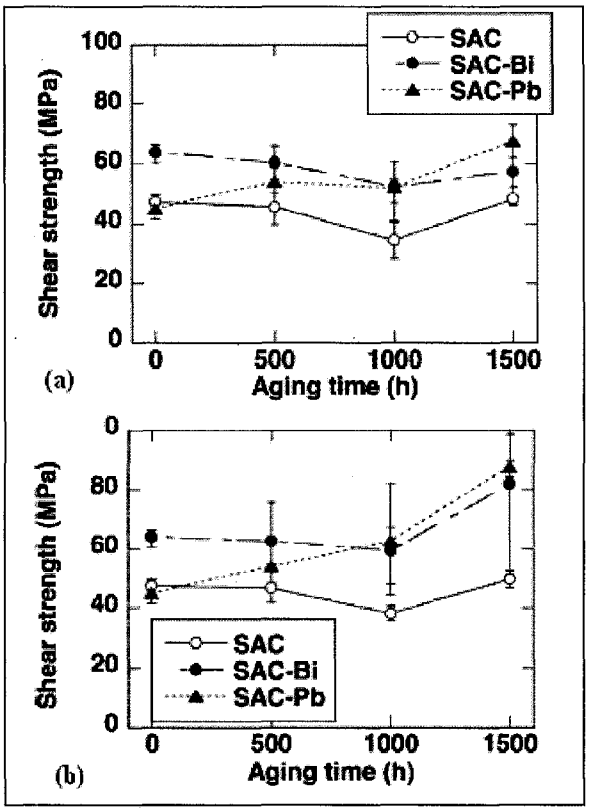

Figure 11. Shear strength of solder joint after aging at (a) 125°C and (b) 150°C as a function of aging time [2]. (Reprinted from Sci. & Tech. of Adv. Mater., Vol 5, A. Hirose, H. Yanagawa, E. Ide and K. Kobayashi, *Joint strength and interfacial microstructure between Sn-Ag-Cu and Sn-Zn-Bi solders and Cu substrate*, 267-276, © 2004, with permission from Elsevier).

D.G. Kim *et al.* [56] found that the shear strength of Sn-3.0Ag-0.5Cu/NiP UBM decreased as the aging time was increased. Sn-3.0Ag-0.5Cu solder paste was reflowed on the ENIG UBM at 250°C for 60 sec, then isothermally aged at 80°C, 100°C, 120°C, and 150°C for 3, 6, 15, 30 50, 60, and 100 days. In all the test conditions used, the shear force was significantly reduced at the initial stage of aging. Overall, the shear strength decreased as aging time was increased, as shown in Figure 12.

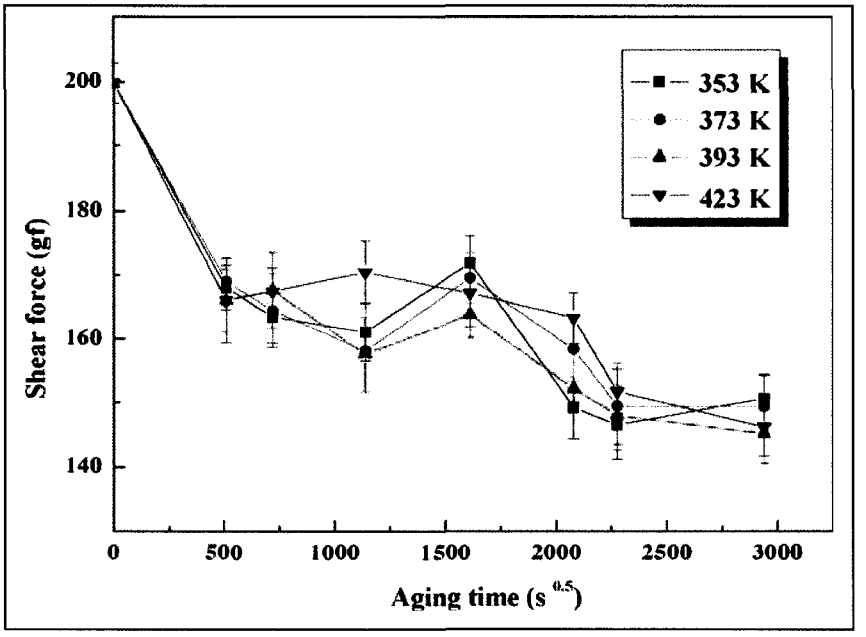

Figure 12. Shear force as a function of aging time for various aging temperatures [56]. (Reprinted from Mater. Sci. & En.: B, Vol 21, D.G. Kim, J.W. Kim and S.B. Jeung, *Effect of aging conditions on interfacial reaction and mechanical joint strength between Sn-3.0Ag-0.5Cu solder and Ni-P UBM*, 204-210, © 2005, with permission from Elsevier).

To determine the cause for the shear force variations, the authors examined the fracture surfaces of the specimens that were shear tested. For the as-reflowed specimens, they found that nearly all of the tested specimens showed ductile failure mode, which

implied that the decrease in shear force at the initial stage of aging was mainly caused by the coarsening of the microstructure within the bulk solder. As the aging time was increased, mixed mode of ductile and brittle failure was observed. They believed that the brittle IMCs were the main cause of the reduction in the shear force after aging.

The shear strength results from these studies are tabulated in Table 5. Although some of the final shear strength values may be about the same, different shear strength behaviors were found. This is because shear rate, solder joint thickness, sample type, IMC thickness, temperature, solder composition, etc., can affect the value of the shear strength. This explains why the shear strength of Pb-free solder joints is still inconclusive.

2.4 Summary of Literature Review

The banning of Pb-containing solders has resulted in the research and development of Pb-free solders. However, more research needs to be done to thoroughly understand these materials. Different intermetallic compounds formed when Sn-rich solders were placed in contact with different base materials. In the case of Sn-Ag-Cu solders that were reflowed with Cu, some authors found that the first intermetallic compound that formed was Cu_6Sn_5, followed by Cu_3Sn and Ag_3Sn. Other researchers, however, found only Cu_6Sn_5, while yet some others detected only Ag_3Sn. The microstructural morphology of the intermetallic compounds was also different in the experiments performed. When the base material was Ni or NiP, some authors found $(Cu,Ni)_6Sn_5$ while others have found $(Ni,Cu)_3Sn_4$. The common observation was that

IMC thickness increased with increasing reaction time, and the amount of base metal dissolved increased as the reflow time was increased.

Different theories have also been proposed for the occurrence of other interfacial reactions such as spalling, base metal dissolution, and voiding. The occurrence of voids is not general to all the solders studied.

The data for the mechanical properties of Pb-free solder joints also differed with each study. This may be attributed to several factors, such as strain rate, sample dimension and geometry, solder composition, intermetallic compound thickness, test temperature, equipment, and test methods that were utilized in the study. No conclusive data are available, at this time, for the mechanical properties of Pb-free solders.

Table 5. Summary of shear strengths of Pb-free solder joints.

Sample	Shear Rate (μm/sec)	Solder Joint Thickness (μm)	Specimen Type	Approximate Shear Strength		Reference
				After Reflow	After Aging	
Sn-3.0Ag-0.5Cu/Cu	33.33	200	Single-overlap	56 MPa	48 MPa	[26]
Sn-3.0Ag-0.5Cu/NiP	33.33	200	Single-overlap	47 MPa	43 MPa	[26]
	N/A	145	Flip chip solder bump	0.2 kgf	0.15 kgf	[55]
Sn-3.5Ag-0.5Cu/Ni	550	N/A	BGA package	1.7 kgf	1.1 kgf	[27]
Sn-3.5Ag-0.7Cu/Cu	830	100	Disc-type	48 MPa	49 MPa	[2]
Sn-3.8Ag-0.7Cu/Cu	33.33	200	Single-overlap	61 MPa	47 MPa	[26]
Sn-3.8Ag-0.7Cu/NiP	33.33	200	Single-overlap	43 MPa	45 MPa	[26]
Sn-4.0Ag-0.5Cu/Cu	33.33	200	Single-overlap	52 MPa	46 MPa	[26]
Sn-4.0Ag-0.5Cu/NiP	33.33	200	Single-overlap	46 MPa	47 MPa	[26]

CHAPTER 3

RESEARCH OBJECTIVES

The objectives of this study were threefold. The first objective was to determine the interfacial reactions that occur between Sn-3.0 wt%Ag-0.5wt%Cu (SAC 305) solder and coatings used on copper pads or copper lead frames, during reflow and subsequent thermal aging. The particular coatings selected for the study were Immersion Silver (ImAg), Electroless Nickel/Immersion Gold (ENIG), and Organic Solderability Preservative (OSP).

The second objective was to determine the shear strength of the solder joints, measured with ball shear test, as a function of aging time, at 150°C. Paired t-test was utilized to interpret the ball shear test results. An α-value of 0.05 was chosen, corresponding to a 95% confidence level. The hypotheses for the study were:

- Null Hypothesis: The mean shear strengths are the same.
- Alternative Hypothesis: The mean shear strengths are different.

The third objective was to determine the relationship, if any, between the nature of the intermetallic compounds formed and the solder joint strength.

CHAPTER 4

EXPERIMENTAL METHODOLOGY

The experimental methodology was divided into four parts. The first part was the acquisition of the printed circuit board and solder balls. The second part consisted of initial board inspection and testing. The third part was reflow of the solder balls onto the PCB and aging of the specimens. The fourth part was characterization of the specimens. Shown in Figure 13 is the overall flowchart of the investigation methodology.

4.1 Experimental Materials

4.1.1 Printed Circuit Board (PCB)

The printed circuit board samples were obtained from San Francisco Circuits [57]. The schematic of the top view of the printed circuit board (PCB) is shown in Figure 14. The PCBs, with the trade name of IS410, consisted of a lead-free laminate that has a glass transition temperature of 180°C. Each PCB was 1.6 mm thick and had a dimension of 25.4 mm × 25.4 mm (1" × 1"). The copper (Cu) substrate was approximately 35 μm thick and the pad diameter was 550 μm. The coatings used were Immersion Silver (ImAg), Electroless Nickel/Immersion Gold (ENIG), with a phosphorus content of 9-13 wt%, and Organic Solderability Preservative (OSP). The thickness of the coatings [57] are shown in Table 6. The ENIG and ImAg coatings are in accordance with the Institute of Interconnecting and Packaging Electronic Circuits (IPC) standards, namely IPC- 4552 and IPC-4553 [58-59]. No industry standard was available yet for the optimum thickness

of the OSP coating at the time of this investigation. The same Au and ImAg coating thickness of 0.05 – 0.127 μm were used for OSP. No solder mask was used on all the specimens.

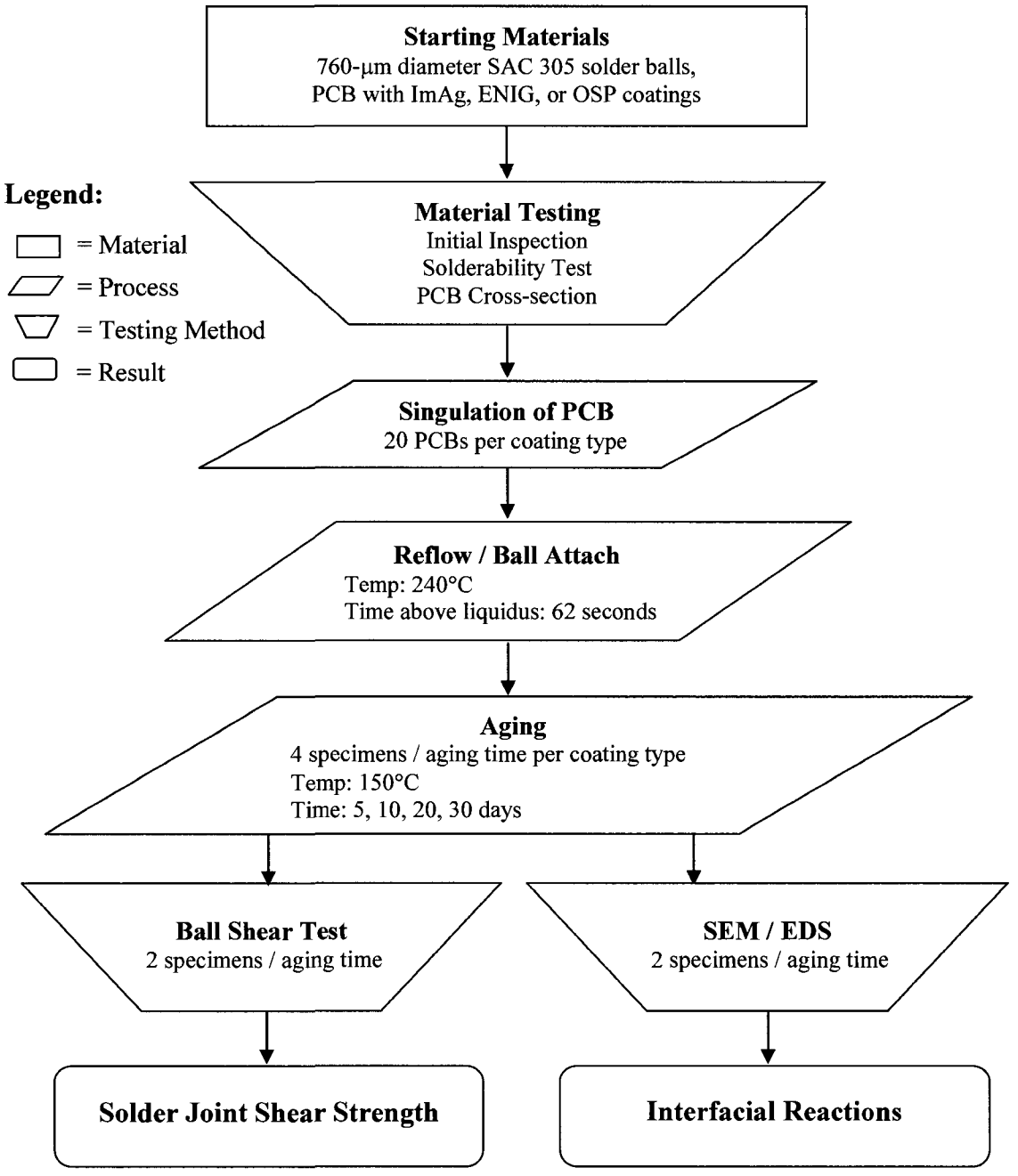

Figure 13. Flowchart of investigation methodology.

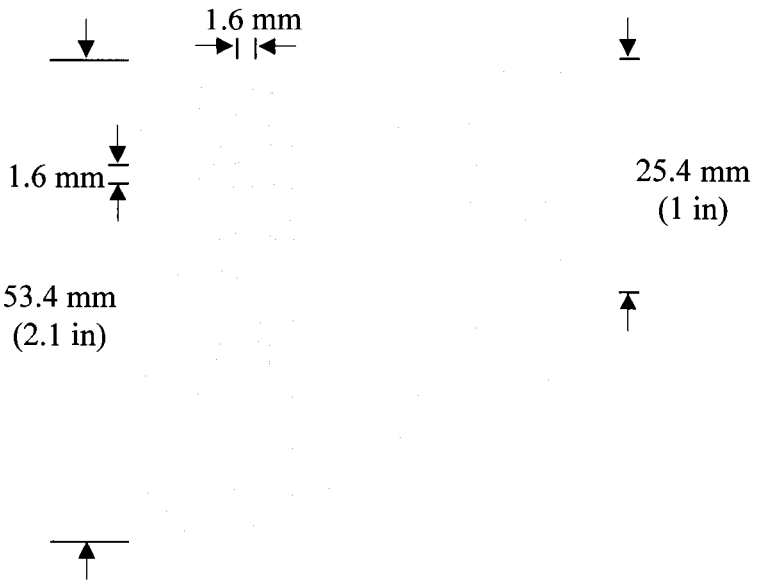

Figure 14. Schematic of the printed circuit board.

Table 6. Coating types and thickness used for the PCB.

Coating Type	Thickness (μm)
Immersion Silver (ImAg)	0.05 – 0.127
Electroless Nickel/Immersion Gold (ENIG)	4 – 5 (NiP), 0.05 – 0.127 (Au)
Organic Solderability Preservative (OSP)	0.05 – 0.127

4.1.2 Solder Balls

96.5 wt% Sn-3.0 wt% Ag-0.5 wt% Cu (SAC 305) Ball Grid Array (BGA) solder balls, with diameter of 760 μm, were purchased from Profound Company [60]. The SAC 305 composition was verified using X-Ray Fluorescence (XRF) by randomly choosing five solder balls from the container. The compositions obtained are shown in Table 7.

Table 7. Solder ball composition as verified by XRF.

Solder Ball #	Composition
1	96.62Sn-2.96Ag-0.42Cu
2	96.53Sn-3.03Ag-0.44Cu
3	96.70Sn-2.85Ag-0.45Cu
4	96.54Sn-2.97Ag-0.49Cu
5	96.50Sn-2.99Ag-0.51Cu

4.2 Initial Board Inspection/Testing

4.2.1 Pad Diameter

Upon receiving the PCBs, the pad diameter for each coating type was checked and verified for consistency. Twenty 25.4 mm × 25.4 mm (1" × 1") PCBs were chosen from each coating finish. Using a Mitutoyo toolmaker's microscope, the pad diameter was measured. Five readings were taken from each 25.4 mm × 25.4 mm sample in random (20 readings per board), totaling 100 random readings per coating finish.

4.2.2 Solderability Test

A specimen was taken from each coating type for solderability testing. Solderability testing for boards was performed in accordance with Joint Electron Device Engineering Council (JEDEC) J-STD-003 [61] to ensure the plating finish was done properly. For the ImAg and OSP-coated PCB specimens, surface mount solderability test was performed. However, for specimens, such as ENIG, with several underlying metallization layers, the "dip and look" approach is preferred since the surface metallization, in this case, gold, is dissolved into the molten solder and the nickel layer

then comes in direct contact with the solder. The specimen passes this test if the solder completely "wets" the copper pad and occupies the entire pad; otherwise it fails.

4.2.3 Cross-section of PCB

Bare printed circuit boards were cross-sectioned and examined to identify defects, if any. A 25.4 mm × 25.4 mm PCB sample, for each coating type, was taken and mounted in a resin/hardener mixture (100 parts by weight Buehler EPO-THIN low viscosity resin and 39 parts by weight EPO-THIN hardener) and cured at room temperature. The samples were then ground and polished according to the sequence shown in Table 8. Microstructural characterization of the boards was done using a scanning electron microscope equipped with an energy dispersive spectrometer.

Table 8. Grinding and polishing steps used for cross-sectioning bare PCB [62].

Surface	Abrasive / Grit Size	Load (lb)	Speed (Direction)	Time (min:sec)
Carbimet	400	5	120 (contra)**	3:00
Carbimet	600	5	120 (contra)	1:30
Carbimet	800	5	120 (contra)	1:30
Carbimet	1200	5	120 (contra)	1:30
Texmet	3 μm	5	240 (contra)	1:30
Microcloth	1 μm	5	120 (contra)	1:30
Microcloth	0.05 μm	5	120 (contra)	1:30

** Contra – head direction is opposite to wheel direction

4.3 Specimen Processing

The PCBs were first divided into four 25.4 mm × 25.4 mm boards before reflow by marking the PCB with a blade and then separating into four parts. An air gun was then used to blow off dirt or any particulates on the PCB surface before reflow. No

additional PCB cleaning step was utilized since the specimens were received in good packing conditions.

4.3.1 Reflow

Reflow was performed in accordance with JEDEC J-STD-020 [63]. This industry standard is a guide, for semiconductor companies, on the proper reflow and processing of moisture-sensitive surface mount devices and materials.

4.3.1.1 Calibration

To determine the actual response of the PCB sample to the reflow profile, calibration runs were first done, using a dummy unit for each coating type. Three thermocouples were utilized to determine the temperature response of center, corner 1, and corner 2, all measured on the topside of the PCB. The PCB was placed on a reflow tray in a Heller 1088 EXL convection oven, which had four top and bottom convection heating zones and one outside cooling zone. The oven had four zones - preheat, reflow, peak, and cool down. The temperature response was monitored using a data logger. The measured reflow profile is shown in Figure 15. The reflow requirements and the actual values are shown in Table 9.

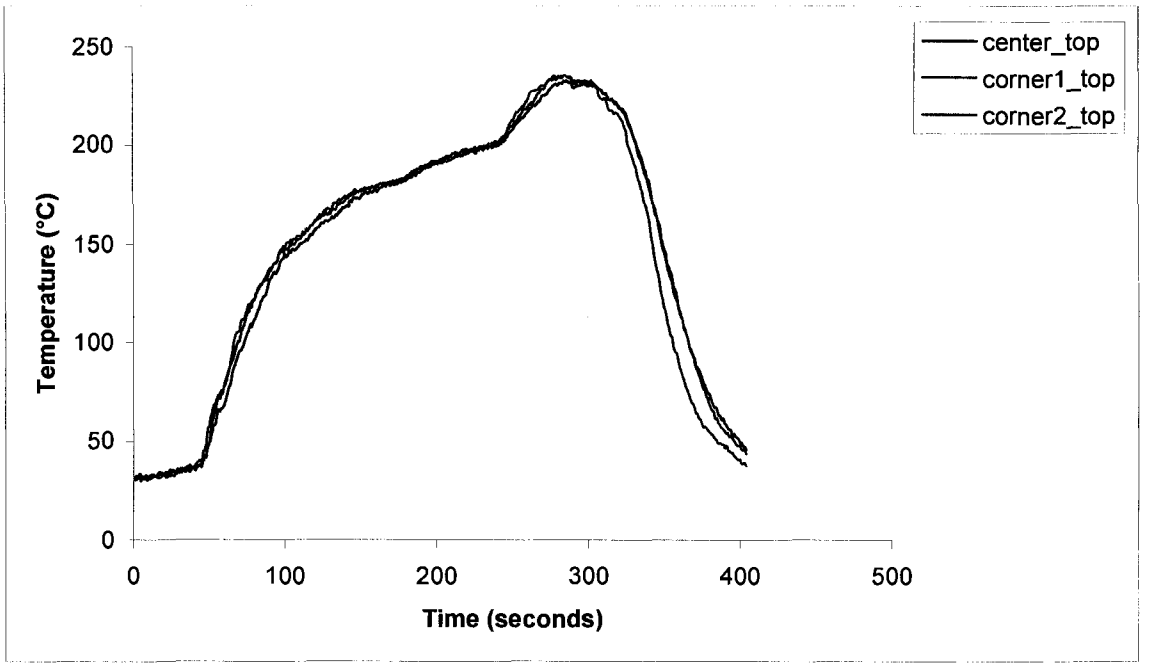

Figure 15. Reflow profile used for ball attach.

Table 9. Reflow profile requirements [63] and the experimental reflow profile.

Profile Feature	J-STD-020 Pb-free Assembly Requirements	Reflow Profile (Experimental)
Average Ramp-up Rate (T_{smax} to T_p)	3°C/sec (maximum)	1.1°C/sec
Preheat -Temperature Min ($T_{s(min)}$) -Temperature Max ($T_{s(max)}$) -Time ($t_{s(min)}$ to $t_{s(max)}$)	 150°C 200°C 60-180 sec	 147.8°C 202°C 136 sec
Time maintained above: -Temperature (T_L) - time (t_L)	 217°C 60-150 sec	 218°C 62 sec
Peak/Classification Temperature (T_p)	Based on package thickness and volume	255°C (measured: 240°C)
Time within 5°C of actual Peak Temperature (t_p)	20-40 sec	26 sec
Ramp-Down Rate	6°C/sec (maximum)	1.1°C/sec
Time 25°C to Peak Temperature	8 min (maximum)	6.8 min

From JEDEC J-STD-020, $T_{s(min)}$ is the preheat temperature at preheat time, t_s. This step is a ramp-up from room temperature to 150°C and is done to prevent thermal shock to the PCB specimen. The preheat time, from room temperature to 200°C, was 136 seconds. $T_{s(max)}$, the maximum temperature at ramp-up, is 200°C. T_L is the liquidus temperature of the solder, 218°C, for time t_L above the liquidus temperature, and the reflow time was 62 seconds. The peak temperature, T_p, is the reflow temperature usually set at 30°C-50°C above the liquidus temperature of the solder. In this case, the peak temperature was set at 255°C, but the actual temperature was 240°C. The dwell time, t_P, within 5°C of the peak temperature, was 26 seconds. Cool down was performed at a rate of 1.1°C/sec. The entire reflow cycle took 6.8 minutes.

4.3.1.2 Ball Attach Process

After the reflow profile was obtained, the Sn-3.0Ag-0.5Cu solder balls were attached onto the printed circuit board following standard industry practices. The ball attach process is depicted in Figure 16. A halide-free water-soluble SAC 305 flux paste (Alpha WS-619-LF) was used. The solder balls were cleaned within 20 minutes after reflow to remove excess flux. The specimens were then placed in a post-clean tray and spray-rinsed for 1 minute under low-pressure DI water. The specimens were then carefully blow-dried to remove excess water, and placed in a moisture-barrier bag until aging, to prevent moisture absorption.

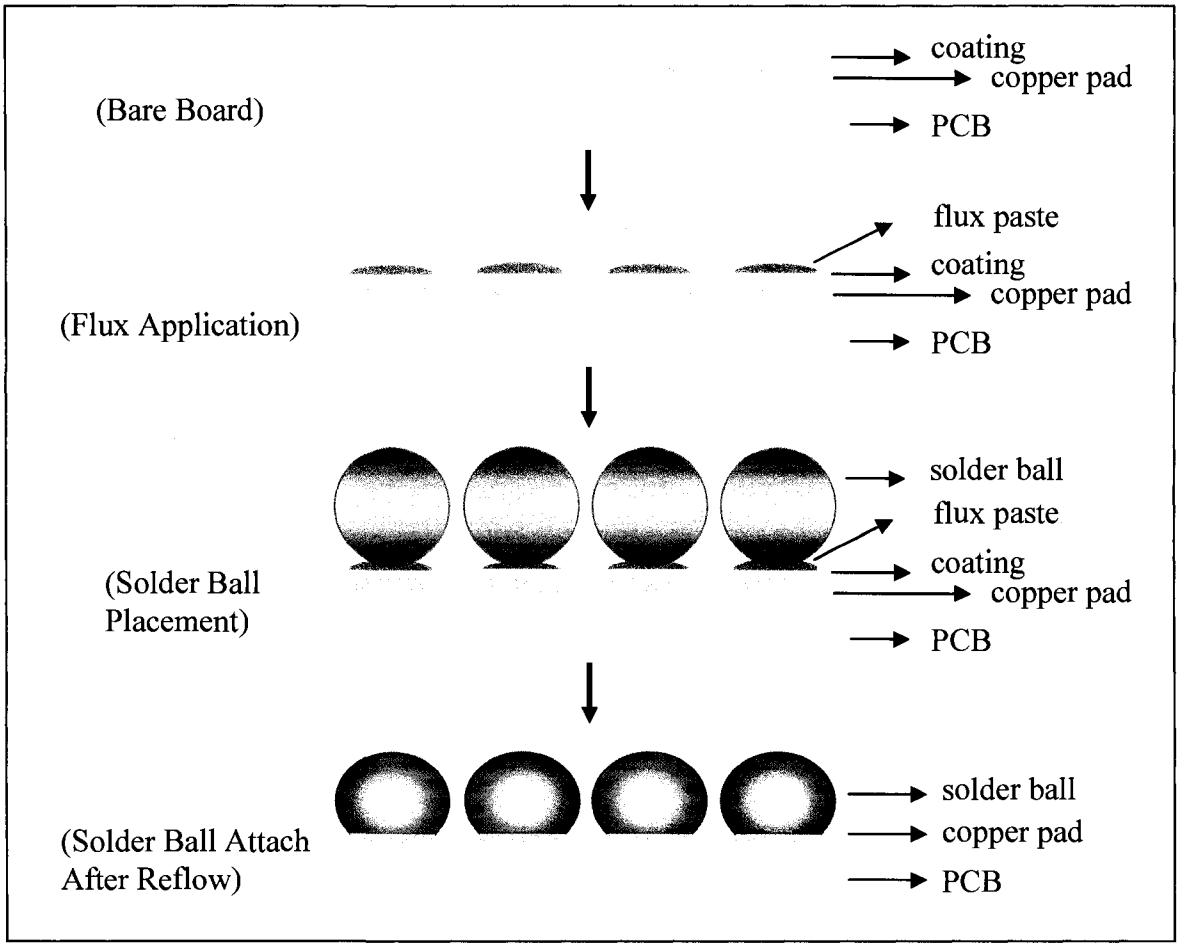

Figure 16. Ball attach process.

4.3.2 Aging

Aging of the specimens was performed after reflow for 5, 10, 20, and 30 days at an aging temperature of 150°C. Shown in Table 10 is the number of specimens utilized for each aging time. Four specimens were used for each aging time (two for ball shear test and two for SEM-EDS) and four control specimens were employed for each coating type. The aged specimens were placed in a Dry Pak bag immediately after aging. The Dry Pak bag was sealed and placed in a freezer with the temperature set at 0°C, to

prevent microstructural changes in the specimens. When the specimens were ready for processing, the Dry Pak bag was removed from the freezer and opened only when it reached room temperature, to prevent the specimens from absorbing moisture.

Table 10. Number of specimens used for each aging time.

Coating Type	Number of Specimens	Aging Time (days)
ImAg	4	0
	4	5
	4	10
	4	20
	4	30
ENIG	4	0
	4	5
	4	10
	4	20
	4	30
OSP	4	0
	4	5
	4	10
	4	20
	4	30

4.3.3 Metallographic Inspection

4.3.3.1 Mounting

The specimens were mounted at room temperature in resin/hardener, a mixture of 100 parts by weight Buehler EPO-THIN low viscosity resin and 39 parts by weight EPO-THIN hardener. Care was exercised to prevent bubbling. Room temperature curing was done for 12 hours.

4.3.3.2 Grinding and Polishing

Wet grinding was done using 400, 600, 800, and 1200 grit-sized sand paper. The sand papers were coated with paraffin wax to prevent SiC particle embedment in the specimen. Polishing, which followed the last grinding step, was done using Buehler Microcloths, impregnated with 1 and 0.05 μm alumina suspension. Grinding and polishing were done using a Buehler Ecomet 3 automatic polisher. The parameters used for this process are shown in Table 11 [64]. After polishing, the specimen was thoroughly washed and rinsed with deionized water.

4.3.3.3 Etching

The polished specimen was immersed in a 2% nital (2 parts HNO_3 and 98 parts isopropanol) etchant for 5 seconds. The specimen was then rinsed with deionized water, followed with an alcohol rinse before drying.

Table 11. Grinding and polishing steps utilized for the specimens [64].

Surface	Abrasive / Grit Size	Load (lb)	Speed (Direction)	Time (min:sec)
Carbimet	320 (wax coated)	4	240 (comp)**	until plane
Carbimet	400 (wax coated)	4	240 (comp)	0:30
Carbimet	600 (wax coated)	4	240 (comp)	0:30
Carbimet	800 (wax coated)	4	240 (comp)	0:30
Carbimet	1200 (wax coated)	4	240 (comp)	0:30
Microcloth	1 μm	5	120 (contra)**	5:00
Microcloth	0.05 μm	4	120 (comp)	4:00

** Comp (complementary) – head direction is the same as wheel direction; contra – head direction is opposite to wheel direction

4.4 Specimen Characterization

Ball shear test was utilized to determine the shear strength of the solder joint, and microstructural analysis of the specimens was performed using Scanning Electron Microscopy-Energy Dispersive Spectroscopy.

4.4.1 Intermetallic Compound Characterization

An FEI Quanta 200 Environmental Scanning Electron Microscope with Energy Dispersive X-Ray Analysis was used for microstructural and composition analysis of the intermetallic compounds that formed at the Cu substrate-solder ball interface, and determine the microstructures that formed at the bulk solder ball. The accelerating voltage was 20 kV. A carbon evaporator was used to coat the specimens to prevent charging. Knowing the probe size that corresponds to each spot size was critical, since it should be smaller than the area of interest. Shown in Figure 17 is the corresponding probe size diameter for each spot size (for each voltage) for the SEM-EDS system used in this research. The same accelerating voltage of 20 kV and a spot size of 5 were utilized for all specimens.

Two specimens per aging time for each coating type were used for this test. The 10 highest thicknesses, t_{max}, and the 10 lowest thicknesses, t_{min}, of the intermetallic compounds that formed at the metal substrate-solder ball interface were measured for each specimen after reflow and subsequent aging, as shown in Figure 18. The averages of t_{max} and t_{min} were then obtained and plotted separately against aging time.

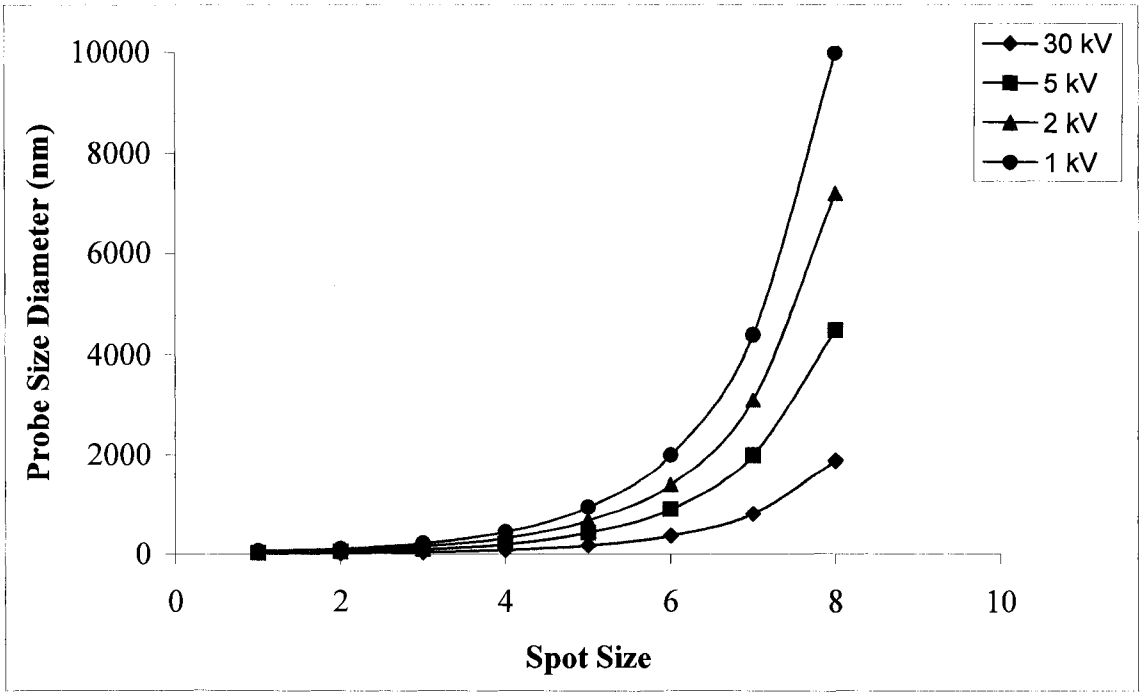

Figure 17. Probe size diameters for each spot size (as a function of voltage) [65].

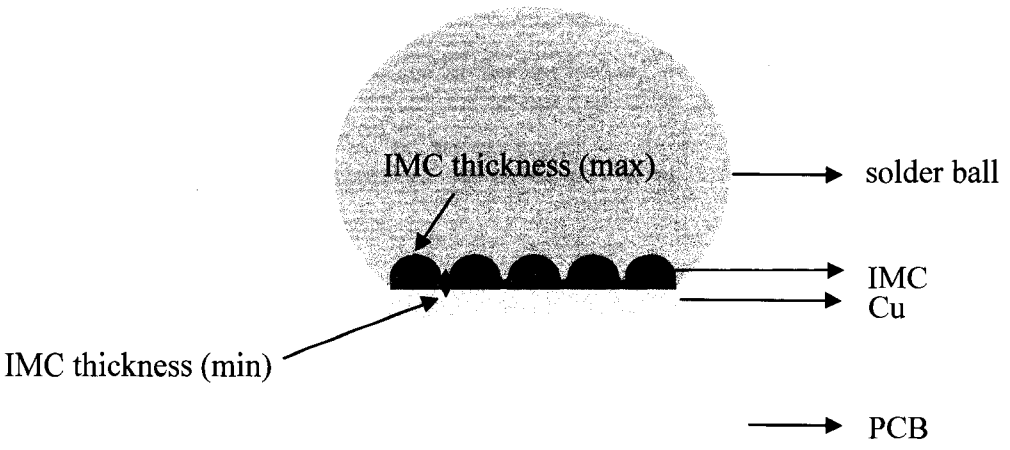

Figure 18. Schematic of IMC thickness measurement.

4.4.2 Shear Strength

The solder joint strength after reflow and subsequent aging was determined by using the ball shear test setup shown in Figure 19 [66], using a Royce System 552 shear tester. The specimen was placed on the test fixture and held rigidly so that the solder ball can be sheared by the shear probe, which presses directly against the BGA solder ball during shearing. The other end of the probe was attached to the ball shear tester to measure the shear force. The shear height used was 20% of the solder ball height. The ball was sheared at a constant rate of 200 μm/sec. Loading was continued until the maximum load was reached, and until the load fell to at least ¾ of the maximum load. After this, loading was stopped. For each sheared solder ball, the maximum load and failure mode were recorded. According to the JEDEC standard for ball shear, JESD22-B117, the acceptable failure modes for ball shear are ductile, pad lift, ball lift, and interfacial break [66].

Two specimens per aging time for each coating type were used for ball shear test. Ten solder balls were sheared per specimen, and the maximum shear force from each specimen for the same aging time and coating type were combined. To determine the shear strength, the maximum shear force for each sheared solder ball was divided by the cross-sectional area of the pad, which was taken to be representative of the cross-sectional area of the solder ball. The ball shear strength values were then plotted against aging time.

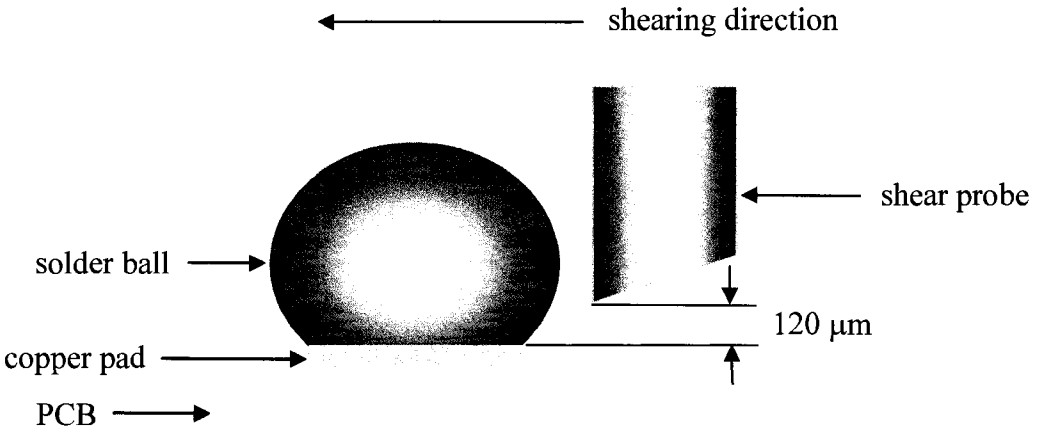

Figure 19. Schematic of the BGA ball shear test setup.

4.4.3 Data Analysis

To determine if the relationship between the intermetallic compound growth and time is parabolic, the averages of the IMC thicknesses, t_{max} and t_{min}, were plotted individually against the square root of aging time. For the ball shear test results, the averages of the ball shear strengths for each coating type were plotted against aging time and the trends were manually obtained by using the software features. These trends were then compared with the calculations obtained from the student t-test to determine if a statistical difference existed between the ball shear test results obtained for different aging times.

CHAPTER 5

RESULTS

The interfacial reactions that formed for each coating type after reflow and subsequent thermal aging at 150°C for 5, 10, 20, and 30 days are presented in this chapter. Results obtained from the initial testing of the printed circuit boards are presented in Sections 5.1 through 5.3. The intermetallic compounds that formed between the solder and the different Cu-coated PCB coatings, and the ball shear test results for each aging time are discussed in Sections 5.4 through 5.6. A comparison of the results for each coating type is presented in Section 5.7.

5.1 Pad Diameter

The desired Cu pad diameter of the printed circuit board was 550 μm ± 25 μm. Shown in Table 12 are the mean, standard deviation, maximum, and minimum values of the pad diameters measured for each coating type. The mean pad diameters of the specimens for the 3 coating types were all within the tolerances of the desired value. The raw data and histograms for the pad diameters are included in Appendix A.

Table 12. Average and standard deviation of Cu pad diameters for each coating type.

Coating Type	Mean (μm)	Stdev (μm)	Maximum (μm)	Minimum (μm)
ImAg	545	11	563	527
ENIG	547	9	561	533
OSP	539	9	554	523

5.2 Solderability Test

A specimen was taken from each coating type. Surface mount solderability test was utilized for the specimens with OSP and ImAg coatings; dip and look solderability test was employed for the ENIG-coated specimens. Two requirements must be satisfied in order to pass these tests – wettability and flowability [67]. First, the solder must be able to wet the base metal, in this case, Cu or Ni. The solder must adhere to the base metal and must continue to do so until the solder has solidified. Second, the molten solder must be able to spontaneously fill the entire pad diameter. All three specimens passed the solderability tests, which were done according to J-STD-003. As can be seen from Figure 20, the solder wetted the base metals and filled the entire pads.

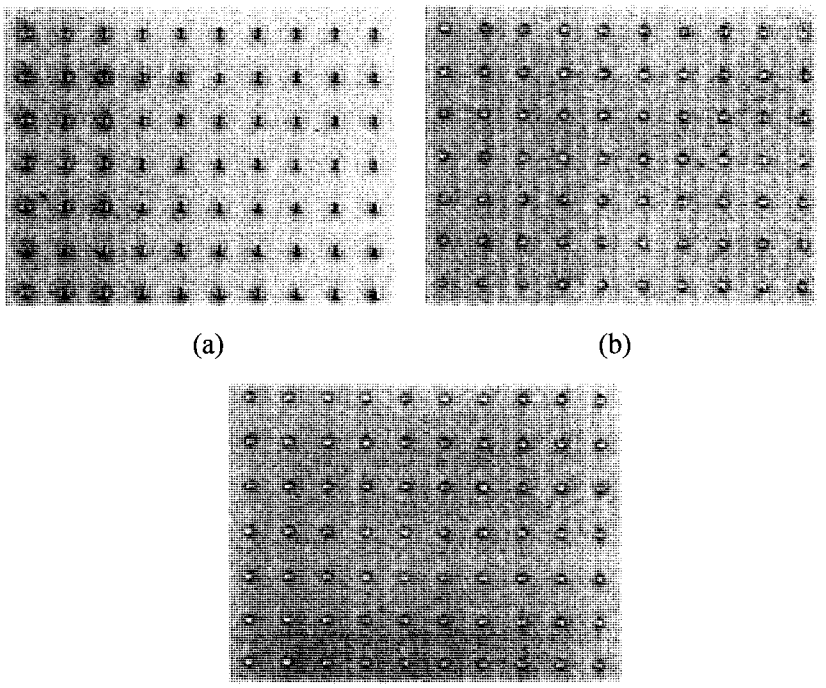

(a) (b)

(c)

Figure 20. Solderability test image for (a) ImAg, (b) ENIG, and (c) OSP-coated samples.

5.3 Cross-section of PCB

The cross-section of the PCB with ImAg, ENIG, and OSP-coated samples, prior to reflow, are shown in Figure 21a - c. As can be seen from Figure 15, no voids and other board problems were identified. However, the thickness of the NiP layer for the ENIG specimen was not 4 μm, which was what the suppliers stated. From the cross-section, the NiP layer thickness was approximately 2 μm, at the most. The very thin layers of Au, Ag, and OSP coatings were not determined due to SEM limitations.

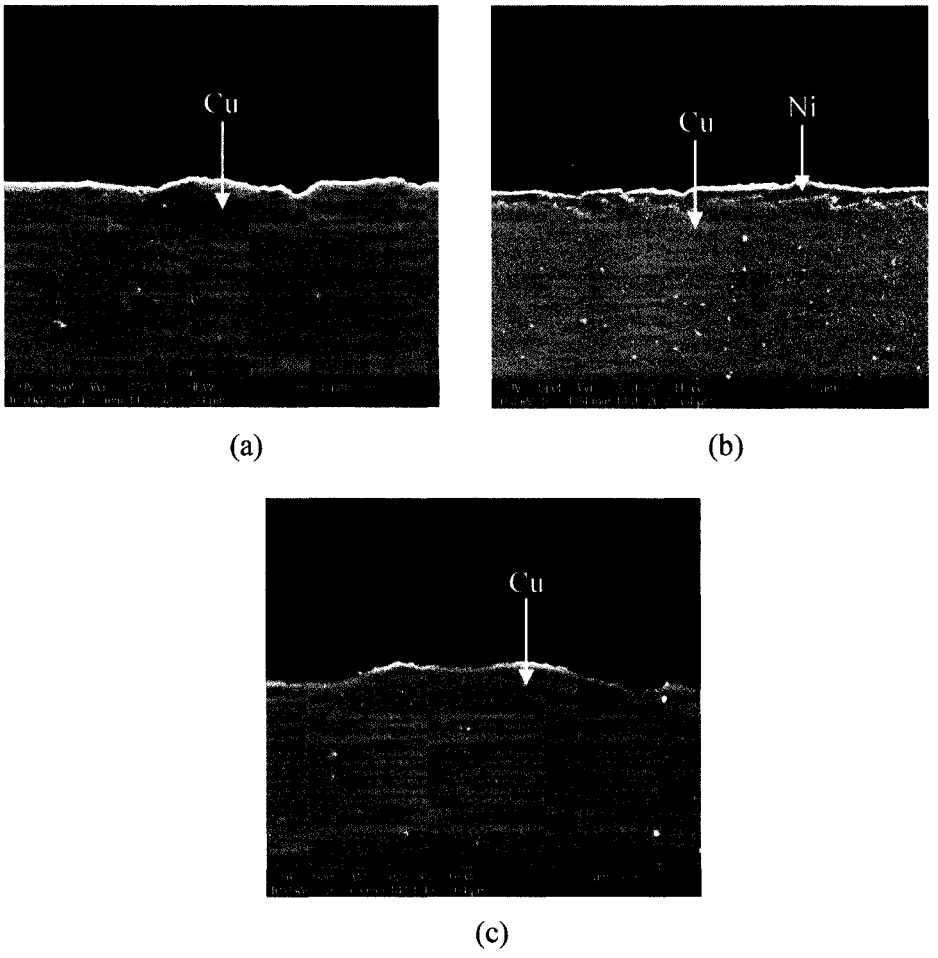

(a) (b)

(c)

Figure 21. Cross-section of PCB samples with (a) ImAg, (b) ENIG, and (c) OSP coatings.

5.4 ImAg-Coated Specimens

The intermetallic compounds that formed between the Cu pad and the solder ball, for the specimens coated with ImAg, after reflow and subsequent aging had a scallop-like morphology. The energy dispersive spectroscopy spectrum contained Cu and Sn peaks, from which it was concluded that the intermetallic compounds were of Cu-Sn composition, which is consistent with what was predicted using the phase diagram of this binary system. Ball shear test results revealed that there was only one mode of failure: pad lift. Details of the results are discussed below.

5.4.1 Intermetallic Compound Formation

Shown in Figure 22 is the interfacial microstructure of the specimens with ImAg coating after reflow. As can be seen from the micrograph, a scallop-like Cu-Sn intermetallic compound was formed between the solder ball and the Cu pad. Analysis with EDS confirmed the IMC composition to be Cu_6Sn_5, as shown in Figure 23. The thickness of this intermetallic compound is consistent and relatively uniform throughout the entire solder ball/Cu pad interface.

Needle-like microstructures were also found in the bulk solder, which were thought to be Ag_3Sn intermetallic compounds. Their composition was not verified due to SEM-EDS limitations. However, based on the phase diagrams for the Ag-Sn system, Ag_3Sn is the IMC that would precipitate in the bulk solder during solidification.

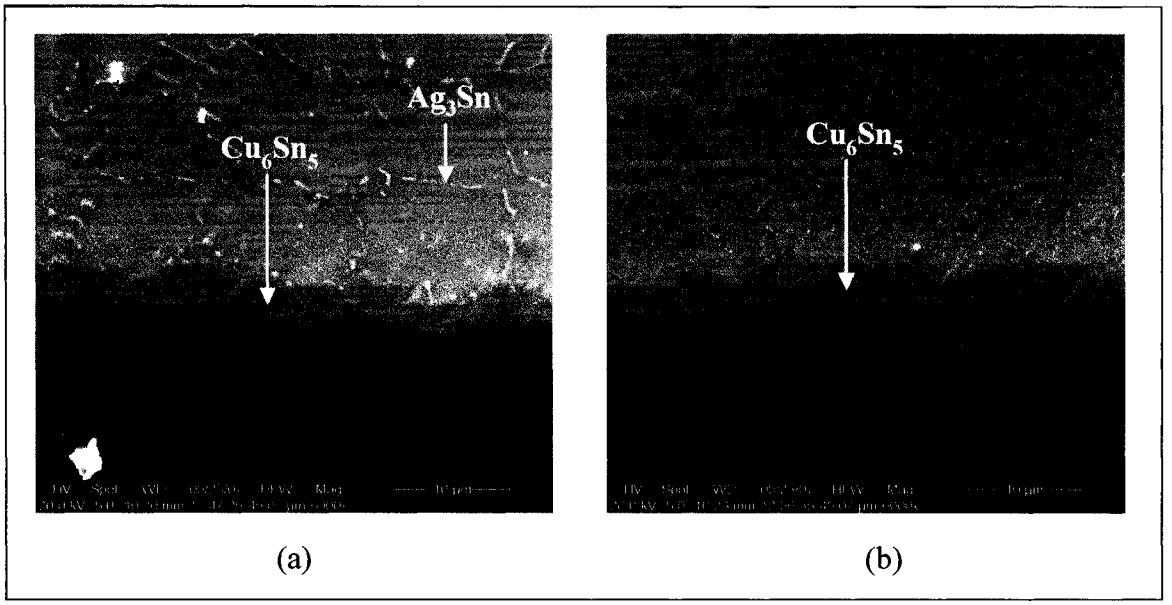

Figure 22. Interfacial microstructures of the ImAg-coated specimens after reflow for (a) solder ball from Specimen 1 and (b) solder ball from Specimen 2.

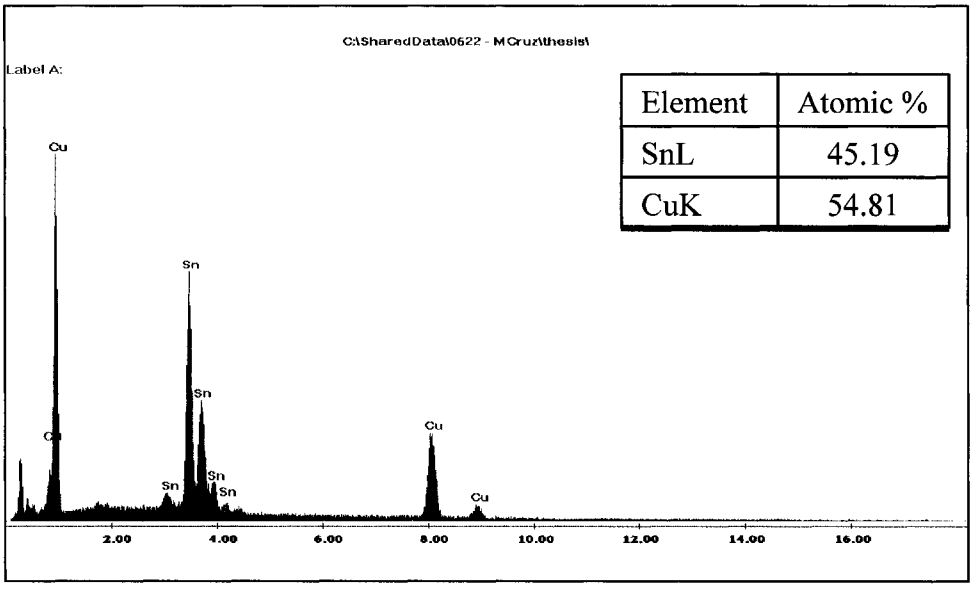

Figure 23. EDS spectrum of the Cu_6Sn_5 intermetallic compound for the ImAg-coated specimen after reflow.

The microstructure of the solder ball/Cu pad interface of the specimens that were reflowed then aged for 5 days at 150°C are shown in Figure 24. The scallop-like Cu-Sn intermetallic compounds were seen again at the interface of the solder ball and the Cu pad. The EDS spectrum of these intermetallic compounds is shown in Figure 25, from which it can be concluded that they are Cu_6Sn_5. These IMCs were thicker than the intermetallic compounds found in the reflowed specimens that were not aged. Voids, shown in Figure 24, were also found in the intermetallic compound layer, and at the interface between the Cu pad and the intermetallic compound layer. Some Ag_3Sn intermetallic compounds in the bulk solder were pebble-shaped and some were still needle-like, although shorter and wider than the Ag_3Sn needle-like structures that were found in the un-aged specimens.

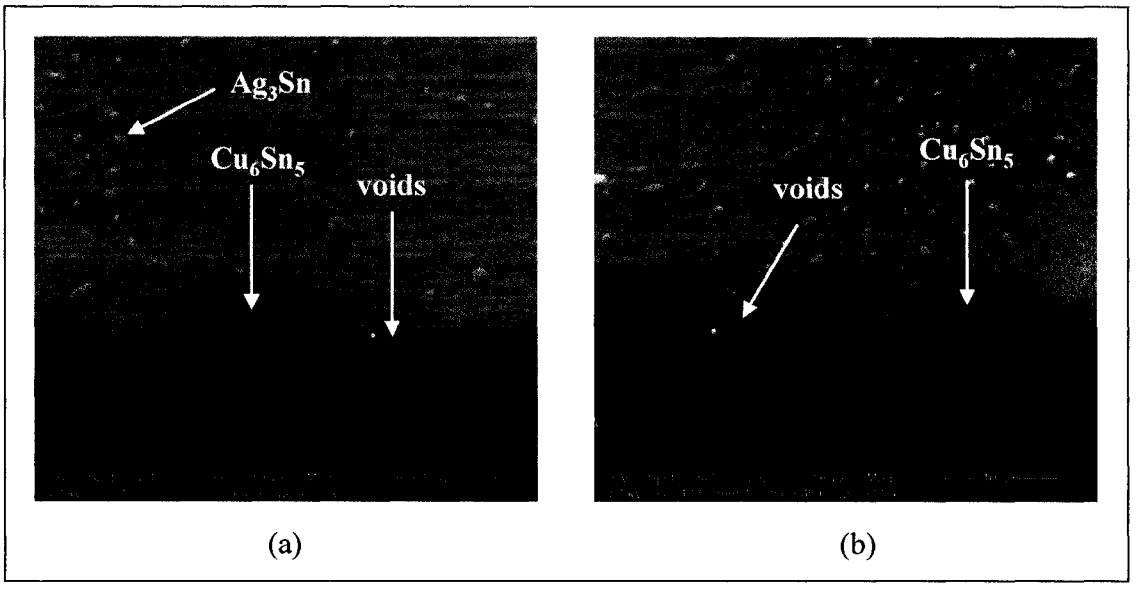

Figure 24. Interfacial microstructures of the ImAg-coated specimens after aging for 5 days at 150°C, after reflow, for (a) solder ball from Specimen 1 and (b) solder ball from Specimen 2.

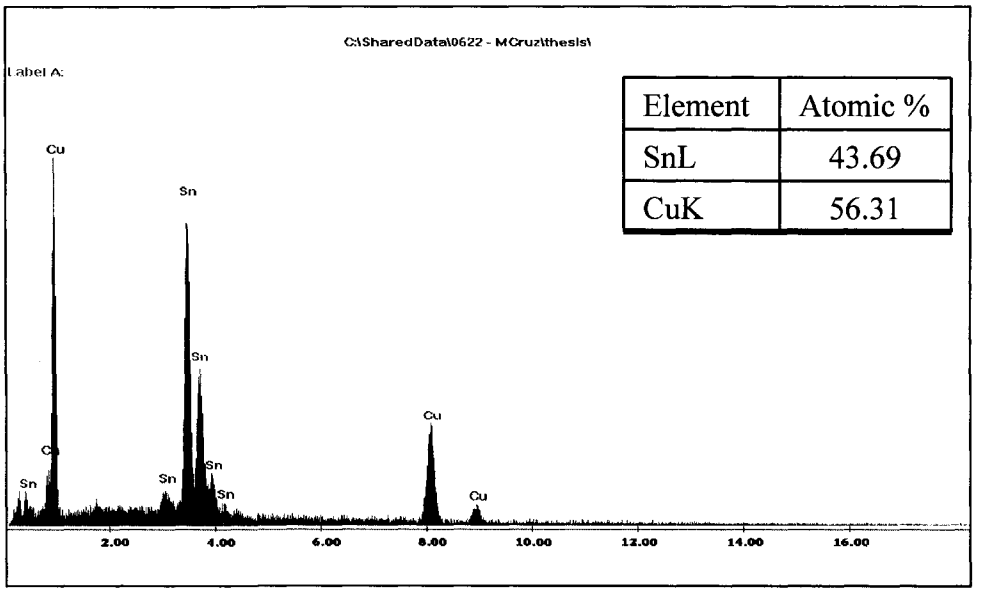

Figure 25. EDS spectrum of the Cu_6Sn_5 intermetallic compound for the ImAg-coated specimen after aging for 5 days at 150°C, after reflow.

Thicker Cu-Sn intermetallic compounds were found at the interface of the solder ball and the Cu pad after aging for 10 days at 150°C. The SEM micrographs of the cross-sections are shown in Figure 26, and the EDS spectrum for the intermetallic compound is shown in Figure 27. Voids were present at the interface between the Cu pad and the intermetallic layer, in the intermetallic layer, and some in the bulk solder. The number of voids in these specimens was greater than those found in the specimens that were aged for 5 days. Spalling of the Cu-Sn intermetallic compounds can also be seen in Figure 20b. The EDS spectrum in Figure 27 indicates that the IMC layer is Cu_6Sn_5. Almost all of the Ag_3Sn intermetallic compounds in the bulk solder were pebble-shaped, and no needle-like microstructures were seen. Some of these intermetallic compounds were larger than those found in the specimens that were aged for 5 days, and even larger than the specimens that were not aged.

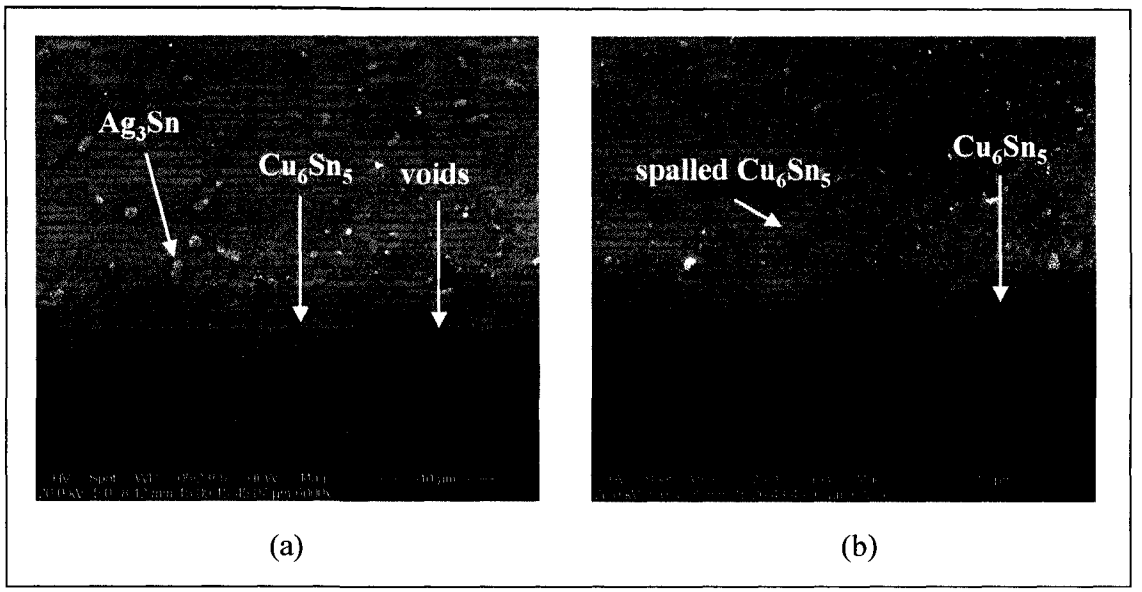

Figure 26. Interfacial microstructures of the ImAg-coated specimens after aging for 10 days at 150°C, after reflow, for (a) solder ball from Specimen 1 and (b) solder ball from Specimen 2.

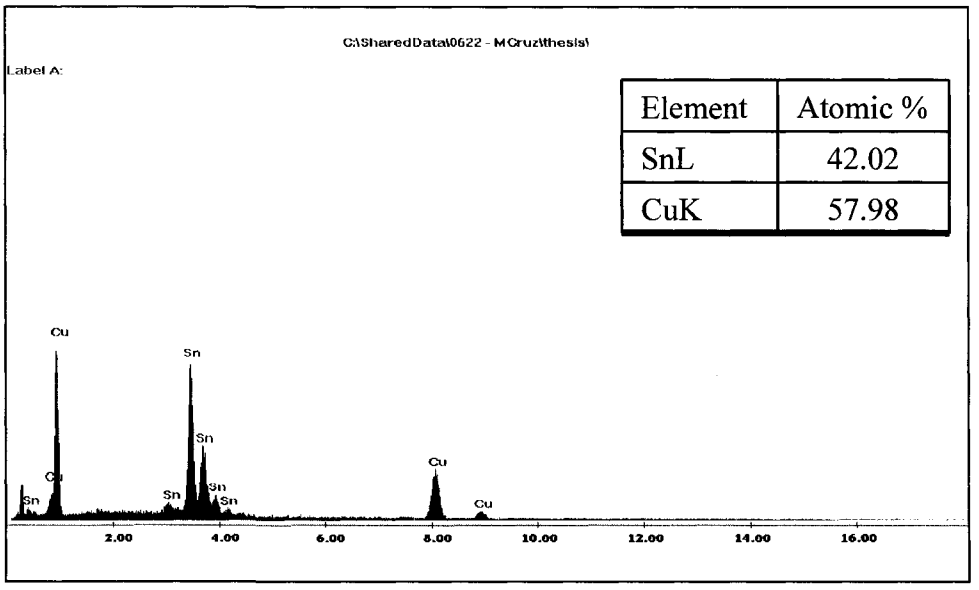

Figure 27. EDS spectrum of the Cu_6Sn_5 intermetallic compound for the ImAg-coated specimen after aging for 10 days at 150°C, after reflow.

The interfacial microstructures found for the specimens that were aged for 20 days are shown in Figure 28. The IMC layer was thicker than the IMC in the ImAg-coated specimens discussed thus far. Aside from the Cu_6Sn_5 intermetallic compound that was found at the solder ball/Cu pad interface, another Cu-Sn intermetallic compound layer was detected between the Cu pad and the Cu_6Sn_5 intermetallic compound. The composition of this intermetallic compound was verified via EDS, and was found to correspond to Cu_3Sn, as shown in Figure 29. Voids were still present, and this time, they were located within the Cu_6Sn_5 intermetallic compound, in the Cu_3Sn layer, and in the Cu_6Sn_5 intermetallic compound that spalled away from the substrate, as can be seen from Figure 28a. Several pebble-shaped and spherical Ag_3Sn intermetallic compounds were present, as seen in Figure 28b, in the solder matrix, although their number was less than those in the specimens that were aged for shorter aging times.

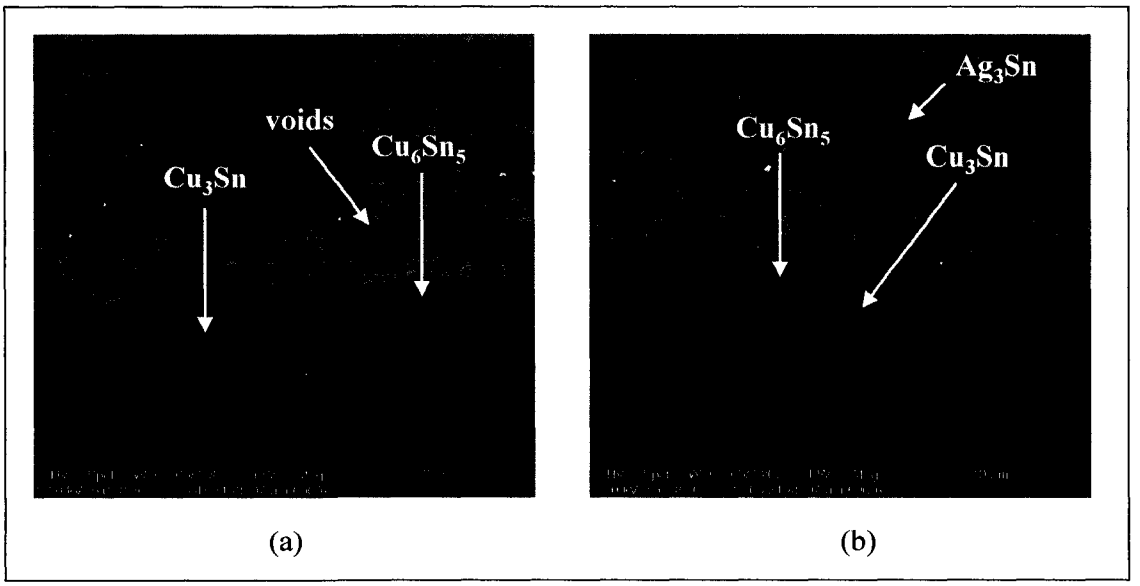

Figure 28. Interfacial microstructures of the ImAg-coated specimens after aging for 20 days at 150°C, after reflow, for (a) solder ball from Specimen 1 and (b) solder ball from Specimen 2.

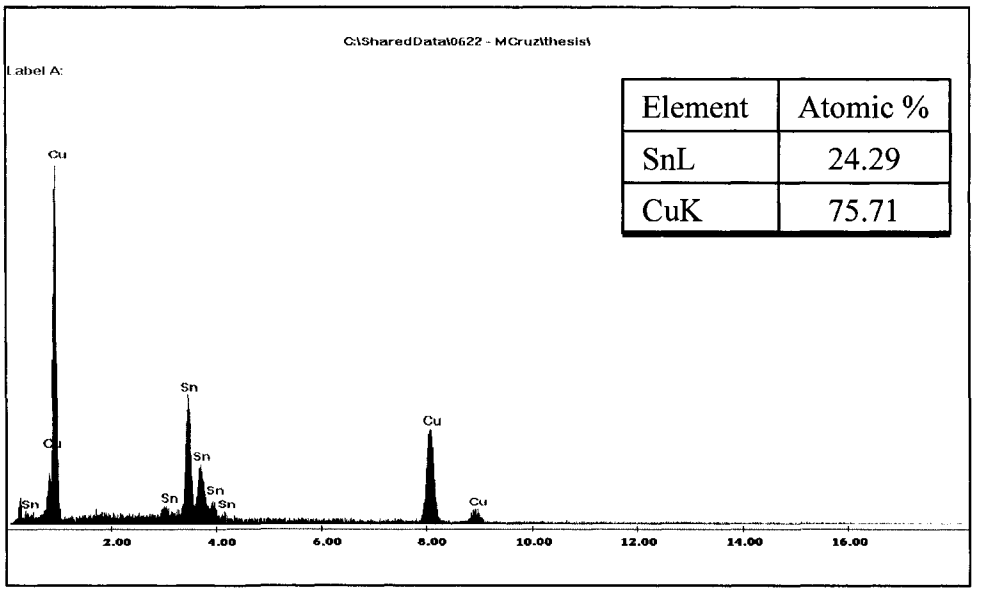

Figure 29. EDS spectrum of the Cu_3Sn intermetallic compound for the ImAg-coated specimen after aging for 20 days at 150°C, after reflow.

The microstructures of the interfacial reactions for the ImAg-coated specimens that were aged for 30 days are shown in Figure 30. The Cu_6Sn_5 intermetallic compounds have grown very thick, and about 1 μm thicker than in the ImAg-coated specimens that were aged for 20 days. More voids were also found at the Cu_6Sn_5 intermetallic compound/Cu pad interface. The Cu_3Sn IMC layer, the EDS spectrum of which is shown in Figure 31, was still present, although it was not possible to determine if it had grown thicker. Spalling of the Cu_6Sn_5 intermetallic compound was still found, although the size of these spalled IMCs appeared to be smaller than those that were aged for 10 days. Spherical-shaped Ag_3Sn intermetallic compounds were still found in the solder matrix, and appeared to have grown larger than those in the specimens with shorter aging times. The number of these IMCs appeared to have been reduced, however, at this aging time.

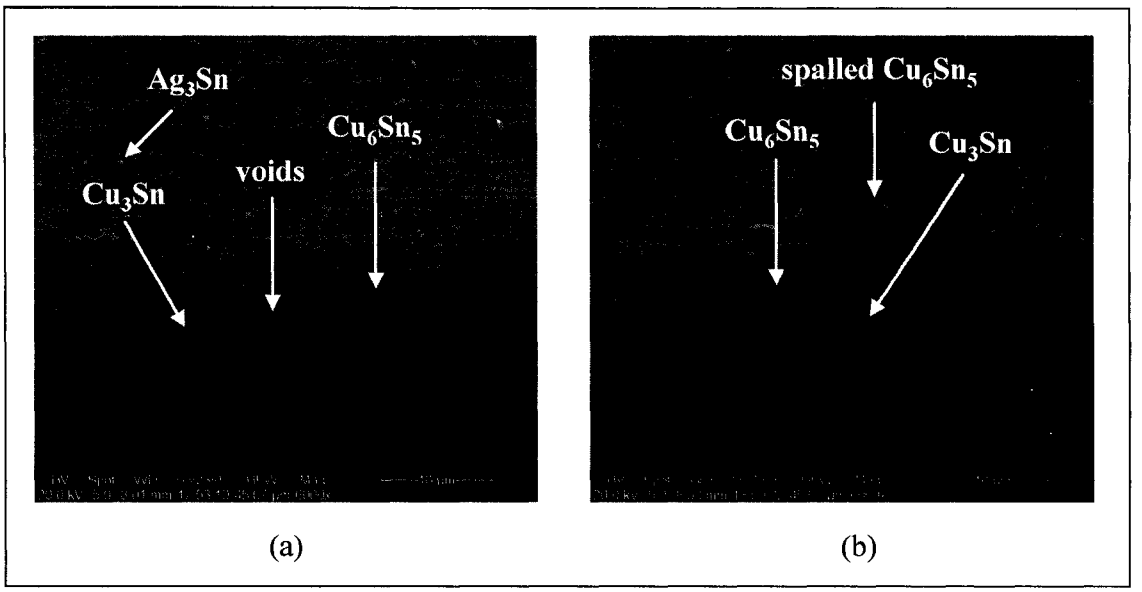

Figure 30. Interfacial microstructures of the ImAg-coated specimens after aging for 30 days at 150°C, after reflow, for (a) solder ball from Specimen 1 and (b) solder ball from Specimen 2.

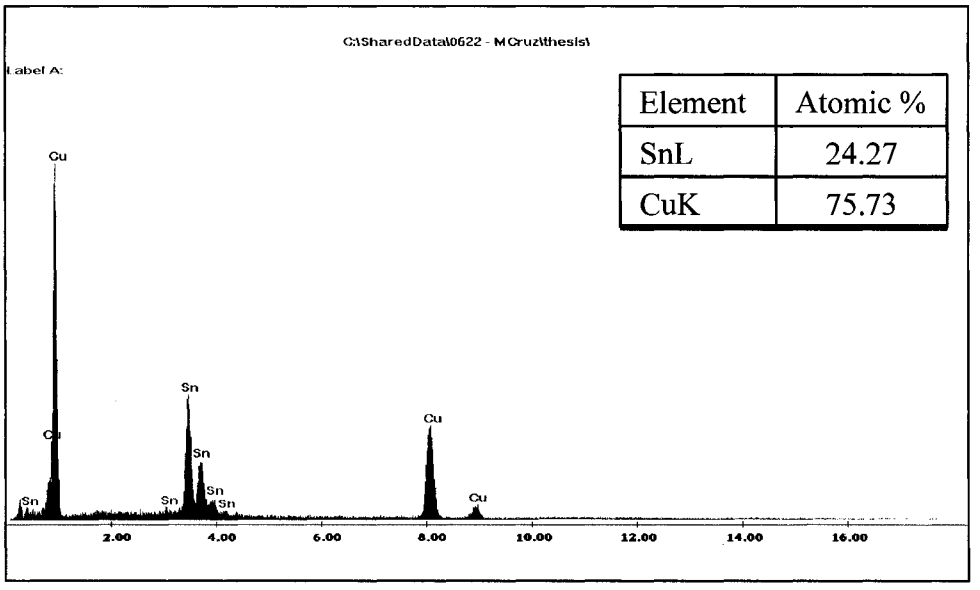

Element	Atomic %
SnL	24.27
CuK	75.73

Figure 31. EDS spectrum of the Cu_3Sn intermetallic compound for the ImAg-coated specimen after aging for 30 days at 150°C, after reflow.

To determine the effect of aging on the size of the intermetallic compounds, the 10 largest thicknesses, t_{max}, and the 10 smallest IMC thicknesses, t_{min}, were measured. The averages of t_{max} and t_{min}, shown in Table 13, were then plotted as a function of aging time. The raw data are tabulated in Appendix B.

Table 13. Average IMC thickness for ImAg-coated specimens.

Aging Time (days)	Average of t_{max} IMC (μm)	Average of t_{min} IMC (μm)
0	4.5	3.6
5	5.8	4.9
10	7.2	5.7
20	8.5	7.2
30	9.4	7.6

The plot of the averages of the intermetallic compound (Cu_6Sn_5 + Cu_3Sn) thicknesses, t_{max} and t_{min}, as a function of aging time for the ImAg-coated specimens is shown in Figure 32. The graph exhibits a parabolic relationship between IMC thickness and aging time, which is consistent with the findings of other researches, and also consistent with solid-state diffusion controlled growth. To determine the growth rate constant of the Cu-Sn intermetallic compounds at 150°C, the averages of the 10 highest IMC thicknesses, t_{max}, were plotted as a function of the square root of the aging time, as shown in Figure 33. The basis for this assumption is Equation 3, expressed as:

$$\delta = \delta_o + k\sqrt{t} \qquad \text{Equation 3}$$

where: δ is the thickness of the IMC at time t

δ_o is the thickness of the IMC at time zero

k is the growth rate constant at the temperature considered

Hence, the slope from Figure 33 gives the growth rate constant of the Cu-Sn IMCs at the aging temperature of 150°C. From Figure 33, the growth rate constant is 3.152×10^{-3} $\mu m/(sec)^{1/2}$.

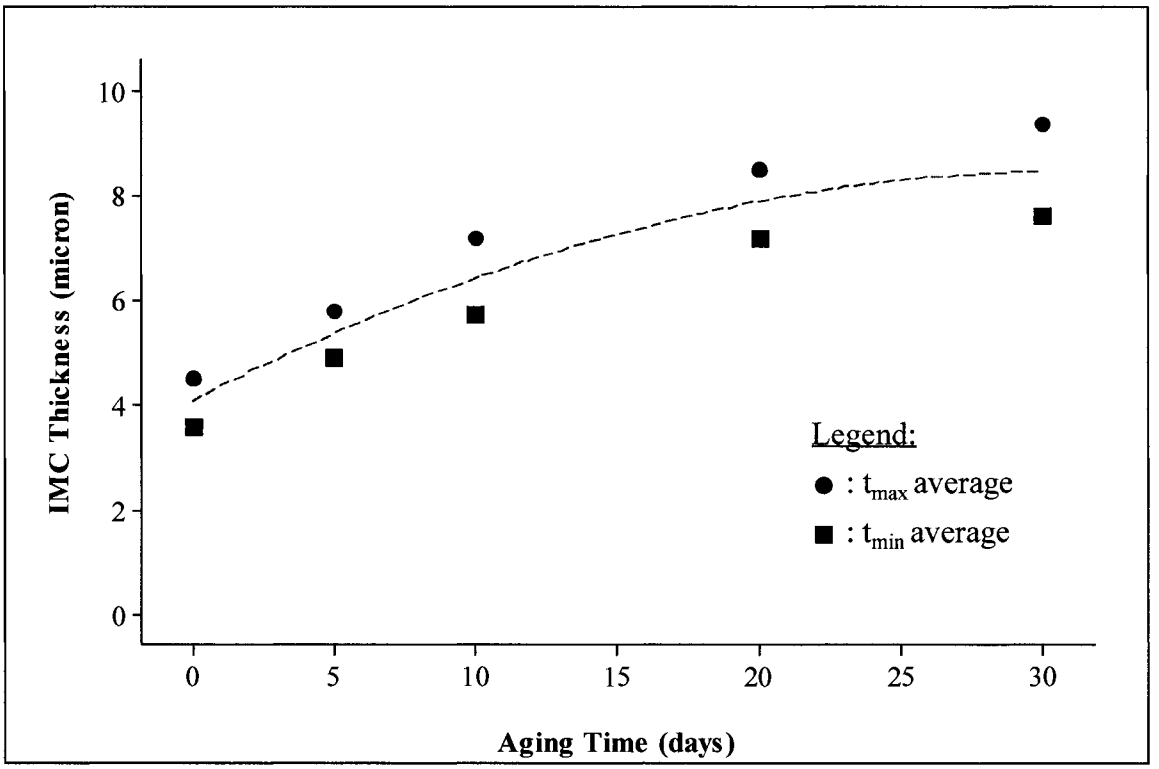

Figure 32. IMC thickness as a function of aging time plot for the ImAg-coated specimens.

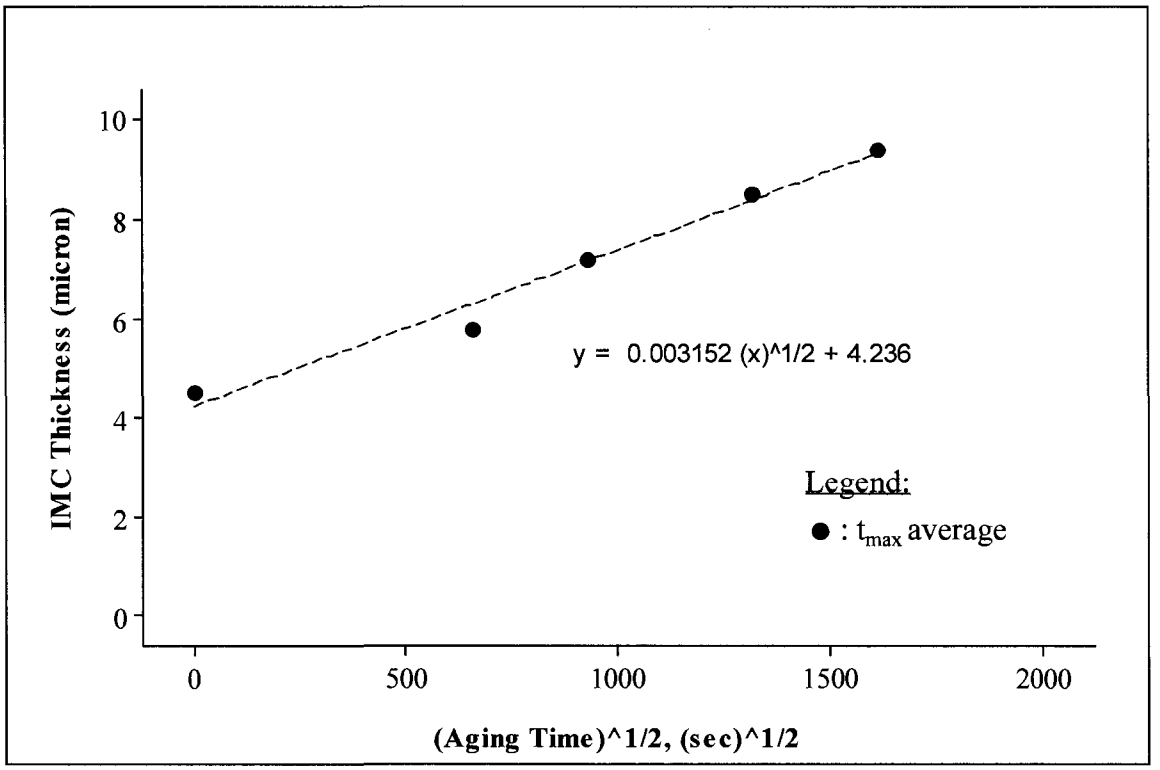

Figure 33. IMC thickness as a function of the sqrt of aging time plot for the ImAg-coated specimens.

5.4.2 Shear Strength

The average ball shear strength results for the specimens with ImAg coating are shown in Table 14. The failure modes for ball shear based on JESD22-B117, the industry standard for solder ball shear [65], are described in Table 15. For the ImAg-coated specimens, only one failure mode was found for ball shear test, namely, pad lift. An optical micrograph of this failure mode is shown in Figure 34. From Figure 34, it can be seen that the base material is ruptured. The entire solder ball was lifted off from the pad and no solder ball residue remained in the pad.

Table 14. Average and standard deviation of ball shear strength for the ImAg-coated specimens.

Coating Type	Aging Time (days)	Average Shear Strength (MPa)	Standard Deviation (MPa)
ImAg	0	31	3
	5	28	3
	10	31	3
	20	31	3
	30	30	2

Table 15. Ball shear failure mode types based on JESD22-B117 [65].

Failure Mode Type	Description
Ductile	Fracture within the bulk solder ball
Pad Lift	Base metal pad, that may include ruptured base material, is lifted with the solder ball
Ball Lift	Solder ball is lifted from the pad, with the pad not completely covered with solder. Pad plating is exposed.
Interfacial Break	Fracture at the solder/intermetallic surface or intermetallic surface/base metal interface

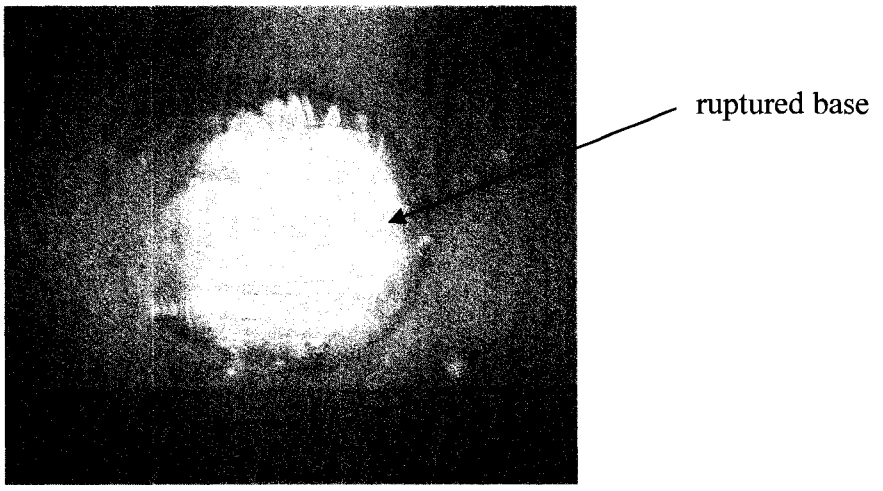

Figure 34. Optical micrograph of pad lift failure found in the ImAg-coated specimens.

The ball shear test results are plotted in Figure 35, with the raw data being tabulated in Appendix C. As can be seen from Figure 35, there was practically no change in the shear strength of the solder joint as aging time was increased. However, when this trend was compared with the results from the student t-test calculations, a different behavior was obtained. A statistical difference in ball shear strength after reflow and up to 10-day aging was found. The shear strength then remained constant until 30-day aging. The difference in finding between the trend in the actual plot of the specimens and the t-test results may be attributed to the presence of voids, the coarsening of the Ag_3Sn intermetallic compounds, the spalling of the Cu_6Sn_5 intermetallic compound, and most importantly, the mode of ball shear failure.

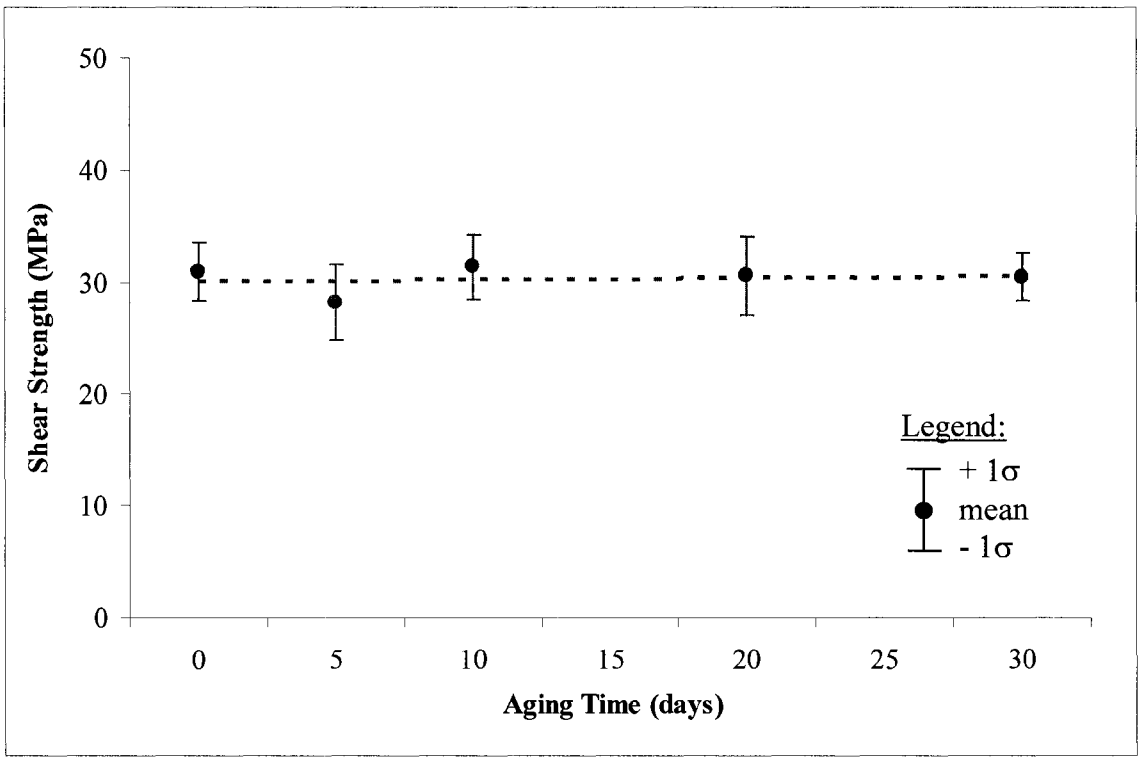

Figure 35. Ball shear test results for the ImAg-coated specimens.

5.5 ENIG-Coated Specimens

The intermetallic compounds that formed between the Cu pad and the solder ball, for the specimens coated with ENIG, after reflow and subsequent aging had a scallop-like morphology, that later transformed into a layered-type morphology. The energy dispersive spectroscopy spectrum contained Cu, Ni, and Sn peaks. Two types of failure modes were found after ball shear, namely, pad lift and ductile rupture. These results are presented below.

5.5.1 Intermetallic Compound Formation

The interfacial microstructures of the ENIG specimens after reflow are shown in Figure 36. The thickness of the Ni layer was greatly reduced after reflow, compared to the thickness of the Ni layer in the virgin boards. Intermetallic compounds formed at the solder ball/Ni interface. Verification with EDS revealed that these IMCs have a composition of $(Cu,Ni)_6Sn_5$, as shown in Figure 37. Spalling of this Cu-Ni-Sn layer after reflow can also be seen in Figure 36b. Needle-like intermetallic compounds at the bulk solder, which are thought to be Ag_3Sn, were also seen. Voids between the Ni layer and the Cu pad were also found.

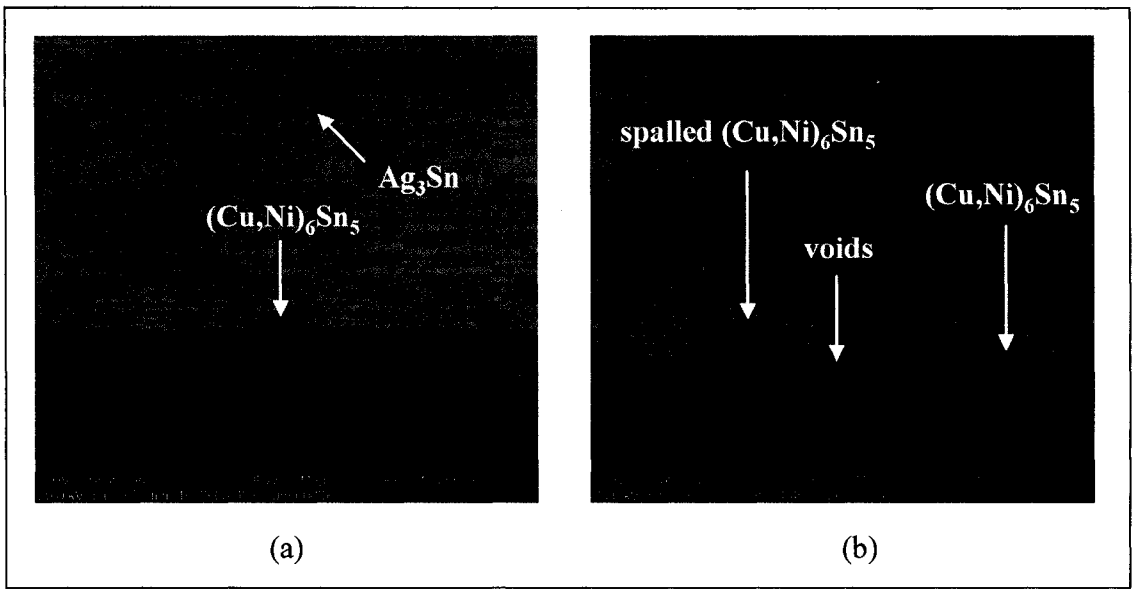

Figure 36. Interfacial microstructures of the ENIG-coated specimens after reflow for (a) solder ball from Specimen 1 and (b) solder ball from Specimen 2.

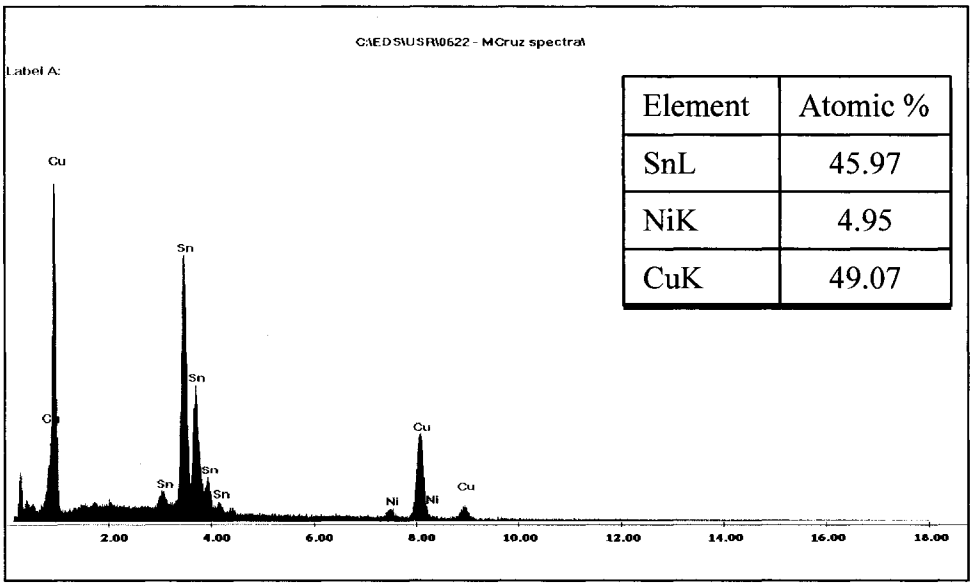

Element	Atomic %
SnL	45.97
NiK	4.95
CuK	49.07

Figure 37. EDS spectrum of the $(Cu,Ni)_6Sn_5$ intermetallic compound for the ENIG-coated specimen after reflow.

The interfacial microstructures that formed for the ENIG-coated specimens that were aged for 5 days at 150°C after reflow are shown in Figure 38. The scallop-like Cu-Ni-Sn intermetallic compounds became thicker and more uniform than the specimens with no aging. The EDS spectrum of these intermetallic compounds is shown in Figure 39. Spalling of the $(Cu,Ni)_6Sn_5$ intermetallic compounds can also be seen in Figure 38a. What used to be needle-like Ag_3Sn IMCs in the solder matrix have transformed into pebble-shaped microstructures. The voids at the Ni layer/Cu pad interface also became larger.

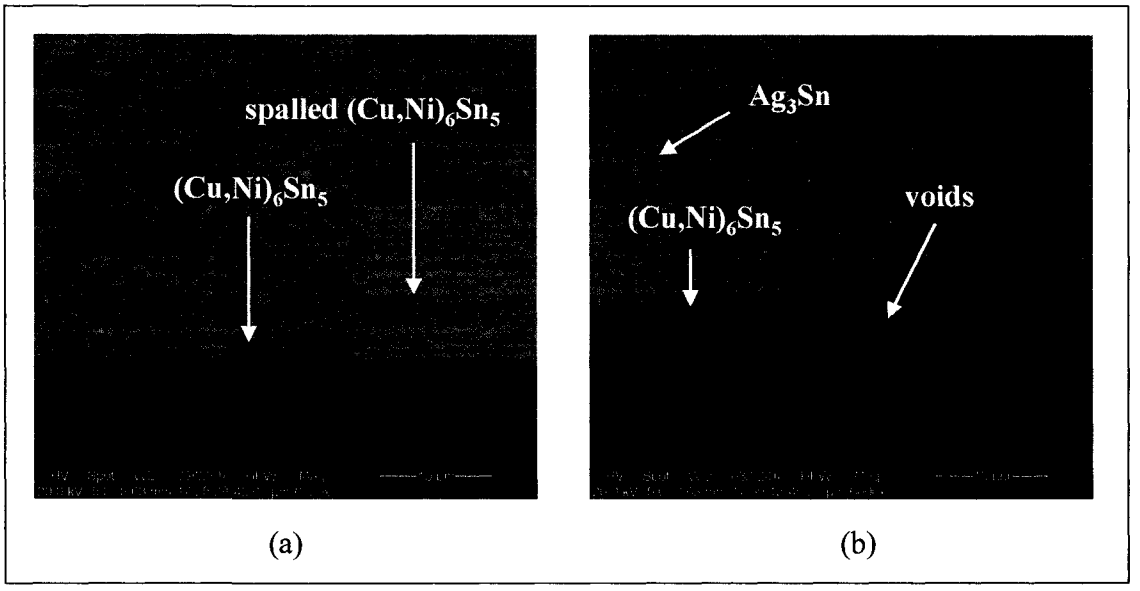

Figure 38. Interfacial microstructures of the ENIG-coated specimens after aging for 5 days at 150°C, after reflow, for (a) solder ball from Specimen 1 and (b) solder ball from Specimen 2.

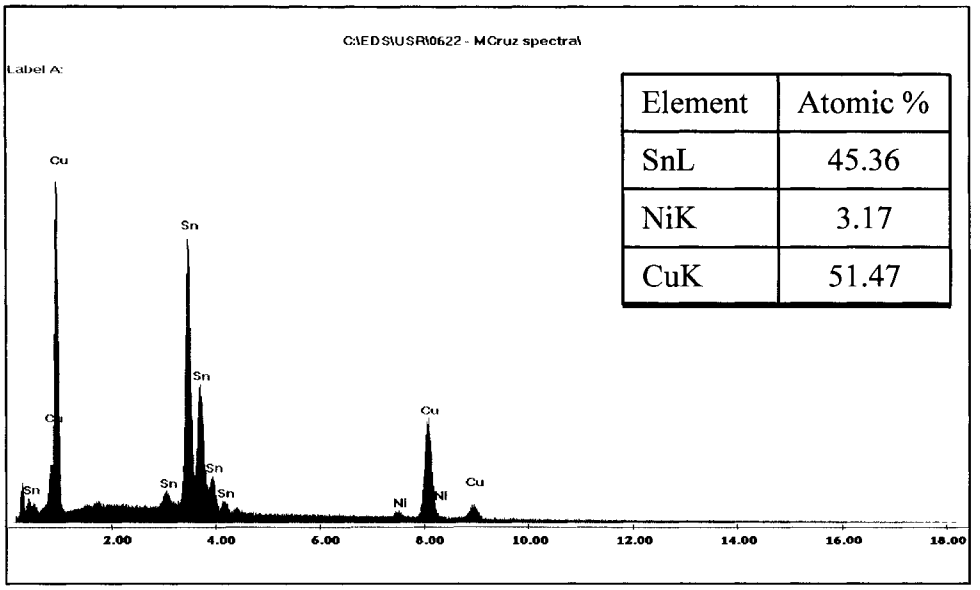

Element	Atomic %
SnL	45.36
NiK	3.17
CuK	51.47

Figure 39. EDS spectrum of the $(Cu,Ni)_6Sn_5$ intermetallic compound for the ENIG-coated specimen after aging for 5 days at 150°C, after reflow.

The interfacial intermetallic compounds continued to become thicker as the specimens were aged for 10 days. Instead of the scallop-like morphology found in the ENIG-coated specimens that were aged for 5 days after reflow, these intermetallic compounds have a layered-type morphology. The Ni layer appears to have "disappeared", although the EDS spectrum shown in Figure 41 revealed the existence of Ni in the $(Cu,Ni)_6Sn_5$ intermetallic compound. The Ni layer, which was 2 μm thick, "dissolved and interacted" with Sn and Cu to form the $(Cu,Ni)_6Sn_5$. If the Ni did not dissolve, the Cu cannot interact with the Sn. As can be seen from Figure 40b, spalling of the intermetallic compounds was found, and the size of these spalled IMCs was larger than those found in the specimens that were aged for 5 days. The size of the voids also became larger as the aging time was increased. Most of the pebble-shaped Ag_3Sn intermetallic compounds became spherical in shape.

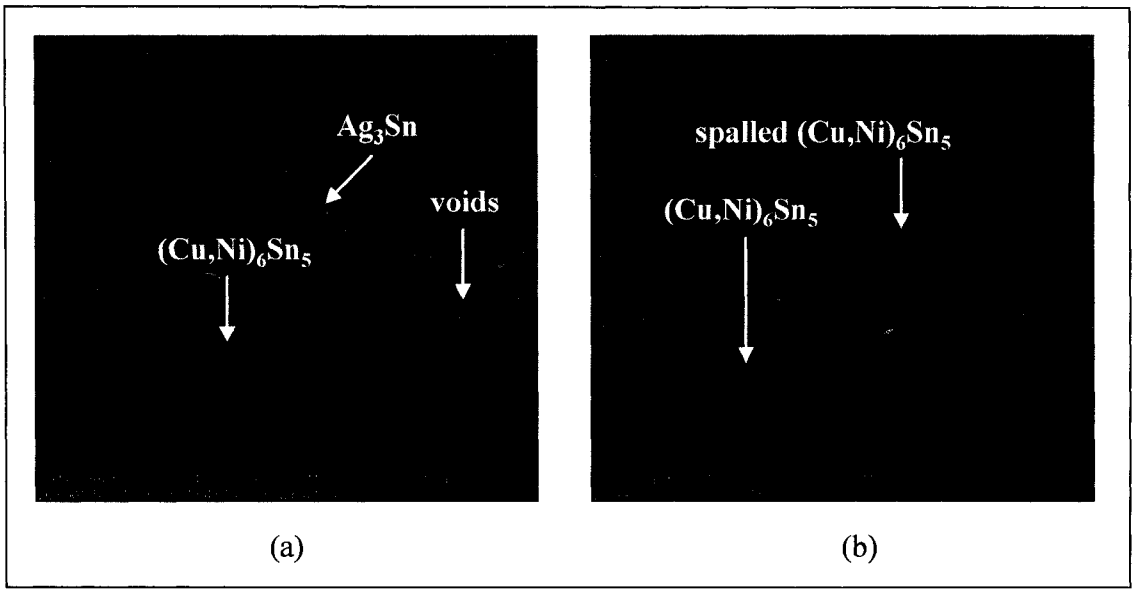

Figure 40. Interfacial microstructures of the ENIG-coated specimens after aging for 10 days at 150°C, after reflow, for (a) solder ball from Specimen 1 and (b) solder ball from Specimen 2.

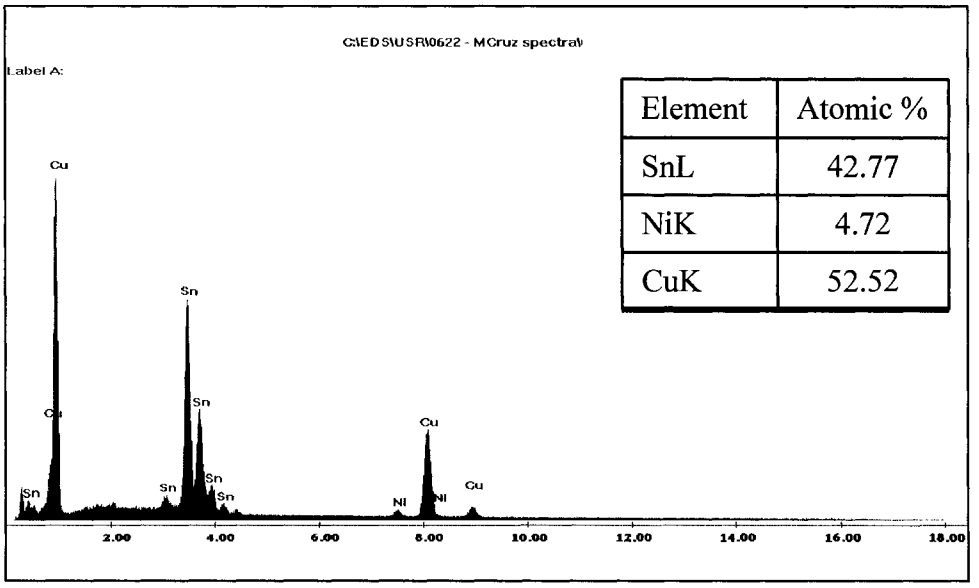

Element	Atomic %
SnL	42.77
NiK	4.72
CuK	52.52

Figure 41. EDS spectrum of the $(Cu,Ni)_6Sn_5$ intermetallic compound for the ENIG-coated specimen after aging for 10 days at 150°C, after reflow.

Bigger voids, as compared to those found in the ENIG-coated specimens that were aged for 10 days after reflow, were seen for the specimens that underwent aging for 20 days, as shown in Figure 42. The layered-type morphology of the intermetallic compound at the interface became thicker. Spalling of the intermetallic compounds was still found, and these spalled IMCs had migrated farther away from the substrate. The number of spherical-shaped Ag_3Sn intermetallic compounds in the solder matrix became smaller, but the size of the precipitates became bigger. At this aging time, another layer was detected between the Cu pad and the $(Cu,Ni)_6Sn_5$ intermetallic compound. Using EDS, the composition of this thin layer was determined to be $(Cu,Ni)_3Sn$, as shown in Figure 43. Although the Ni layer was no longer visible, a small amount was still detected. It had interacted with Cu and Sn to form the $(Cu,Ni)_3Sn$ IMC.

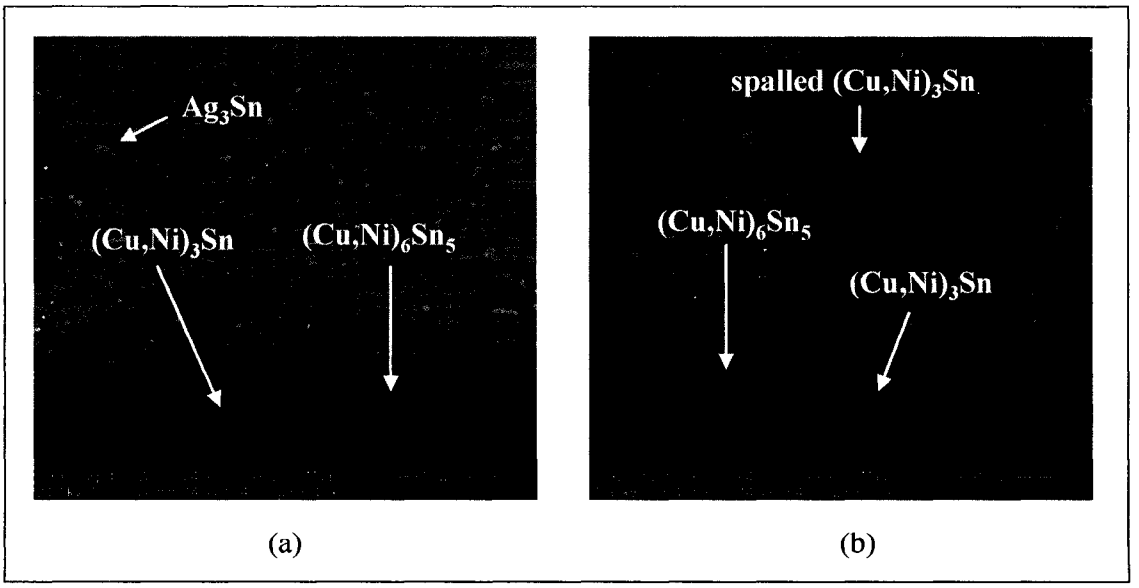

Figure 42. Interfacial microstructures of the ENIG-coated specimens after aging for 20 days at 150°C, after reflow, for (a) solder ball from Specimen 1 and (b) solder ball from Specimen 2.

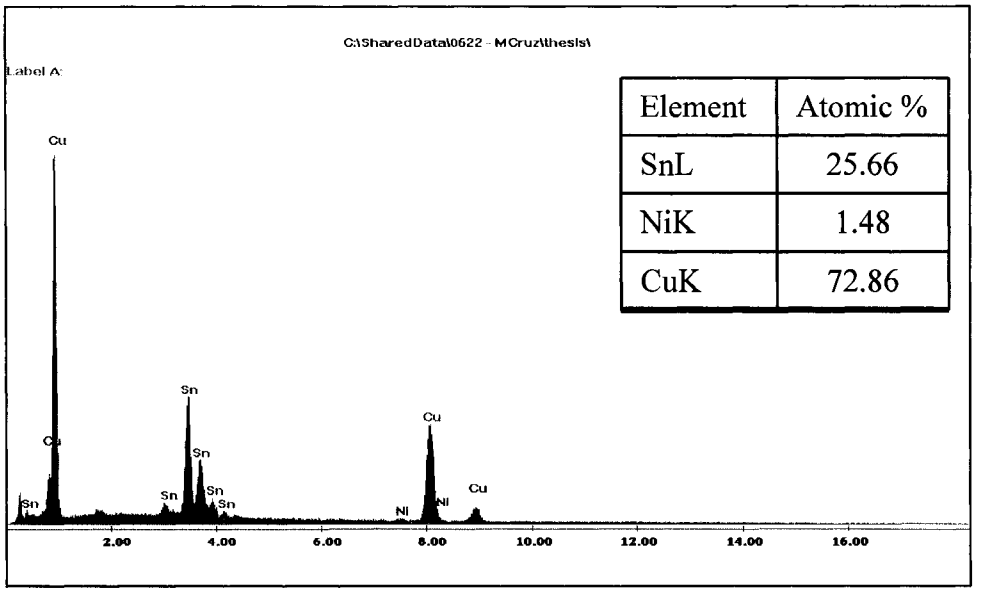

Element	Atomic %
SnL	25.66
NiK	1.48
CuK	72.86

Figure 43. EDS spectrum of the $(Cu,Ni)_3Sn$ intermetallic compound for the ENIG-coated specimen after aging for 20 days at 150°C, after reflow.

The morphology of the interfacial microstructures found in the specimens that were aged for 30 days is shown in Figure 44. The $(Cu,Ni)_6Sn_5$ intermetallic layer became thicker. The voids at the $(Cu,Ni)_6Sn_5$ intermetallic compound, and at the interface between the Cu pad and the $(Cu,Ni)_6Sn_5$ layer, became larger in diameter. The number of these voids also became larger as the aging time was increased. There was an increase in the size of the Ag_3Sn intermetallic compounds, although their number decreased. Spalling was still seen at this aging time. The $(Cu,Ni)_3Sn$ intermetallic layer was still detected, although the Ni content was even lower than at the previous aging time, which is thought to be due to its continuous diffusion in Cu. The EDS spectrum for this IMC is shown in Figure 45.

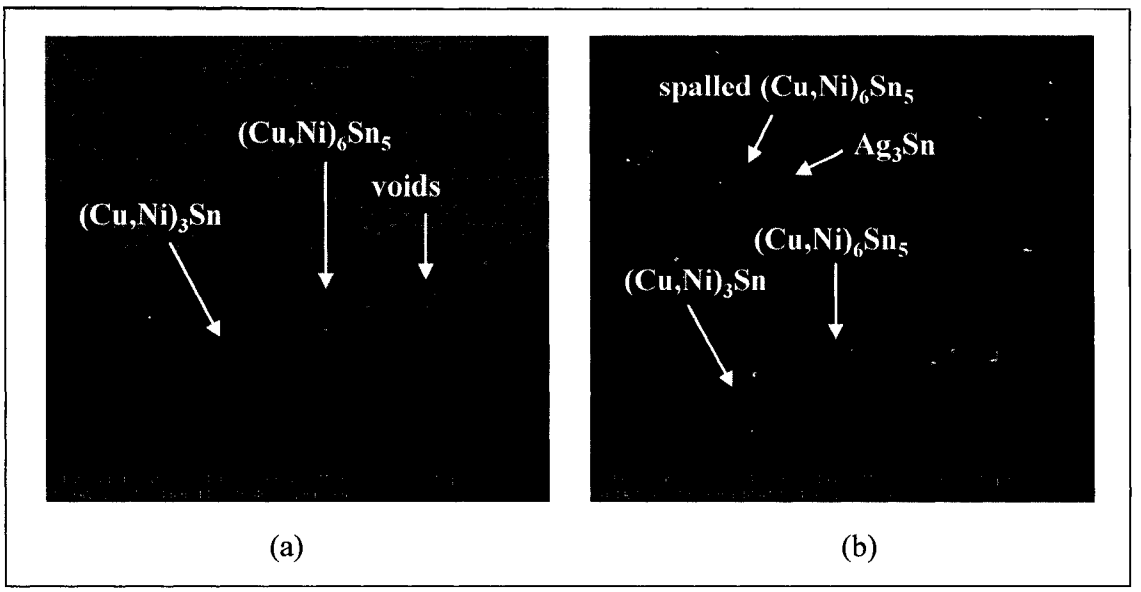

Figure 44. Interfacial microstructures of the ENIG-coated specimens after aging for 30 days at 150°C, after reflow, for (a) solder ball from Specimen 1 and (b) solder ball from Specimen 2.

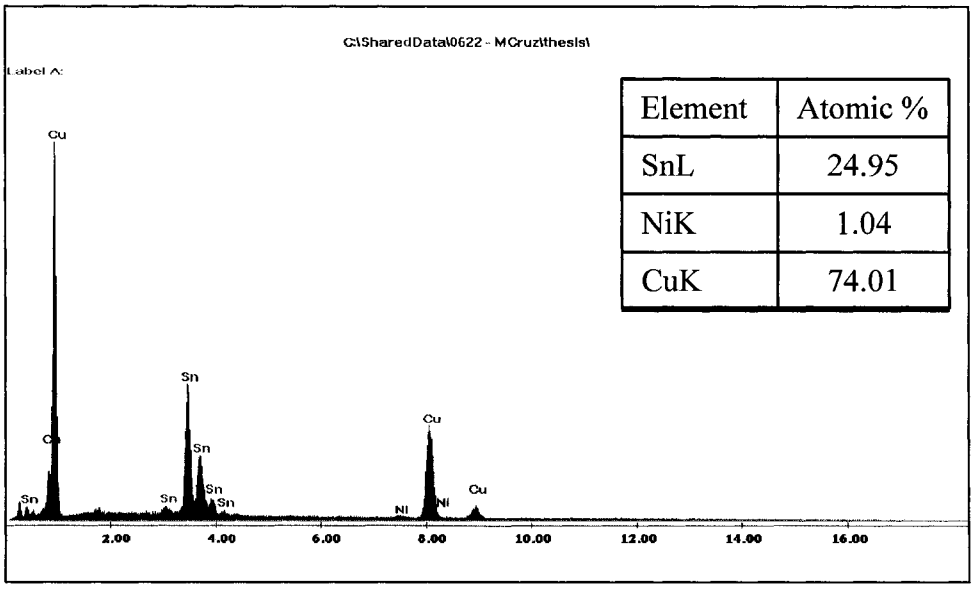

Element	Atomic %
SnL	24.95
NiK	1.04
CuK	74.01

Figure 45. EDS spectrum of the $(Cu,Ni)_3Sn$ intermetallic compound for the ENIG-coated specimen after aging for 30 days at 150°C, after reflow.

The 10 highest IMC thicknesses, t_{max}, and the 10 lowest IMC thicknesses, t_{min}, were measured for the ENIG-coated specimens. The averages of these measurements are shown in Table 16. The raw data are tabulated in Appendix B.

Table 16. Average IMC thickness for the ENIG-coated specimens.

Aging Time (days)	Average of t_{max} (μm)	Average of t_{min} (μm)
0	3.4	2.0
5	4.1	3.0
10	4.9	3.6
20	8.2	6.3
30	9.3	6.7

The plot of the averages of IMC thickness ($(Cu,Ni)_6Sn_5 + (Cu,Ni)_3Sn$), t_{max} and t_{min}, as a function of aging time for the ENIG-coated specimens is shown in Figure 46. The IMC thickness increased as the aging time was increased. The relationship between IMC thickness and aging time was not parabolic, and hence, the IMC thickness as a function of the square root of aging time was not plotted.

5.5.2 Shear Strength

Ball shear tests were also performed to determine the effect of aging on the solder joint strength. The average ball shear strengths and the corresponding standard deviations of the solder joints are shown in Table 17. For these specimens, the dominant failure modes were pad lift (majority) and ball shear (minority). An optical micrograph of the ball shear failure mode is shown in Figure 47. The pad lift failure mode was the

same as the pad lift found in the ImAg-coated specimens. The ball shear raw data and the statistical calculations obtained from student t-test are included in Appendix C.

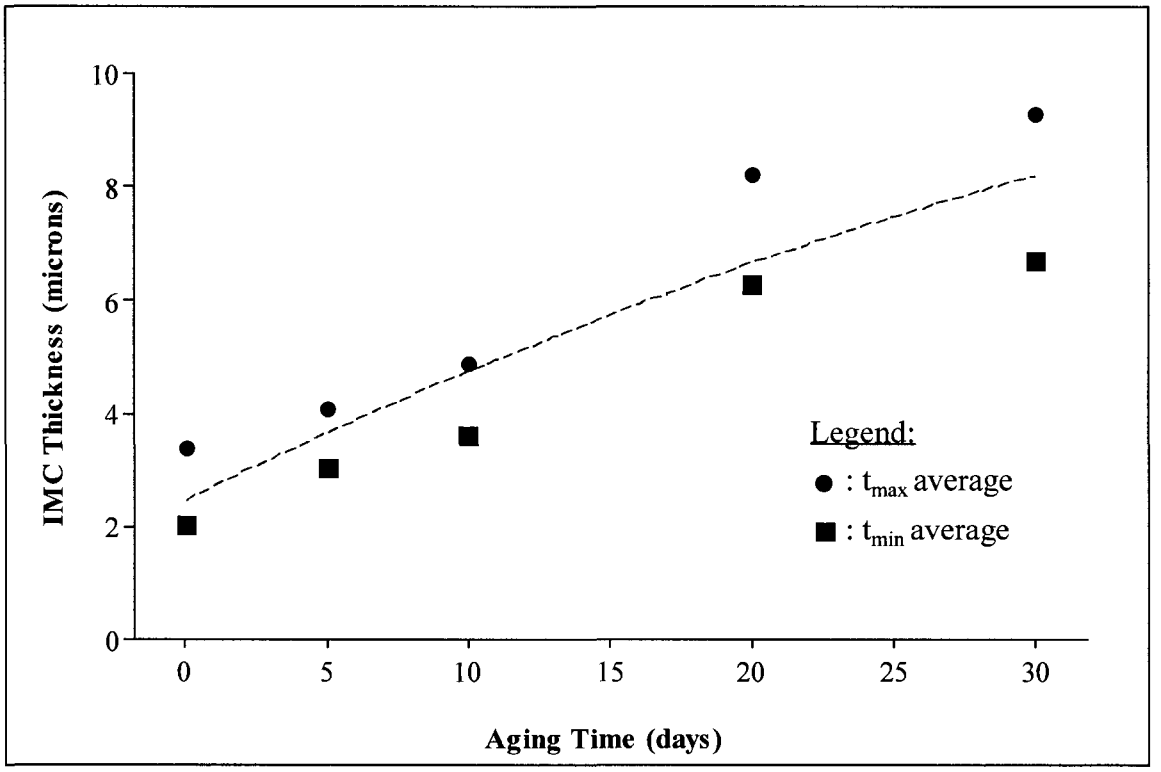

Figure 46. IMC thickness as a function of aging time plot for the ENIG-coated specimens.

Table 17. Average and standard deviation of ball shear strength for the ENIG-coated specimens.

Coating Type	Aging Time (days)	Average Shear Strength (MPa)	Standard Deviation (MPa)
ENIG	0	36	2
	5	32	5
	10	34	3
	20	34	2
	30	31	3

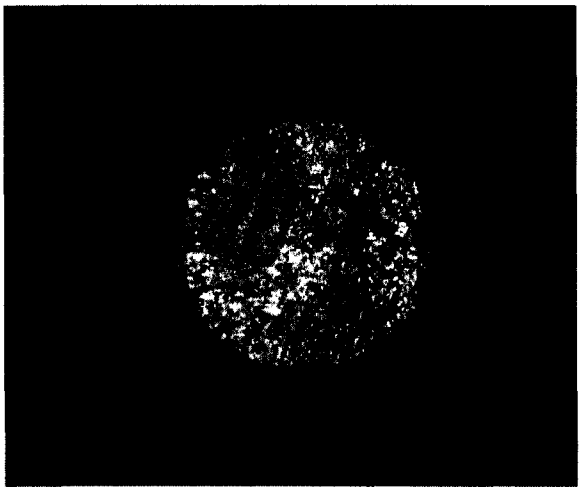

Figure 47. Optical micrograph of ball shear failure mode for the ENIG-coated specimen.

From Figure 48, the graph of the ball shear strength as a function of aging time exhibits linear behavior, with a 15% decrease in the mean shear strength after 30-day aging. The paired student t-test calculations showed that there was a statistical difference in ball shear strength between after reflow and 5-day aging, and the shear strength remained the same until 20-day aging, and decreased again after that. The difference between the two findings may be due to the presence of voids, ripening of the Ag_3Sn intermetallic compounds, and spalling of the interfacial intermetallic compounds, all of which could not be accounted for in the student t-test calculations. In addition, if the failure mode was pad lift, little to no difference should be found in the shear strengths, regardless of aging time, since the solder balls are well adhered to the substrate. For ball shear failure mode, the solder balls are sheared along the bulk solder, not along the solder joint. Hence, it is the Ag_3Sn intermetallic compounds at the bulk solder that could affect the shear strength, and not the Cu-Ni-Sn IMCs at the solder joint. The reduction in the shear strength with increasing aging time may be attributed to the coarsening of the

Ag_3Sn intermetallic compounds. Initially, these IMCs were smaller in size, leading to higher strength of the material. As the specimen was aged, these IMCs continued to grow bigger, making the material weaker, hence, lower shear strength. This would explain the trend found in the graph, i.e., decrease in shear strength.

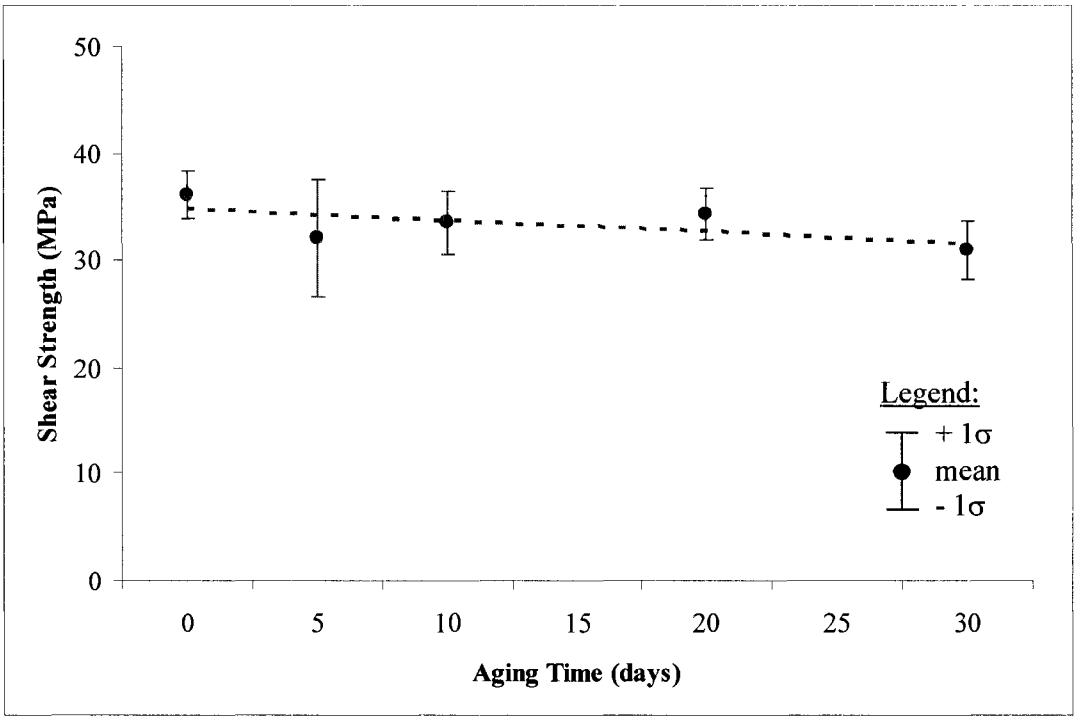

Figure 48. Ball shear test results for the ENIG-coated specimens.

The ball shear test results for the ENIG-coated specimens, classified according to failure mode, are shown in Table 18. Some of the reflowed specimens had pad lift failure while some had ductile failure. The same was true for the specimens that were aged for 5 days. The specimens that were aged for 10, 20, and 30 days only exhibited pad lift failure.

Table 18. Average ball shear strength of the ENIG-coated specimens per failure mode.

Aging Time	Average Shear Strength (MPa)	Standard Deviation (MPa)	Failure Mode
0	36	2.3	Pad Lift
	37	2.1	Ductile
5	32	5.4	Pad Lift
	33	3.6	Ductile
10	34	2.9	Pad Lift
20	34	2.4	Pad Lift
30	31	2.7	Pad Lift

5.6 OSP-Coated Specimens

For the OSP-coated specimens, the intermetallic compounds that formed after reflow and thermal aging exhibited scallop-like morphology. Cu and Sn peaks were found in the energy dispersive spectrum, from which it was concluded that the intermetallic compounds had Cu-Sn composition. Only pad lift failure mode was found after ball shear. The results are discussed in this Section.

5.6.1 Intermetallic Compound Formation

The SEM micrographs of the interfacial microstructures found in the OSP-coated specimens after reflow are shown in Figure 49. Intermetallic compounds, with a scallop-like morphology were found at the solder ball/Cu pad interface. Upon analysis with EDS, the composition of these intermetallic compounds was determined to be Cu_6Sn_5, as shown in Figure 50. Needle-like microstructures, which are thought to be the Ag_3Sn IMC also formed at the bulk solder.

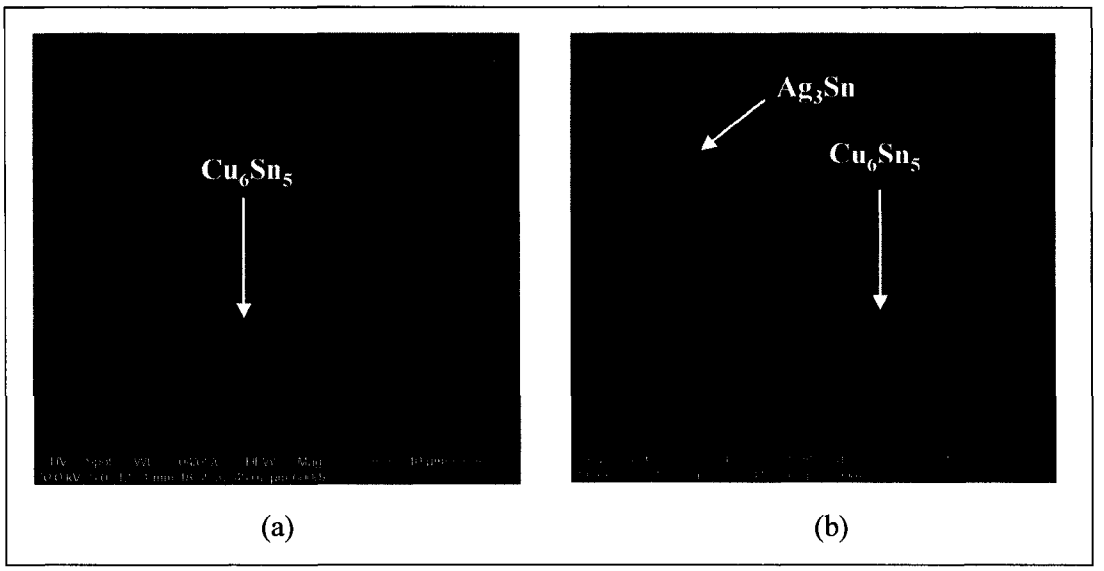

Figure 49. Interfacial microstructures of the OSP-coated specimens after reflow for (a) solder ball from Specimen 1 and (b) solder ball from Specimen 2.

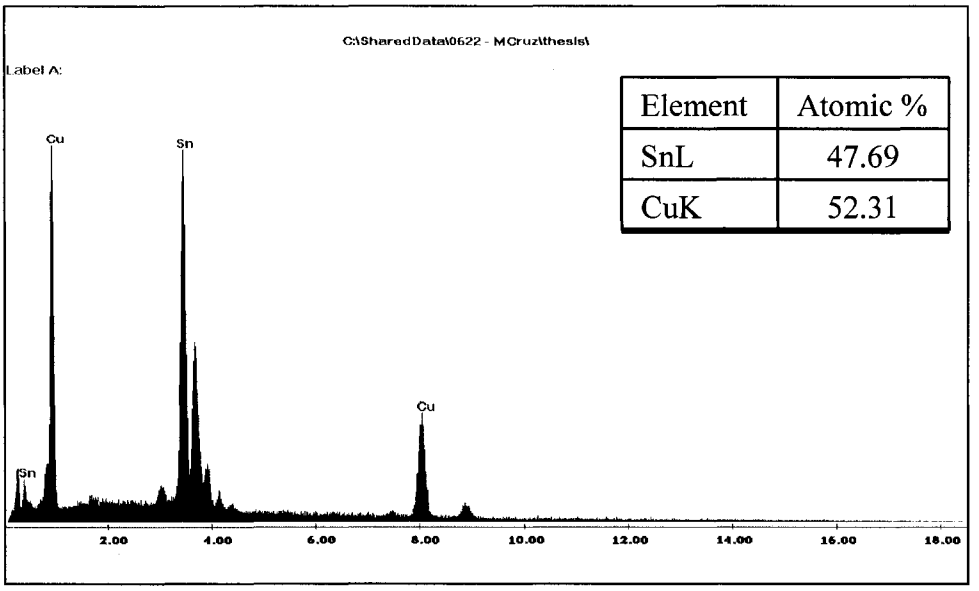

Element	Atomic %
SnL	47.69
CuK	52.31

Figure 50. EDS spectrum of the Cu_6Sn_5 intermetallic compound for the OSP-coated specimen after reflow.

The interfacial reactions after the OSP-coated specimens were aged for 5 days at 150°C are shown in 51. The thickness of these IMCs increased after aging. The Cu_6Sn_5,

with the EDS spectrum shown in Figure 52, changed its morphology from scallop-like to layered-type. Some of the needle-like Ag_3Sn intermetallic compounds also transformed to pebble-shaped and spherical-shaped microstructures. Voiding was also seen, mostly at the interface between Cu and the Cu_6Sn_5 intermetallic compound layer.

These Cu_6Sn_5 intermetallic compounds, with the EDS spectrum shown in Figure 54, became thicker as the specimens were aged for 10 days. The Ag_3Sn intermetallic compounds continued to transform to spherical-shaped, and some were embedded in the Cu_6Sn_5 IMCs. Spalling of the Cu_6Sn_5 intermetallic compound was also seen, as shown in Figure 53a. More voiding at the Cu pad/Cu_6Sn_5 intermetallic compound interface was also found.

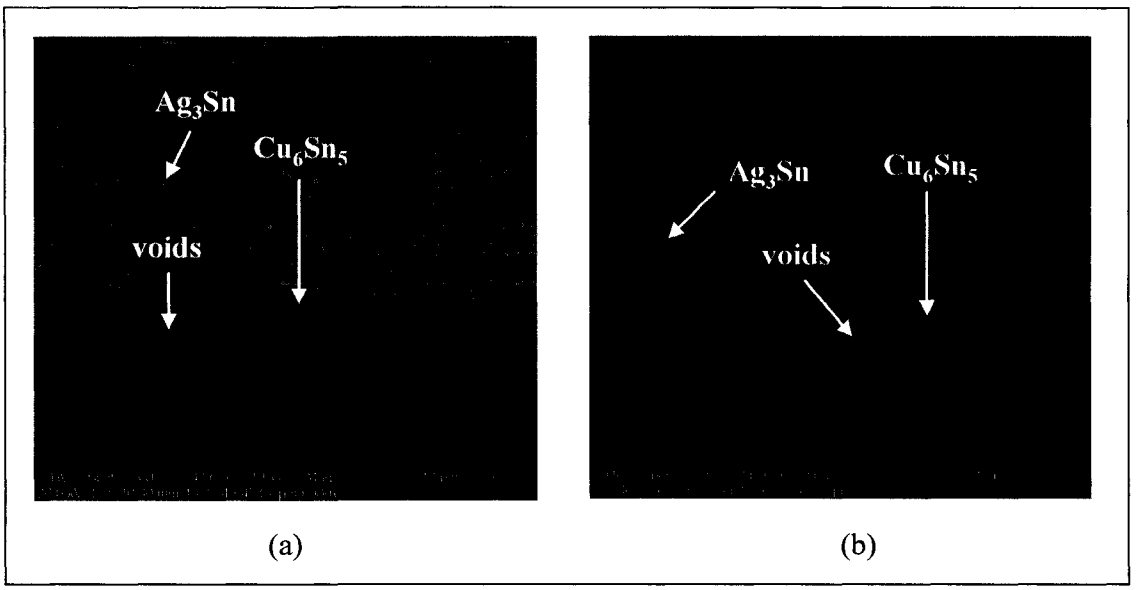

Figure 51. Interfacial microstructures of the OSP-coated specimens after aging for 5 days at 150°C, after reflow, for (a) solder ball from Specimen 1 and (b) solder ball from Specimen 2.

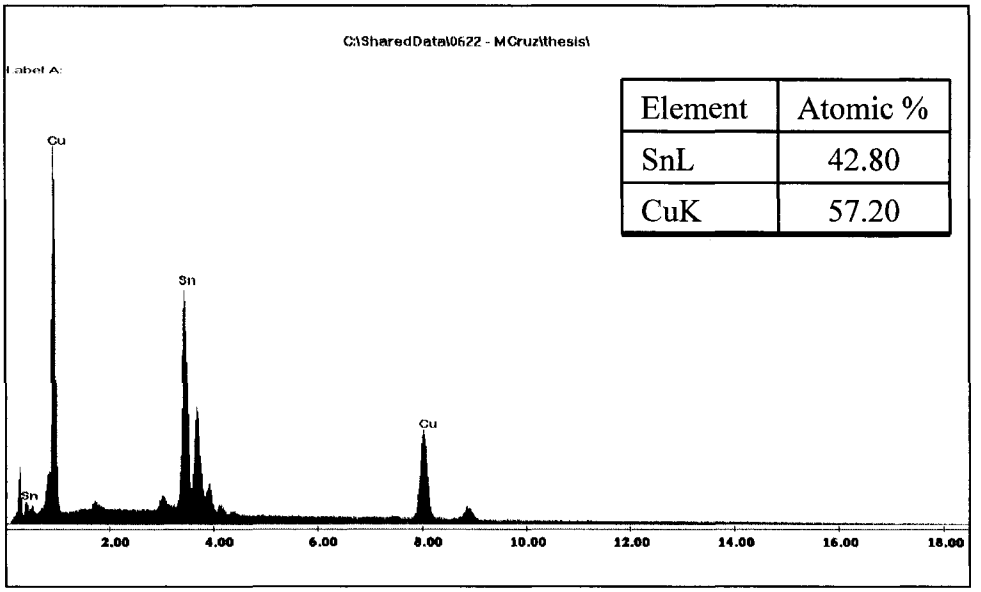

Element	Atomic %
SnL	42.80
CuK	57.20

Figure 52. EDS spectrum of the Cu_6Sn_5 intermetallic compound for the OSP-coated specimen after aging for 5 days at 150°C, after reflow.

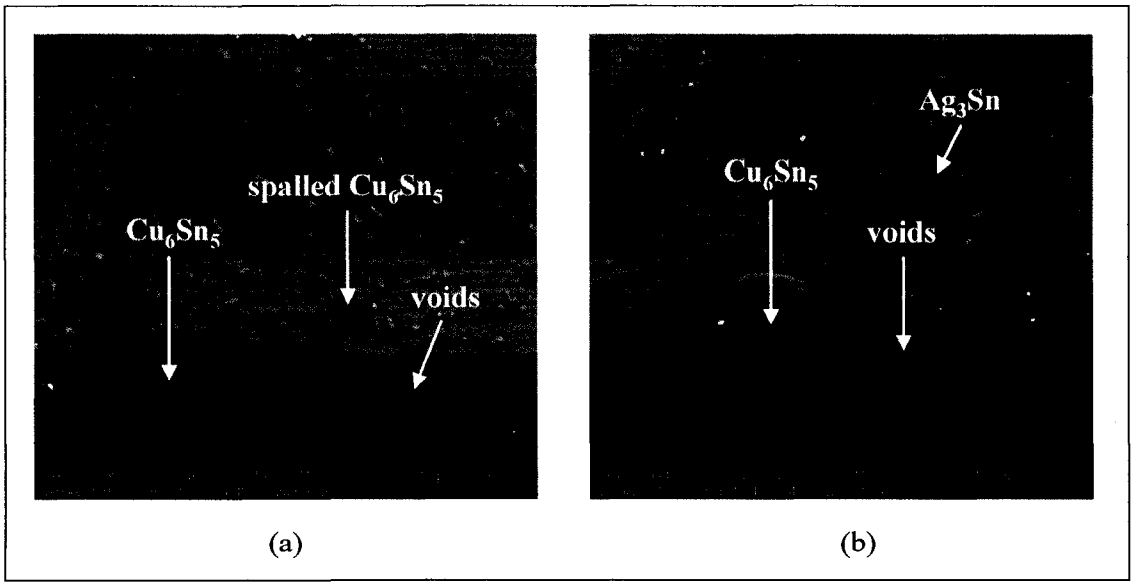

Figure 53. Interfacial microstructures of the OSP-coated specimens after aging for 10 days at 150°C, after reflow, for (a) solder ball from Specimen 1 and (b) solder ball from Specimen 2.

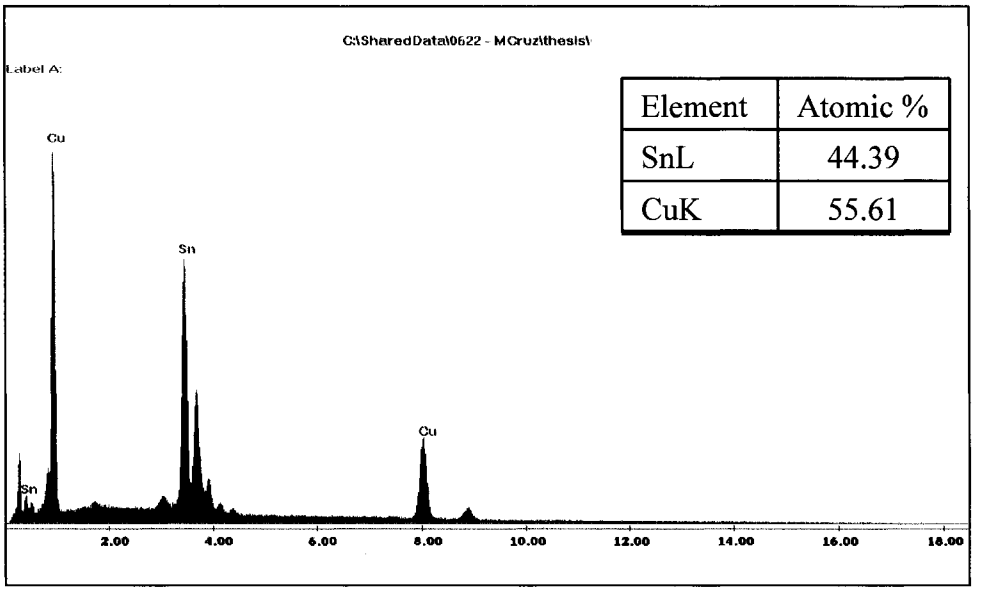

Element	Atomic %
SnL	44.39
CuK	55.61

Figure 54. EDS spectrum of the Cu_6Sn_5 intermetallic compound for the OSP-coated specimen after aging for 10 days at 150°C, after reflow.

After aging for 20 days, these Cu_6Sn_5 intermetallic compounds became even thicker, and the layered-type morphology became more obvious. Spalling was still evident as seen in Figure 55b, and even the thickness of these spalled IMCs became thicker as can be seen in Figure 55b. The Ag_3Sn intermetallic compounds continued to transform from pebble-shaped to spherical shape, and a few have already become spherical in shape. The number of voids at the interface between the Cu pad and the Cu_6Sn_5 layer increased with increased aging time. It is also interesting to note that at this aging time, another layer was detected at the interface between the Cu_6Sn_5 layer and the Cu substrate. It is at this layer where most of the voids were found. Analysis with EDS revealed that the composition of these intermetallic compounds corresponds to Cu_3Sn, as shown in Figure 56. The aging time at which these IMCs were detected and their composition is the same as those found in the ImAg-coated specimens, which is Cu_3Sn.

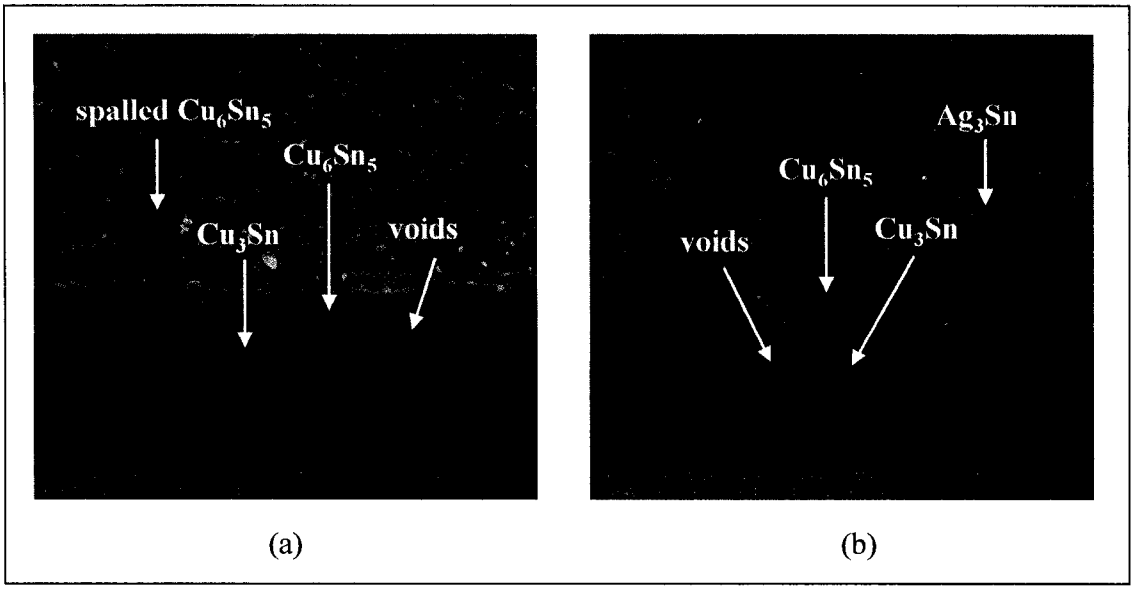

Figure 55. Interfacial microstructures of the OSP-coated specimens after aging for 20 days at 150°C, after reflow, for (a) solder ball from Specimen 1 and (b) solder ball from Specimen 2.

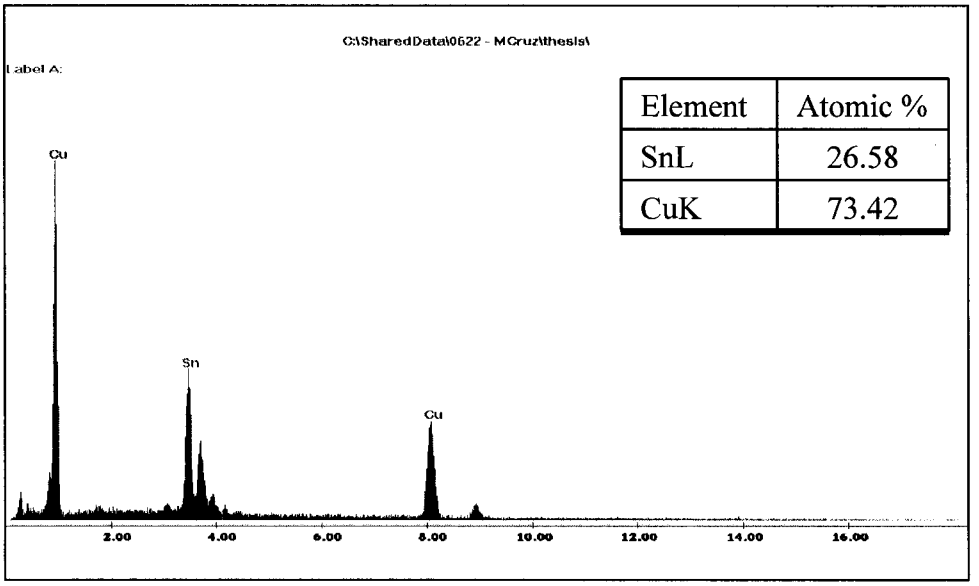

Element	Atomic %
SnL	26.58
CuK	73.42

Figure 56. EDS spectrum of the Cu_3Sn intermetallic compound for the OSP-coated specimen after aging for 20 days at 150°C.

The Cu_6Sn_5 intermetallic compounds grew thicker as the specimens were aged for 30 days. The number and the size of the voids also increased with increasing aging time. Spalling was still present as seen in Figure 57b, and the distance of the spalled IMCs from the substrate increased gradually. Almost all of the Ag_3Sn intermetallic compounds at the solder matrix transformed to spherical-shaped, and a few to pebble-shaped microstructures. No needle-like Ag_3Sn IMCs were found at this aging time. The size of these Ag_3Sn IMCs also increased, and some were still attached/embedded in the Cu_6Sn_5 intermetallic compounds. However, the number of these Ag_3Sn phases seems to have been reduced. The Cu_3Sn layer was still present and its spectrum is shown in Figure 58. It is not known, however, if its thickness had increased with increased aging time, due to SEM resolution limitations.

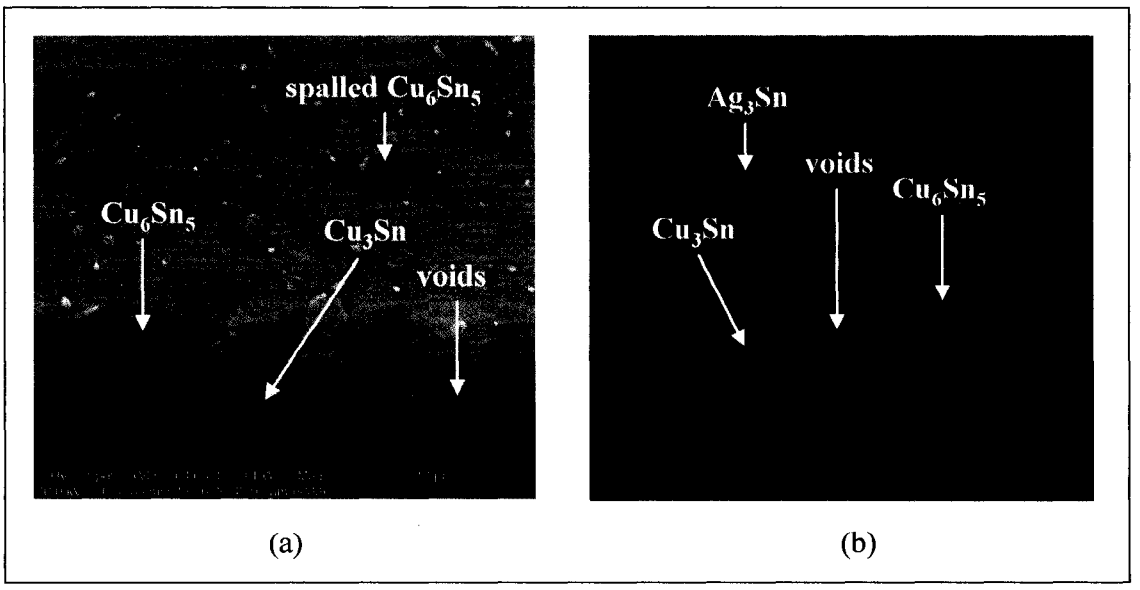

Figure 57. Interfacial microstructures of the OSP-coated specimens after aging for 30 days at 150°C, after reflow, for (a) solder ball from Specimen 1 and (b) solder ball from Specimen 2.

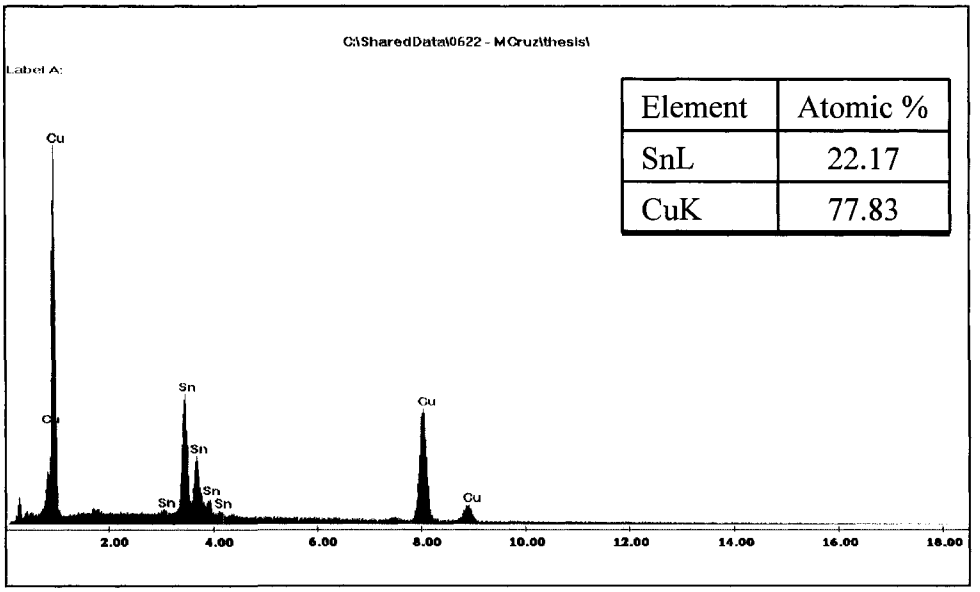

Figure 58. EDS spectrum of the Cu_3Sn intermetallic compound for the OSP-coated specimen after aging for 30 days at 150°C.

The thicknesses of the 10 largest, t_{max}, and 10 smallest, t_{min}, IMC were measured to determine the effect of aging on the IMC thickness. The averages of these measurements are shown in Table 19. The raw data are given in Appendix C.

Table 19. Average IMC thickness for the OSP-coated specimens.

Aging Time (days)	Average of t_{max} (μm)	Average of t_{min} (μm)
0	4.6	3.5
5	6.0	4.9
10	7.6	5.8
20	8.7	7.4
30	9.8	8.0

The plot of the total IMC thickness, the averages of t_{max} and t_{min}, as a function of aging time is shown in Figure 59. It can be seen that the thickness of the intermetallic compounds increased as the aging time was increased.

To determine the growth relationship between the IMC thickness and the aging time, the average of t_{max} was plotted as a function of the square root of aging time, as shown in Figure 60. This graphs exhibits a linear trend, which means that the relationship between the intermetallic compound growth and aging time is parabolic. The slope from the graph gives the growth rate constant of the intermetallic compounds. The growth rate constant obtained for the OSP-coated specimens is 3.3×10^{-3} μm/(sec)$^{1/2}$.

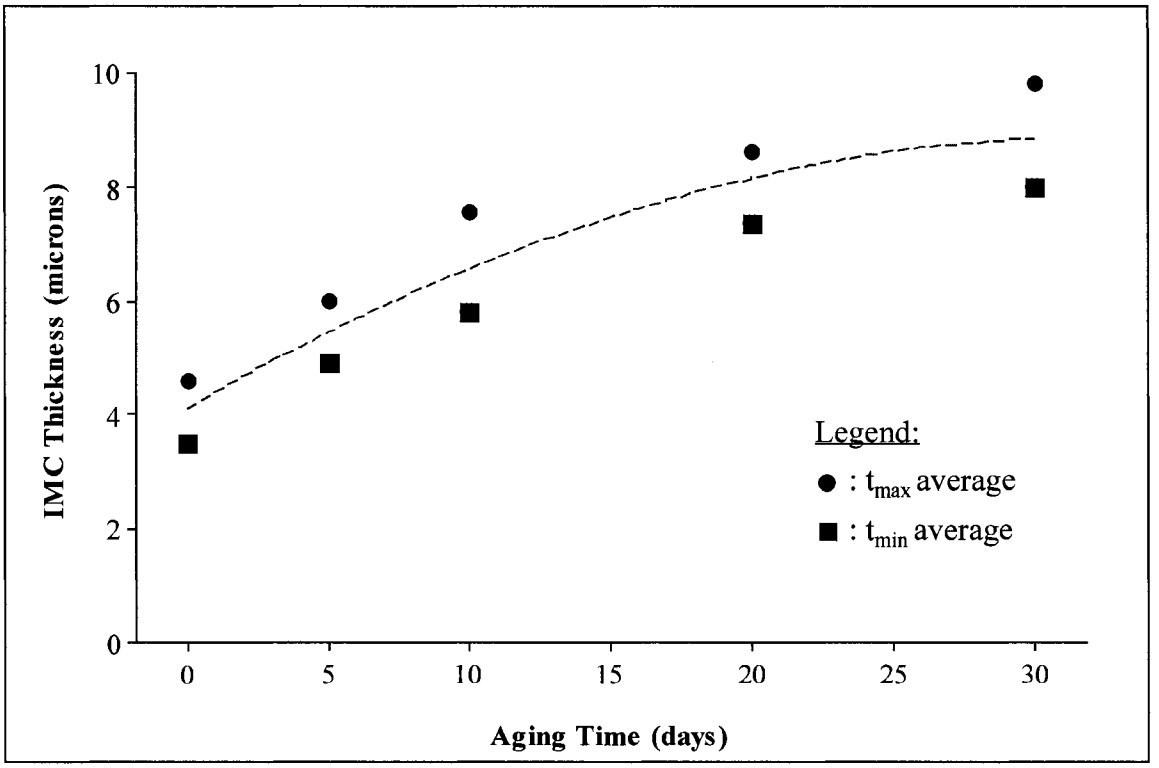

Figure 59. IMC thickness as a function of aging time plot for the OSP-coated specimens.

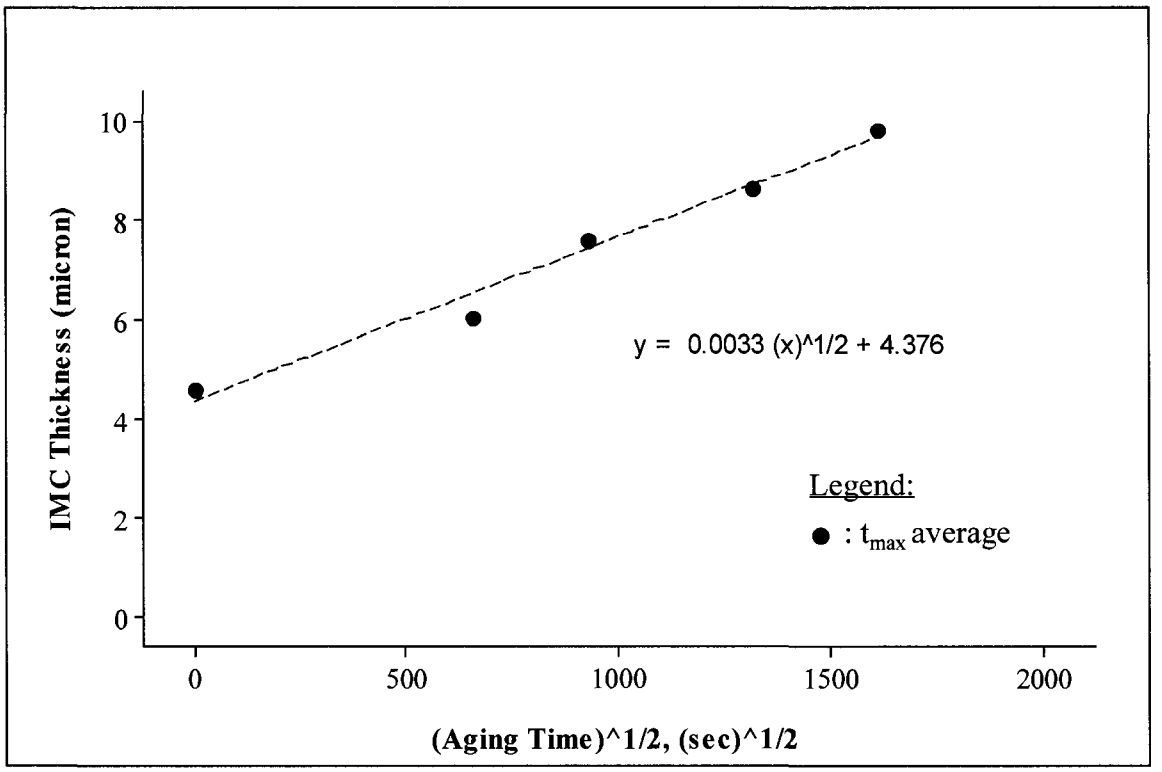

Figure 60. IMC thickness as a function of the sqrt of aging time plot for the OSP-coated specimens.

5.6.2 Shear Strength

The shear strength data for the OSP-coated specimens are shown in Table 20. The results for the student t-test and the raw data for ball shear are in Appendix C. Only one failure mode was found for these specimens, namely, pad lift.

Table 20. Average and standard deviation of ball shear data for OSP-coated specimens.

Coating Type	Aging Time (days)	Average Shear Strength (MPa)	Standard Deviation (MPa)
OSP	0	33	3
	5	36	3
	10	33	2
	20	32	2
	30	32	2

The shear strength of the OSP-coated specimens increased after 5-day aging, as shown in Figure 61. The mean shear strength then decreased asymptotically from 10 to 30-day aging. This observation agreed very well with the student t-test calculations. There was a statistical difference in shear strength between after reflow and 5-day aging, and between 5-day aging and 10-day aging. The shear strength remained constant after that. The majority of the ball shear failure mode was pad lift, indicating that the joint was consistently stronger than the pad-substrate bonding. Therefore, the solder joint strength was not affected by the thermal aging.

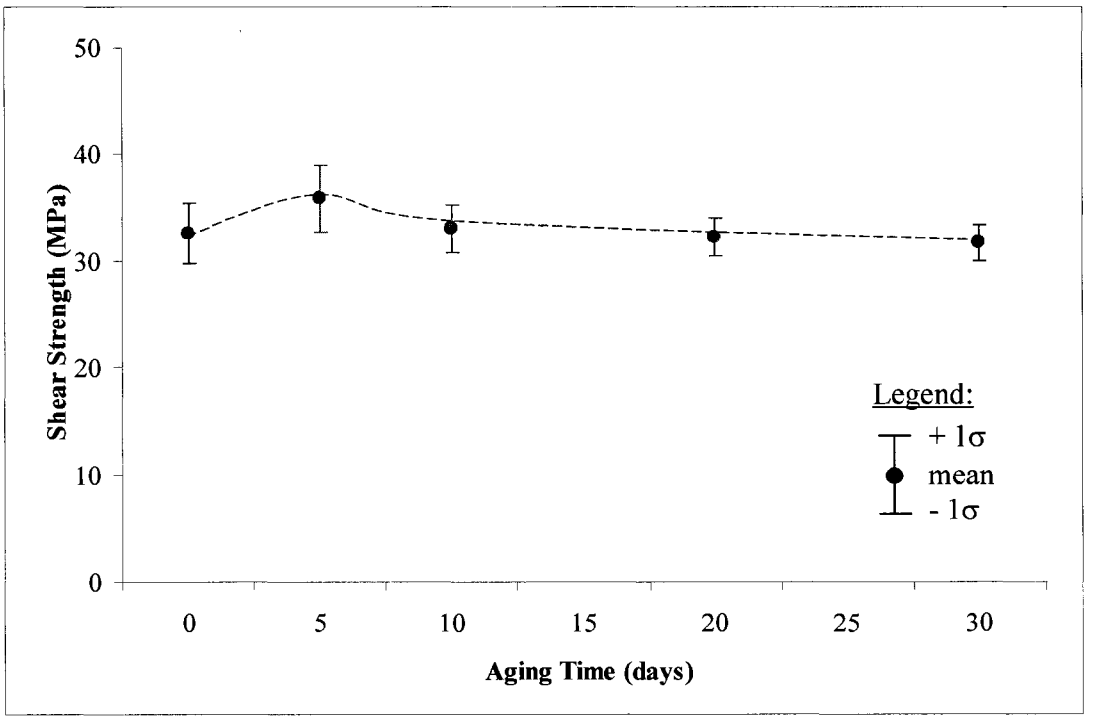

Figure 61. Ball shear test results for the OSP-coated specimens.

5.7 Comparison of the Results

The results that were obtained for the specimens coated with ImAg, ENIG, and OSP are compared and discussed in this Section.

The intermetallic compounds that formed between the solder-Cu pad interface after reflow and subsequent aging are discussed in Section 5.7.1. The shear strengths of these specimens are then compared in Section 5.7.2. The overall findings are shown in Table 21.

Table 21. IMCs and shear strength behavior found in the ImAg, ENIG, and OSP-coated specimens.

Specimen	IMC Formed	Shear Strength Behavior
ImAg	Cu_6Sn_5 and Cu_3Sn	linear, no change in shear strength
ENIG	$(Cu,Ni)_6Sn_5$ and $(Cu, Ni)_3Sn$	linear, 15% decrease over aging time
OSP	Cu_6Sn_5 and Cu_3Sn	asymptotic decrease

5.7.1 Intermetallic Compound Formation

Both ImAg and OSP-coated specimens had intermetallic compounds at the solder-Cu pad interface that were scallop-like, after reflow. These intermetallic compounds became thicker as subsequent thermal aging at 150°C was performed, after reflow. The composition of these intermetallic compounds was verified from the respective EDS spectra, and it was concluded that the IMCs were Cu_6Sn_5, which is consistent with the IMCs found in the phase diagram of the Cu-Sn binary system. Aside from Cu_6Sn_5, another IMC layer was found between the Cu_6Sn_5 layer and the Cu pad, and it was concluded from the EDS spectra that it was Cu_3Sn. This IMC was detected for both the ImAg and OSP-coated specimens after aging for 20 days.

For the ENIG-coated specimens, scallop-like intermetallic compounds were also found at the solder- pad interface after reflow. From the EDS spectra, Cu, Sn, and small Ni peaks were found and it was concluded that the IMC composition is $(Cu,Ni)_6Sn_5$. Unlike the Cu_6Sn_5 intermetallic compounds found in the ImAg and OSP-coated specimens, the IMCs found in these specimens after reflow, were scallop-like but irregular in shape. The $(Cu,Ni)_6Sn_5$ IMCs grew thicker with increasing aging time. The Ni layer between the solder and the Cu pad became thinner and seemed to have "disappeared" as aging time was increased, but it was still detected in the EDS spectra due to its interaction with Cu and Sn, forming the Cu-Ni-Sn intermetallic compound. Another IMC, the $(Cu,Ni)_3Sn$, was detected after the specimens were aged for 20 days.

The thicknesses of these intermetallic compounds were measured and overall, the thickness of the IMCs in the ImAg-coated specimens is approximately the same as those found in the OSP-coated specimens. The overall thickness of the IMCs found in the ENIG-coated specimens is about 1 μm to 1.5 μm smaller than those in the ImAg and OSP-coated specimens.

Both the ImAg and OSP-coated specimens exhibited parabolic growth when the IMC thicknesses were plotted as a function of the square root of aging time. The slopes obtained from these graphs correspond to the growth rate constant of the intermetallic compounds at 150°C. The values obtained for the ImAg and OSP-coated specimens were 3.15×10^{-3} μm/(sec)$^{1/2}$ and 3.3×10^{-3} μm/(sec)$^{1/2}$, respectively. The ENIG-coated specimens did not exhibit parabolic growth behavior.

5.7.2 Shear Strength

Two types of failure mode were found after ball shear tests: pad lift and ductile. Both ImAg and OSP-coated specimens only had pad lift failure, while the ENIG-coated specimens had both modes. For the ImAg-coated specimens, practically no change in the solder shear strength was found after aging for 30 days. The mean shear strength of the OSP-coated specimens increased after 5 days, and decreased asymptotically from 10 to 30-day aging. For the ENIG-coated specimens, the shear strength behavior was linear, with a 15% decrease in the mean shear strength after 30-day aging. Overall, the mean shear force was approximately the same for all three coating types after 30-day aging.

CHAPTER 6

DISCUSSION OF RESULTS

The interfacial reactions that formed between the SAC 305 solder and the Cu-coated specimens and the solder joint shear strength presented in Chapter 5, are discussed in this chapter. The reliability of the results is addressed in Section 6.1, Interfacial Reactions in Section 6.2, and Shear Strength in 6.3. The results obtained in this study are also compared with those from published papers.

6.1 Reliability of the Results

As noted in Chapter 4, two specimens for microstructural analysis and two specimens for ball shear test, for each aging time for each coating type, were used in this study. A total of ten solder ball cross-sections, representing five from each of the two specimens were examined for microstructural analysis. Twenty solder balls, with ten from each of the two specimens, for each aging time, for each coating type, were sheared. The consistency of the failure mode in ball shear test for the ImAg and OSP-coated specimens reveal that the trend of the results were inherent to the specimens and not from accidental sources of error. In addition, the trend found in the intermetallic compound growth, that is, increasing IMC thickness with increasing aging time, agrees very well with published data [2, 19-23]. The composition of these intermetallic compounds is also consistent with those found in the literature [17, 24-26].

6.2 Interfacial Reactions

For both the ImAg and OSP-coated Cu specimens, the scallop-like Cu_6Sn_5 intermetallic compound was the dominant interfacial compound after reflow. After solid-state aging, this intermetallic compound transformed from a scallop-like to a layered-type morphology. This finding is similar to Tu's research [9] and other research studies [23, 68-69]. The formation of Cu_6Sn_5 may be attributed to the dissolution of Cu from the substrate into the molten solder. Kim and Tu suggested that a nonconservative ripening process contributes to the formation of a scallop-like structure and results in the growth and coarsening of the Cu_6Sn_5 intermetallic compound [69]. This scallop-like morphology is often found after reflow, and subsequent annealing or aging transforms this scallop-like structure into a planar-type morphology as a result of simultaneous intermetallic dissolution and growth [68]. With the Cu_6Sn_5 intermetallic compound between the solder and the Cu substrate, it would be difficult for Cu to dissolve into Sn due to the presence of the Cu_6Sn_5 structure, which serves as a "diffusion barrier" between Cu and Sn. Cu_3Sn will form when Cu_6Sn_5 is in contact with Cu and there is a supply of Cu.

During reflow, when the Sn-Ag-Cu solder ball is in contact with the Cu pad, the Cu surface sees liquid Sn. Therefore, the first intermetallic compound that forms is Sn-rich, i.e., Cu_6Sn_5. Cu_6Sn_5 forms first because the interface is Sn-rich, with Sn being in the liquid state and Cu is available only from the dissolution process, which limits the supply of Cu. Once this thin layer of Cu_6Sn_5 is formed between the solder ball and the Cu pad, Cu migrates through Cu_6Sn_5 to form more Cu_6Sn_5 on the surface. However, Cu migration through the Cu_6Sn_5 layer is solid-state diffusion controlled, hence, a parabolic

growth behavior is seen. Cu then begins to react with the Cu_6Sn_5 as aging is performed, and this is possible because a compound with a lower enthalpy of formation, $\Delta H°_f$, and is more stable than Cu_6Sn_5 can exist, i.e., Cu_3Sn, where $\Delta H°_f$ for this intermetallic compound is -7.75 kJ/g atom [70]. The reaction for formation of Cu_3Sn can be represented as:

$$Cu_6Sn_5 + 9\ Cu \rightarrow 5\ Cu_3Sn$$

Another argument substantiating this can be inferred from the Cu-Sn binary phase diagram. The Sn-rich intermetallic compound, Cu_6Sn_5 has a lower melting point than the Cu-rich intermetallic compound, Cu_3Sn. This means that the $\Delta H°_f$ of Cu_6Sn_5 is higher than the $\Delta H°_f$ of Cu_3Sn, indicating that Cu_6Sn_5 will form first before Cu_3Sn.

Voids, found mostly at the interface between the Cu substrate and the Cu_6Sn_5 intermetallic compound layer, may be attributed to the difference in the diffusion rates of the different elements. If one element diffuses faster than the other element, then vacancies are formed in the region from which diffusion is faster. These vacancies then accumulate to form voids and are known as Kirkendall voids. A group of researchers reported that the growth of the Cu_3Sn intermetallic compound is responsible for the Kirkendall voids formed during solid-state aging, and that reducing its thickness or slowing its growth can subsequently reduce the formation of voids [10]. Although this finding cannot be verified in this study, it was seen, however, that voids were larger when the Cu_3Sn intermetallic compound was detected.

Most researchers have found that the intermetallic compound that formed between Sn-Pb and Sn-Ag solders and Ni is Ni_3Sn_4. In this study, however, the intermetallic

compound that formed between Sn-Ag-Cu and Ni (for the ENIG-coated specimens) after reflow was $(Cu,Ni)_6Sn_5$. This finding is consistent with Zeng *et al.*'s [71] and Zhang *et al.*'s [72] researches, in that $(Cu,Ni)_6Sn_5$ was found instead of the expected Ni_3Sn_4. Zeng and his colleagues stated that the presence of Cu in the Sn-Ag-Cu solder suppressed the formation of Ni_3Sn_4, and promoted the formation of $(Cu,Ni)_6Sn_5$ intermetallic compounds at the Sn-Ag-Cu/Ni interface instead. From the Cu-Sn binary phase diagram, Cu_6Sn_5 is expected to form when Cu and Sn are reacted with each other under Sn-rich conditions. In the presence of Ni, the $(Cu,Ni)_6Sn_5$ intermetallic compound is formed instead due to the diffusion of Ni into Cu. In Chapter 2, it was seen from the Cu-Ni phase diagram that Cu and Ni form a set of isomorphous solid solutions since these two elements are completely soluble in each other in both the solid and liquid states. As a result, the Ni atoms can substitute for the Cu atoms without distorting the lattice, and hence, $(Cu,Ni)_6Sn_5$ intermetallic compounds are formed. This continues to occur until the supply of Ni is depleted. As seen in this study, although Ni was detected in the $(Cu,Ni)_6Sn_5$ intermetallic compound, the Ni content continued to diminish as aging time was increased.

Spalling was more apparent when there was little or no Ni left in the ENIG-coated specimens. This same finding was seen by other researches [6, 17]. The absence of the Ni barrier allowed the Cu_6Sn_5 intermetallic compound to migrate away from the interfacial layer and move toward the solder side. As aging time was increased, the size of these spalled Cu_6Sn_5 intermetallic compounds became larger due to the ripening process mentioned earlier.

Ag in the solder did not participate in the interfacial reactions with the substrate; instead, it formed intermetallic compounds with Sn, Ag_3Sn, in the solder matrix. The transformation of the Ag_3Sn intermetallic compound morphology from needle-like to pebble-shaped to spherical is driven by the reduction in surface free energy. Since Ag_3Sn is a precipitation by-product of Ag and Sn, its formation in the bulk solder matrix, and not at the solder-pad interface is expected.

Both the ImAg and OSP-coated specimens exhibited parabolic growth behavior, that is, a linear trend was found when the IMC thickness was plotted as a function of the square root of aging time. The slopes from these graphs correspond to the growth rate constants of the intermetallic compounds at the aging temperature of 150°C. The values obtained were very close to each other, 3.152×10^{-3} μm/(sec)$^{1/2}$ for the ImAg-coated specimens and 3.3×10^{-3} μm/(sec)$^{1/2}$ for the OSP-coated specimens. These growth rate constants compared very well with those obtained by other researches [21-22] as shown in Table 22. In fact, the growth rate constant found for the OSP-coated specimens in this study was practically the same as that found by Chuang *et al.* [22]. The difference in the growth constants found in this study and that of Yoon and Jung [21] may be due to the higher reflow temperature that was used in their study, ~ 255°C-261°C, as compared to 240°C in this research. From Equation 4, it can be deduced that the growth rate constant, k, would be higher if reflow was done at a higher temperature. As a consequence, the intermetallic compounds that form after reflow at a higher temperature would be larger than those that formed at a lower reflow temperature. Subsequent aging would change the morphology from scallop-like to planar-type, but the overall growth of the

intermetallic compounds that were reflowed at a higher temperature would still be faster than those reflowed at a lower temperature since the intermetallic compounds in the former case were already larger after reflow. This explains why the growth rate constant obtained by Yoon and Jung was higher than the growth rates obtained in this study, even though the aging temperature was the same for both studies.

$$k = A\exp\left(\frac{-Q}{RT}\right) \qquad \text{Equation 4}$$

where: A is a constant

T is the absolute temperature

R is the universal gas constant

Q is the activation energy required for the reaction

The intermetallic compounds found in the ENIG-coated specimens did not exhibit parabolic growth; a quadratic function was found to provide the best fit to the data.

Table 22. Growth rate constants of Sn-Ag-Cu solders/Cu specimens at the aging temperature of 150°C.

Solder Composition / Substrate Metallization	Growth Rate Constant (μm/sec)	Reference
96.5Sn-3.0Ag-05Cu/Cu (ImAg)	3.15×10^{-3}	This work
96.5Sn-3.0Ag-05Cu/Cu (OSP)	3.3×10^{-3}	This work
95.75Sn-3.5Ag-0.75Cu/Cu	5.1×10^{-3}	[21]
95.8Sn-3.5Ag-0.7Cu/Cu	3.3×10^{-3}	[22]

6.3 Shear Strength

Only one type of failure mode was seen for the ImAg and OSP-coated specimens after the solder balls were sheared, namely pad lift. For the ENIG-coated specimens, both pad lift and ductile failure modes were found.

Since there was no change in the shear strength of the ImAg-coated specimens regardless of aging time, then there was no degradation in the solder joint strength. Compared to the ENIG-coated specimens, the mean shear strength of the ImAg-coated specimens after reflow was 5 MPa lower than that of the ENIG-coated specimens, and the overall shear strengths were the same after 30-day aging. The ball shear test results for the ENIG-coated specimens exhibited a linear behavior, with a 15% decrease in the mean shear strength after 30-day aging. In contrast, the shear strength behavior of the OSP-coated specimens was different from those of the specimens with ImAg and ENIG coatings. For the OSP-coated specimens, the mean shear strength increased after 5-day aging, then decreased asymptotically from 10-day to 30-day aging. However, the mean shear strength of these specimens after reflow and 30-day aging was approximately the same as that of the ImAg-coated specimens. Among the three coatings, the OSP-coated specimens were the only ones that had an increase in shear strength after 5-day aging.

Pad lift is an adhesion or bonding strength issue between the Cu pad and the printed circuit board substrate. When a sheared solder ball exhibits this failure mode, it means that the adhesion strength between the solder ball and the Cu pad is stronger than the adhesion strength between the Cu pad and the substrate. The ductile failure mode is a solder strength issue. It denotes the strength of the solder ball, not of the solder joint.

Both pad lift and ductile failure modes do not represent the "interfacial strength". However, when these failure modes are obtained instead of intermetallic layer breakage, then it indicates that the adhesion strength between the pad and the substrate or the strength of the bulk solder ball is weaker than the strength of the interface or in this case, the intermetallic layer. It has been reported repeatedly that intermetallic compounds are brittle in nature and that these brittle IMCs is where the failure of the solder joint occurs [2, 26-27, 56]. However, no failure in the intermetallic compound layer was found in this research.

The difference between the trend in the graphs and student t-test calculations, with a confidence level of 95%, may be attributed to the failure modes found after ball shear. For the ENIG-coated specimens, in addition to failure mode, the presence of voids and the ripening of the Ag_3Sn intermetallic compounds, both of which were not accounted for in the student t-test calculations, may also account for the difference between the graph trends and the t-test calculations. The reduction in shear strength with increasing aging times may be attributed to the coarsening of the Ag_3Sn intermetallic compounds. Initially, these IMCs were smaller in size, hence, the greater the strength of the material. As the specimens were aged, these Ag_3Sn IMCs continued to grow bigger, making the material weaker, hence, lower shear strength.

CHAPTER 7

CONCLUSIONS

The interfacial reactions that formed between the Sn-3.0Ag-0.5Cu wt % solder and the Cu-coated PCB pads after reflow and isothermal aging and their effects on the shear strength of the solder joints were studied. Several conclusions can be drawn from this research.

- Cu_6Sn_5 formed first, followed by Cu_3Sn. This finding was also true for $(Cu,Ni)_6Sn_5$ and $(Cu,Ni)_3Sn$.
- The thickness of the intermetallic compounds, both Cu_6Sn_5 and $(Cu,Ni)_6Sn_5$, increased with increasing aging time. The morphology of the IMCs for the ImAg and OSP-coated specimens were the same and had approximately the same overall thickness. After 30-day aging, the Cu-Sn intermetallic compounds of the ImAg and OSP-coated specimens were approximately 1 μm thicker than the Cu-Ni-Sn IMCs found in the ENIG-coated specimens.
- The IMCs that formed between the solder and the ImAg and OSP-coated Cu pad specimens exhibited parabolic growth behavior, while those from the ENIG-coated specimens showed quadratic growth.
- The electroless Ni barrier was not effective in inhibiting the Cu pad from forming an intermetallic compound with the Sn in the solder ball. As a result, $(Cu,Ni)_6Sn_5$ intermetallic compounds were found at the solder ball-pad interface in the ENIG-coated specimens.

- Voids were found for the ImAg and OSP-coated specimens after 5-day aging, and after reflow for the ENIG-coated specimens. The number and size of voids increased with increasing aging time, and the voids from the ENIG-coated specimens were the largest. Void formation maybe attributed to the difference in the diffusion rates of the elements.
- Ag did not participate in the interfacial reactions; instead needle-like Ag_3Sn intermetallic compounds were found in the bulk solder after reflow. These needle-like intermetallic compounds transformed to pebble-shaped and finally to spherical-shaped morphology as aging time was increased. This is driven by the reduction in surface free energy.
- The failure modes found for ball shear test were pad lift and ductile failure. Since these failure modes, and not intermetallic compound breakage, were found, it showed that the adhesion strength between the pad and the substrate, and the strength of the solder itself were weaker than the strength of the interface.

CHAPTER 8

RECOMMENDATIONS FOR FUTURE WORK

In order to completely and correctly analyze the composition of the intermetallic compounds, the crystallography of these compounds must be determined using X-ray diffraction techniques to confirm the EDS data obtained in this research. In addition, extensive aging studies at different aging temperatures are recommended to determine the activation energy for growth of the intermetallic compounds.

It is also recommended that the materials be procured from different suppliers, and the results be compared to obtain a "global" finding.

REFERENCES

1. C.W. Huang and K.L. Lin, "*Interfacial reactions of lead-free Sn-Zn based solders on Cu and Cu-plated electroless Ni-P/Au layer under aging at 150°C*," J. Mater. Res., **19** (**12**), 3560-3568 (2004).

2. A. Hirose, H. Yanagawa, E. Ide and K. Kobayashi, "*Joint strength and interfacial microstructure between Sn-Ag-Cu and Sn-Zn-Bi solders and Cu substrate*," Sci. & Tech. of Adv. Mater., **5** (**1-2**), 267-276 (2004).

3. S.K. Kang, D.Y. Shih, K. Fogel, P.Lauro, M.J.Yim, G.G. Advocate, M. Griffin, C. Goldsmith, D.W. Henderson, T.A. Gosselin, D.E. King, J.J. Konrad, A. Sarkhel and K.J. Puttlitz, "*Interfacial reaction studies on lead-free solder alloys*," IEEE Trans. on Electron. Pack. Manufac., **25** (**3**), 155-161 (2002).

4. C.M.L. Wu, D.Q. Yu, C.M.T. Law and L. Wang, "*Properties of lead-free solder alloys with rare earth element additions*," Mater. Sci. & Eng. R, **44**, 1-44 (2004).

5. M.N. Islam, Y.C. Chan, M.J. Rizvi and W. Jillek, "*Investigations of interfacial reactions of Sn-Zn based and Sn-Ag-Cu lead-free solder alloys as replacement for Sn-Pb solder*," J. Alloys & Comp., **400**, 136-144 (2005).

6. A. Sharif and Y.C. Chan, "*Interfacial reactions of Sn-3.5%Ag and Sn-3.5%Ag-0.5%Cu solder with electroless Ni/Au metallization during multiple reflow cycles*," J. Mater. Sci.: Mater. in Electron., **16**, 153-158 (2005).

7. J.Y. Park, C.W. Yang, J.S. Ha, C.U. Kim, E.J. Kwon, S.B. Jung and C.S. Kang, "*Investigation of interfacial reaction between Sn-Ag eutectic solder and Au/Ni/Cu/Ti thin film metallization*," J. Electron. Mater., **30** (**9**), 1165-1170 (2001).

8. G.Y.Li, B.L. Chen and J.N. Tey, "*Reaction of Sn-3.5Ag-0.7Cu-xSb solder with Cu metallization during reflow soldering*," IEEE Trans. on Electron. Pack. Manufac., **27** (**1**), 77-85 (2004).

9. K.N. Tu, A.M. Gusak and M. Li, "*Physics and materials challenges for lead-free solders*," J. App. Phys., **93** (**3**), 1335-1353 (2003).

10. S.K. Kang, P.A. Lauro, D.Y. Shih, D.W. Henderson and K.J. Puttlitz, "*Microstructure and mechanical properties of lead-free solders and solder joints used in microelectronic applications*," IBM J. Res. & Dev., **49** (**4-5**), 607-620 (2005).

11. C.W. Hwang and K.Suganuma, "*Effect of Cu addition to Sn-Ag lead-free solder on interfacial stability with Fe-42Ni*," Mater. Trans., **45** (**3**), 714-720 (2004).

12. Y. Takaku, X.J. Liu, I. Ohnuma, R. Kainuma and K. Ishida, "*Interfacial reaction and morphology between molten Sn base solders and Cu substrate*," Mater. Trans., **45** (**3**), 646-651 (2004).

13. T. Laurila, V.Vuorinen and J.K. Kivilahti, "*Interfacial reactions between lead-free solders and common base metals*," Mater. Sci. & Eng. R, **49**, 1-60 (2005).

14. M. Abtew and G. Selvaduray, "*Lead-free solders in microelectronics,*" Mater. Sci. Eng. R., **27** (**5-6**), 95-141 (2000).

15. D.Q. Yu, C.M.L. Wu, C.M.T. Law, L. Wang and J.K.L. Lai, "*Intermetallic compound growth between Sn-3.5Ag lead-free solder and Cu substrate by dipping method*," J. Alloys & Comp., **392** (**1-2**), 192-199 (2005).

16. National Center for Manufacturing Sciences (2007). *Lead-free Solders* [Online]. Available at http://www.ncms.org (accessed 10 June 2007).

17. M.N. Islam and Y.C. Chan, "*Interfacial reactions of Cu-containing lead-free solders with Au/NiP Metallization,*" J. Electron. Mater., **34** (**5**), 662-669 (2005).

18. G. Selvaduray, "*Intermetallic Compounds*," Materials Engineering 234 Lecture Slides, San Jose State University, 54 (2005).

19. M.N. Islam, A. Sharif and Y.C. Chan, "*Effect of volume in interfacial reaction between eutectic Sn-3.5%Ag-0.5%Cu solder and Cu metallization in microelectronic packaging,*" J. Electron. Mater., **34** (**2**), 143-149 (2005).

20. A. Sharif and Y.C. Chan, *"Comparative study of interfacial reactions of Sn-Ag-Cu and Sn-Ag solders on Cu pads during reflow soldering,"* J. Electron. Mater., **34 (1)**, 46-52 (2005).

21. J.W. Yoon and S.B. Jung, "*Effect of isothermal aging on intermetallic compound layer growth at the interface between Sn-3.5Ag-0.75Cu solder and Cu substrate*," J. Mater. Sci., **39**, 4211-4217 (2004).

22. C.M. Chuang and K.L. Lin, *"Effect of microelements addition on the interfacial reaction between Sn-Ag-Cu solders and the Cu substrate,"* J. Electron. Mater., **32 (12)**, 1426-1431 (2003).

23. K.S. Kim, S.H. Huh and K. Suganuma, "*Effects of intermetallic compounds on properties of Sn-Ag-Cu lead-free soldered joints*," J. of Alloys & Comp., **352**, 226-236, (2003).

24. D.Q. Yu, L.Wang, C.M.L. Wu and C.M.T. Law, *"The formation of nano-Ag_3Sn particles on the intermetallic compounds during wetting reaction,"* J. Alloys & Comp., **389**, 153-158 (2005).

25. C.E. Ho, R.Y. Tsai, Y.L. Lin and C.R. Kao, *"Effect of Cu concentration on the reactions between Sn-Ag-Cu solders and Ni,"* J. Electron. Mater., **31 (6)**, 584-590 (2002).

26. J. Sundelin, S. Nurmi, T. Lepisto and E. Ristolainen, *"Mechanical and microstructural properties of SnAgCu solder joints,"* Mat Sci and Eng A., **420**, 55-62 (2006).

27. A. Sharif, M.N. Islam and Y.C. Chan, "*Interfacial reactions of BGA Sn-3.5%Ag-0.5%Cu and Sn-3.5%Ag solders during high-temperature aging with Ni/Au metallization,"* Mat. Sci & Eng. B, **113**, 184-189 (2004).

28. V. Vourinen, T. Laurila, H. Yu and J.K. Kivilahti, *"Phase formation between lead-free Sn-Ag-Cu solder and Ni(P)/Au finishes,"* J. Appl. Phys., **99**, 0235301-023536 (2006).

29. T. Laurila, V. Vuorinen and J.K. Kivilahti, *"Analyses of interfacial reactions at different levels of interconnection,"* Procs. Mater. Sci. Semicon., 307-317 (2004).

30. J.W. Yoon, S.W. Kim, J.M. Koo, D.G. Kim and S.B. Jung, *"Reliability investigation and interfacial reaction of ball grid array packages using the lead-free Sn-Cu Solder,"* J. Electron. Mater,, **33 (10)**, 1190-1199 (2004).

31. Z. Chen, M. He and G. Qi, *"Morphology and kinetic study of the interfacial reaction between the Sn-3.5Ag solder and electroless Ni-P metallization,"* J. Electron. Mater., **33 (12)**, 1465-1472 (2004).

32. M. He, Z. Chen and G. Qi, *"Solid state interfacial reaction of Sn-37Pb and Sn-3.5Ag solders with Ni-P under bump metallization,"* Acta Mater., **52**, 2047-2056 (2004).

33. H.H. Chung, *"Effect of geometry on solder joint reliability of leadless leadframe package,"* Master's Thesis, Dept of Chem and Mat Eng, SJSU, 21-33 (2004).

34. D.V. Ragone, Thermodynamics of Materials, Vol. 1 (John Wiley and Sons, Inc., New York, USA, 1995), pp. 138.

35. T.A. Ramanarayanan and R.A Rapp, *"The diffusivity and solubility of oxygen in liquid tin and solid silver and the diffusivity of oxygen in solid nickel,"* Metall. Transac., **3 (12)**, 3239-3246 (1972).

36. B. Ozturk, P. Barron, and R.J. Fruehan, *"Physical chemistry of gas liquid solder reactions,"* Metall. Transac. B, **18 (3)**, 577-582 (1987).

37. D.A. Porter and K.E. Easterling, Phase Transformations in Metals and Alloys, 2nd ed. (CRC Press, United Kingdom, 2001), pp. 10.

38. S.W. Jeong, J.H. Kim and H.M. Lee, "*Thermodynamic issues of lead-free soldering in electronic packaging*," Mater. Sci. Forum, **426-432,** 4081-4086 (2003).

39. G. Selvaduray, "*Intermetallic Compound Formation*," Materials Engineering 234 Lecture Slides, San Jose State University, 53 (2005).

40. M. Hansen and K. Anderko, Constitution of Binary Alloys, 2nd ed. (McGraw-Hill Book Company, New York, 1958), p. 634.

41. G. Gosh and M. Asta, *"Phase stability, phase transformations, and elastic properties of Cu_6Sn_5: Ab initio calculations and experimental results,"* J. Mater. Res., **20** (**11**), 3102-3117 (2005).

42. A. Gangulee, G.C. Das, and M.B. Bever, *"An x-ray diffraction and calorimetric investigation of the compound Cu_6Sn_5,"* Metall Transac., **4** (**9**), 2063-2066 (1973).

43. J.D. Bernal, *"The complex structure of the copper-tin intermetallic compounds,"* Nature, **122**, 54 (1928).

44. M. Hansen and K. Anderko, Constitution of Binary Alloys, 2nd ed. (McGraw-Hill Book Company, New York, 1958), p. 636.

45. JCPDS- The International Center for Diffraction Data, Powder Diffraction File, (Newton Square, PA, 2002).

46. A.K Larsson, L. Stenberg, and S. Lidin, *"The superstructure of domain-twinned n'-Cu_6Sn_5,"* Acta Cryst., **B50**, 636-643 (1994).

47. S. Lidin, *"Superstructure ordering of intermetallics: B8 structures in the pseudo-cubic regime,"* Acta Cryst., **B54**, 97-108 (1998).

48. B.D. Cullity and S.R. Stock, Elements of X-Ray Diffraction, 3rd ed. (Prentice Hall, New Jersey, 2001), p. 324.

49. Y. Watanabe, Y. Fujinaga, and H. Iwasaki, *"Lattice modulation in the long period-superstructure of Cu_3Sn,"* Acta Cryst., **B39**, 306-311 (1982).

50. M. Hansen and K. Anderko, Constitution of Binary Alloys, 2nd ed. (McGraw-Hill Book Company, New York, 1958), p. 52.

51. M. Hansen and K. Anderko, Constitution of Binary Alloys, 2nd ed. (McGraw-Hill Book Company, New York, 1958), p. 602.

52. M. Hansen and K. Anderko, Constitution of Binary Alloys, 2nd ed. (McGraw-Hill Book Company, New York, 1958), p. 1043.

53. M. Hansen and K. Anderko, Constitution of Binary Alloys, 2nd ed. (McGraw-Hill Book Company, New York, 1958), p. 18.

54. M. Hansen and K. Anderko, Constitution of Binary Alloys, 2nd ed. (McGraw-Hill Book Company, New York, 1958), p. 36.

55. W.K. Choi S.Y. Jang, J.H. Kim, K.W. Paik and H.M. Lee, *"Grain morphology of intermetallic compounds at solder joints,"* J. Mater. Res., **17** (**3**), 597-599 (2002).

56. D.G. Kim, J.W. Kim and S.B. Jeung, *"Effect of aging conditions on interfacial reaction and mechanical joint strength between Sn-3.0Ag-0.5Cu solder and Ni-P UBM,"* Mater. Sci. & Eng. B, **21**, 204-210 (2005).

57. San Francisco Circuits, Purchase Order (August 2006).

58. IPC STANDARD: IPC 4552, *" Specification for Electroless Nickel/Immersion Gold (ENIG) Plating for Printed Circuit Boards,"* (2002).

59. IPC STANDARD: IPC 4553, *"Specification for Immersion Silver Plating for Printed Circuit Boards,"* (2005).

60. H. Shoemaker, Profound Material Technology Corporation, *private communication*, September 2006.

61. JEDEC STANDARD: J-STD-003, "*Solderability Tests for Printed Circuit Boards*," (2006).

62. Buehler Sum-Met, The Science Behind Materials Preparation: A Guide to Materials Preparation and Analysis: Electronic Materials, pp. 62-64 (2004).

63. JEDEC STANDARD: J-STD-020, *"Moisture/Reflow Sensitivity Classification for Non-Hermetic Solid State Surface Mount Devices,"* (2005).

64. Buehler Sum-Met, The Science Behind Materials Preparation: A Guide to Materials Preparation and Analysis: Low Melting Point Metals, pp. 38-39 (2004).

65. D. Phifer, FEI Company, *private communication*, March 2007.

66. JEDEC STANDARD: JESD22-B117, *"Solder Ball Shear,"* (2006).

67. P. Vianco, *"An overview of surface finishes and their role in pcb solderability and solder joint performance,"* Circuit World, **25** (**1**), 6-24 (1998).

68. D. Ma, W. D. Wang and S. K. Lahiri, "*Scallop formation and dissolution of Cu-Sn intermetallic compound during solder reflow,*" J. App. Phys., **91** (**5**), 3312-3317 (2002).

69. H.K. Kim and K. N. Tu, "*Rate of consumption of Cu in soldering accompanied by ripening,*" App. Phys. Lett., **67** (**14**), 2002-2004 (1995).

70. C.J. Smithells and E.A. Brandes, Metals Reference Book, 5th ed. (Butterworth, USA, 1976), p. 194.

71. K. Zeng, V. Vuorinen and J.K. Kivilahti, *"Intermetallic reactions between lead-free SnAgCu solder and Ni(P)/Au surface finish on PWBs,"* Procs. Electronic Components and Tech. Conf., 2001, 693-698.

72. F. Zhang, M. Li, C.C. Chum and Z.C. Shao, *"Effects of substrate metallization on solder/under-bump metallization interfacial reactions in flip-chip packages during multiple reflow cycles,"* J. Electron. Mater., **32** (**3**), 123-130 (2003).

73. Minitab Website (2007). *Paired t-Test* [Online]. Available at www.minitab.com (accessed 2 June 2007).

APPENDIX A

Measured Pad Diameters of the ImAg, ENIG, and OSP-coated Specimens

Table A1. Pad diameter readings for the ImAg-coated specimens.

Pad Diameter (μm)				
Sample 1	Sample 2	Sample 3	Sample 4	Sample 5
549	544	538	537	563
552	547	533	541	552
531	546	533	535	550
538	537	527	538	542
537	549	532	535	550
540	537	538	533	546
542	533	532	528	552
545	535	540	531	550
541	540	528	533	544
533	541	533	532	550
541	533	545	541	554
549	536	537	537	544
544	536	537	537	547
541	530	538	531	552
540	535	535	531	551
540	533	545	536	538
551	537	545	535	546
546	527	541	533	547
550	542	541	537	538
537	536	538	537	542

Table A2. Pad diameter readings for the ENIG-coated specimens.

Pad Diameter (μm)				
Sample 1	Sample 2	Sample 3	Sample 4	Sample 5
547	544	544	542	545
544	542	544	536	549
544	537	544	544	552
546	538	541	538	552
544	540	540	545	554
545	538	547	537	558
550	546	547	544	555
545	547	547	542	560
550	547	546	544	561
550	546	546	544	561
541	541	537	542	555
545	542	538	538	559
546	542	533	538	547
540	542	533	542	547
538	542	533	538	551
538	546	538	542	560
545	550	542	541	559
544	551	533	542	552
540	546	542	541	554
541	549	542	538	550

Table A3. Pad diameter readings for the OSP-coated specimens.

Pad Diameter (μm)				
Sample 1	Sample 2	Sample 3	Sample 4	Sample 5
533	533	538	540	538
533	535	535	533	540
528	531	533	540	545
533	532	538	538	542
533	532	538	537	542
523	540	533	549	551
527	538	538	542	549
528	540	542	546	541
527	538	538	542	549
532	538	545	540	541
533	530	542	542	542
525	526	545	536	541
531	528	546	538	538
532	532	545	536	549
535	535	544	532	546
528	531	540	550	550
528	527	544	545	549
530	535	538	554	551
531	540	542	550	542
533	540	542	551	540

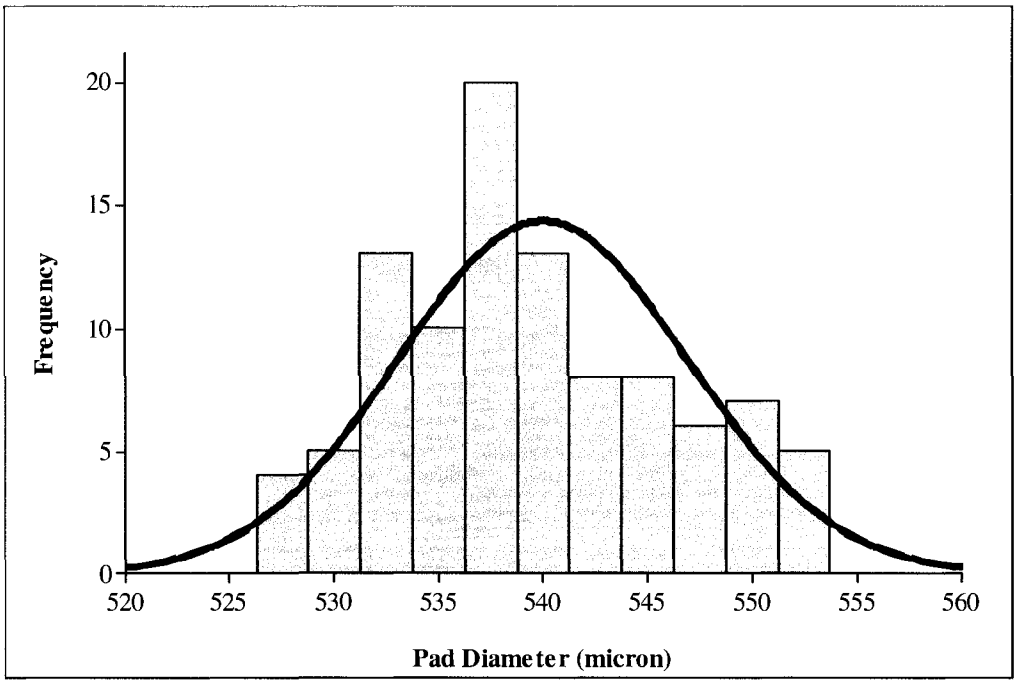

Figure A1. Pad diameter histogram for the ImAg-coated specimens.

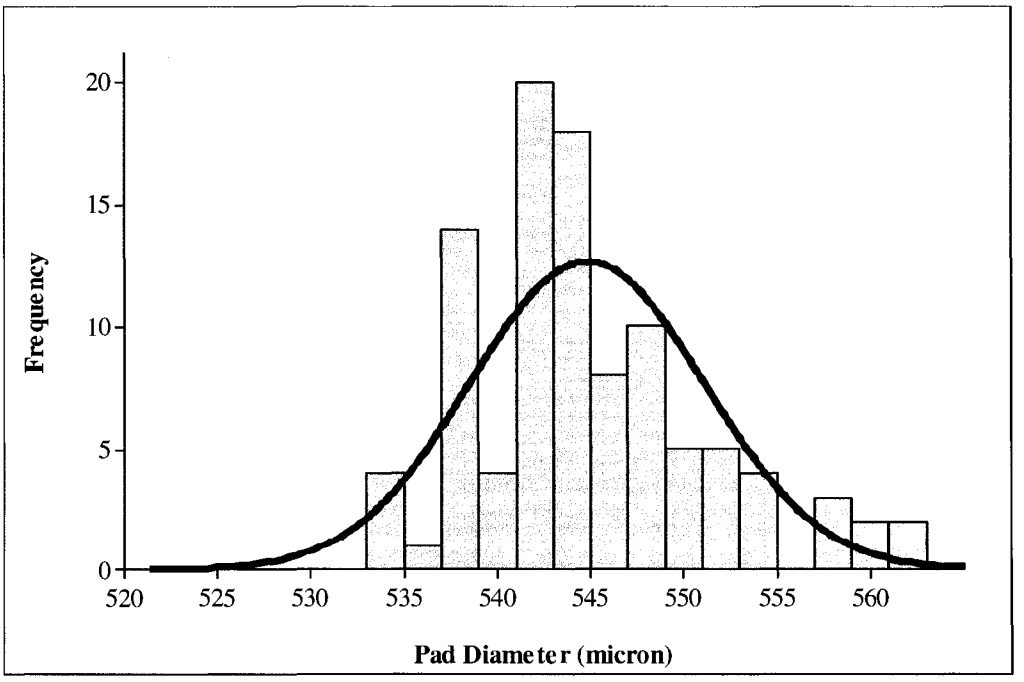

Figure A2. Pad diameter histogram for the ENIG-coated specimens.

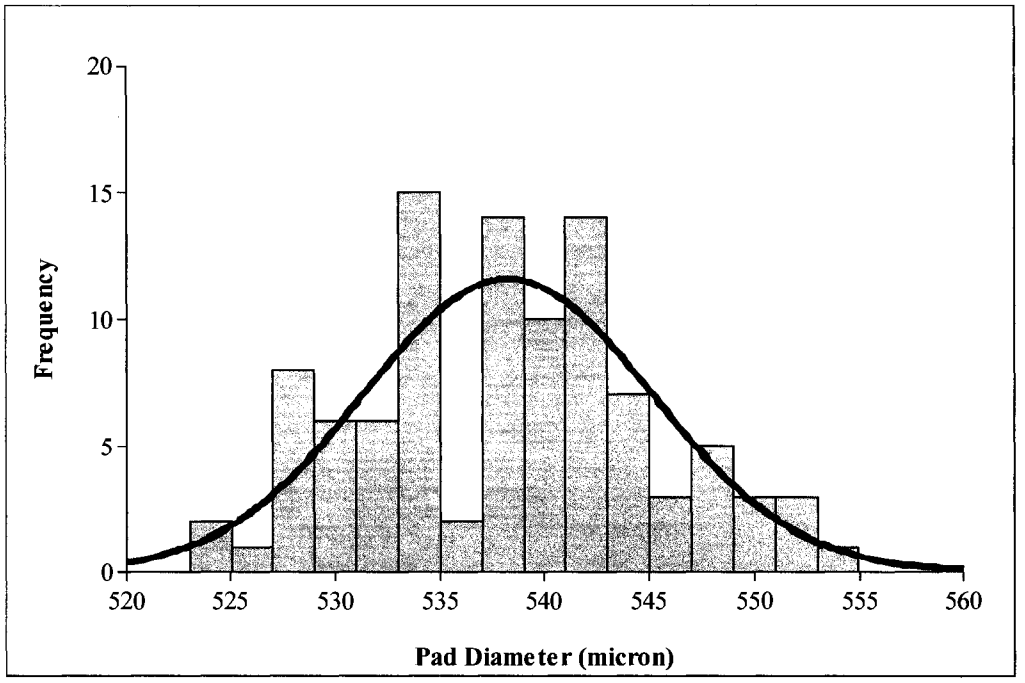

Figure A3. Pad diameter histogram for the OSP-coated specimens.

APPENDIX B

Thickness of the IMCs in the ImAg, ENIG, and OSP-coated Specimens

Table B1. Thickness of the IMCs found in the ImAg-coated specimens as a function of aging time.

Aging Time (days)	IMC Thickness (μm)	Aging Time (days)	IMC Thickness (μm)	Aging Time (days)	IMC Thickness (μm)
0	2.8	10	5.0	30	7.2
	3.3		5.0		7.2
	3.3		5.0		7.2
	3.3		5.6		7.8
	3.3		5.6		7.8
	3.9		5.6		7.8
	3.9		5.6		7.8
	3.9		6.1		7.8
	3.9		6.7		7.8
	3.9		6.7		7.8
	3.9		6.1		7.8
	3.9		6.7		7.8
	3.9		6.7		8.9
	3.9		7.2		8.9
	4.4		7.2		8.9
	5.0		7.2		9.4
	5.0		7.8		10.0
	5.0		7.8		10.6
	5.0		7.8		11.1
	5.0		7.8		11.1
5	3.9	20	6.7		
	3.9		7.2		
	4.4		7.2		
	5.0		7.2		
	5.0		7.2		
	5.0		7.2		
	5.0		7.2		
	5.6		7.2		
	5.6		7.2		
	5.6		7.2		
	5.6		7.2		
	5.6		7.8		
	5.6		7.8		
	5.6		7.8		
	5.6		7.8		
	5.6		7.8		
	5.6		8.3		
	6.1		8.9		
	6.1		8.9		
	6.7		12.8		

Table B2. Thickness of the IMCs found in the ENIG-coated specimens as a function of aging time.

Aging Time (days)	IMC Thickness (μm)	Aging Time (days)	IMC Thickness (μm)	Aging Time (days)	IMC Thickness (μm)
0	2.7	10	3.8	30	5.9
	2.7		3.8		6.5
	2.7		4.3		7.0
	3.2		4.3		7.0
	3.2		4.3		7.0
	3.2		4.9		7.6
	3.8		4.9		7.6
	3.8		5.4		8.1
	3.8		5.4		8.1
	3.8		5.4		8.1
	3.8		5.4		8.1
	3.8		5.4		8.6
	3.8		5.4		8.6
	3.8		5.9		8.6
	3.8		5.9		8.3
	4.3		5.9		9.2
	4.9		5.9		10.8
	4.9		6.5		10.3
	4.9		6.5		10.8
	4.9		6.5		10.8
5	3.2	20	5.4		
	3.8		5.4		
	3.8		5.4		
	3.8		5.9		
	3.8		5.9		
	3.8		6.5		
	4.3		6.5		
	4.3		6.5		
	4.9		7.0		
	4.9		7.0		
	4.3		7.0		
	4.9		7.0		
	4.9		7.6		
	4.9		7.6		
	4.9		7.6		
	5.4		7.6		
	5.4		8.1		
	5.4		8.1		
	5.4		8.6		
	5.9		8.6		

Table B3. Thickness of the IMCs found in the OSP-coated specimens as a function of aging time.

Aging Time (days)	IMC Thickness (μm)	Aging Time (days)	IMC Thickness (μm)	Aging Time (days)	IMC Thickness (μm)
0	3.0	10	4.3	30	7.0
	3.0		5.2		7.4
	3.0		5.2		7.8
	3.5		5.2		7.8
	3.5		6.1		8.3
	3.5		6.1		8.3
	3.5		6.1		8.3
	3.9		6.5		8.3
	3.9		6.5		8.3
	3.9		7.0		8.7
	3.9		7.0		8.7
	4.3		7.0		8.7
	4.3		7.0		9.1
	4.3		7.4		9.1
	4.3		7.4		9.1
	4.8		7.8		10.0
	4.8		7.8		10.4
	4.8		7.8		10.9
	5.2		8.3		10.9
	5.2		8.7		11.3
5	3.5	20	7.0		
	4.8		7.0		
	4.8		7.0		
	4.8		7.0		
	5.2		7.4		
	5.2		7.4		
	5.2		7.8		
	5.2		7.8		
	5.2		7.8		
	5.2		7.8		
	5.7		7.8		
	5.7		7.8		
	6.1		8.3		
	6.1		8.3		
	6.1		8.3		
	6.1		8.7		
	6.1		8.7		
	6.1		9.1		
	6.1		9.6		
	6.5		10.0		

APPENDIX C

Ball Shear Data for the ImAg, ENIG, and OSP-coated Specimens

Table C1. Ball shear data for the ImAg-coated specimens at a shear rate of 200 μm/sec.

Aging Time (days)	Ball Shear Force (gf)	Aging Time (days)	Ball Shear Force (gf)	Aging Time (days)	Ball Shear Force (gf)
0	915	10	1065	30	950
	880		1020		995
	770		1100		870
	885		950		865
	915		1000		1005
	910		960		920
	910		880		785
	950		1020		865
	745		865		875
	960		905		870
	1080		955		985
	1000		845		895
	905		1025		945
	915		825		910
	940		945		1000
	1030		935		885
	985		890		925
	930		865		800
	985		800		860
	870		860		960
5	870	20	825		
	765		755		
	800		850		
	975		815		
	790		700		
	935		985		
	935		935		
	820		825		
	1030		985		
	755		875		
	820		915		
	770		815		
	670		985		
	915		935		
	945		990		
	750		960		
	865		905		
	955		1045		
	700		1030		
	730		1105		

* Ball shear failure mode for all measurements is pad lift.

Table C2. Ball shear data for the ENIG-coated specimens at a shear rate of 200 μm/sec.

Aging Time (days)	Ball Shear Force (gf)	Aging Time (days)	Ball Shear Force (gf)	Aging Time (days)	Ball Shear Force (gf)
0	1100	10	1185	30	945
	1080		1130		870
	1180		1085		940
	1185		870		945
	1020		1045		1030
	1085		1025		920
	1100		1065		850
	1060		865		840
	1025		925		880
	1195		1015		840
	990		945		910
	1090		1005		975
	1135		880		845
	1020		1000		975
	1065		1050		1060
	1015		1010		800
	1170		1040		995
	990		990		1070
	1075		915		795
	1010		915		950
5	**1050**	20	935		
	950		910		
	600		985		
	955		1050		
	865		995		
	930		1095		
	865		1045		
	985		1010		
	795		1045		
	740		1040		
	980		1135		
	1120		880		
	990		960		
	1095		1045		
	1115		1085		
	1120		1085		
	1040		1020		
	915		1015		
	965		1155		
	1170		960		

* Numbers in bold denote ductile failure mode; otherwise failure mode is pad lift.

Table C3. Ball shear data for the OSP-coated specimens at a shear rate of 200 μm/sec.

Aging Time (days)	Ball Shear Force (gf)	Aging Time (days)	Ball Shear Force (gf)	Aging Time (days)	Ball Shear Force (gf)
0	850	10	1020	30	875
	875		1005		910
	865		1090		960
	890		1025		945
	945		985		965
	935		970		920
	1120		985		1030
	930		960		905
	1100		965		975
	1135		875		855
	1070		930		915
	1005		840		925
	1025		855		940
	930		1040		855
	955		995		975
	915		1010		1045
	950		1035		950
	1010		1055		950
	910		950		970
	975		1025		995
5	1120	20	930		
	1165		985		
	1090		1005		
	1020		945		
	1200		915		
	905		885		
	950		860		
	970		925		
	1055		1040		
	950		985		
	995		930		
	945		975		
	1015		960		
	1105		970		
	1085		885		
	1130		995		
	1110		1060		
	1205		955		
	1215		1010		
	1075		935		

* Ball shear failure mode for all measurements is pad lift.

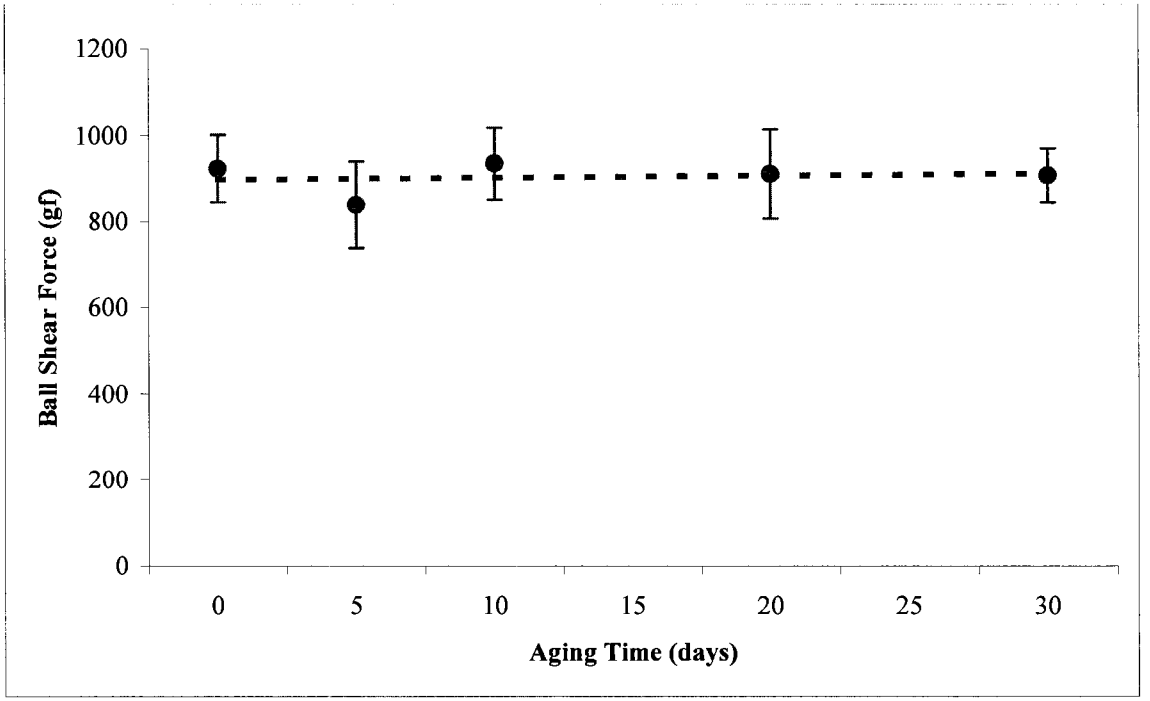

Figure C1. Ball shear force as a function of aging time for the ImAg-coated specimens.

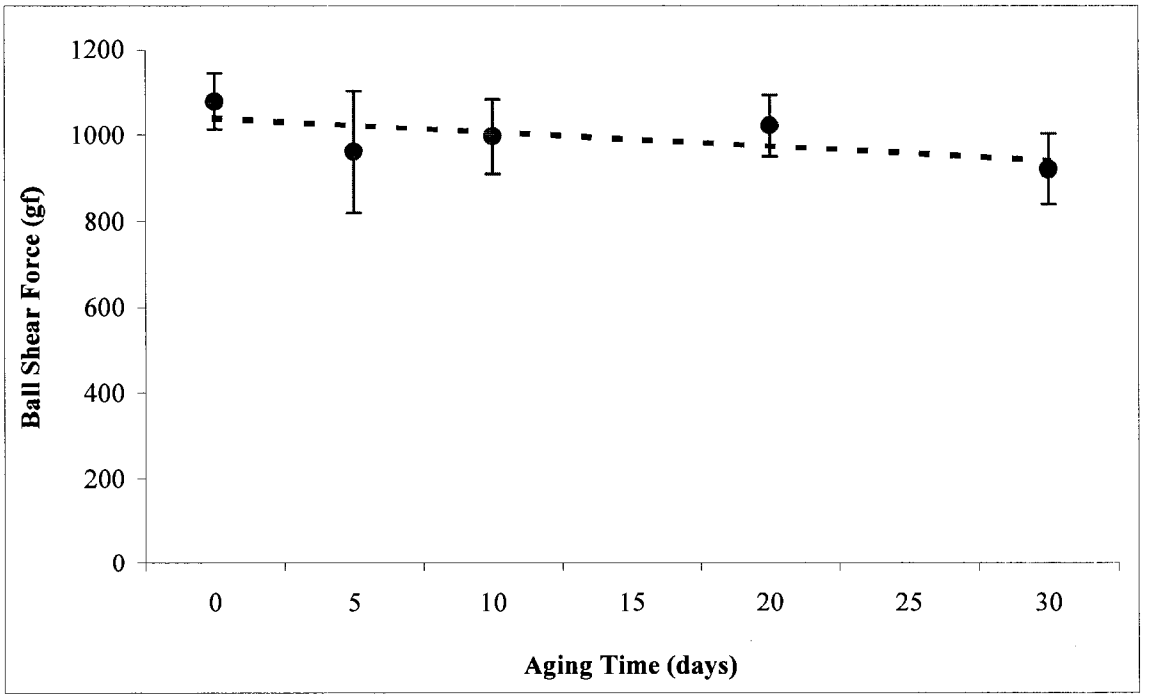

Figure C2. Ball shear force as a function of aging time for the ENIG-coated specimens.

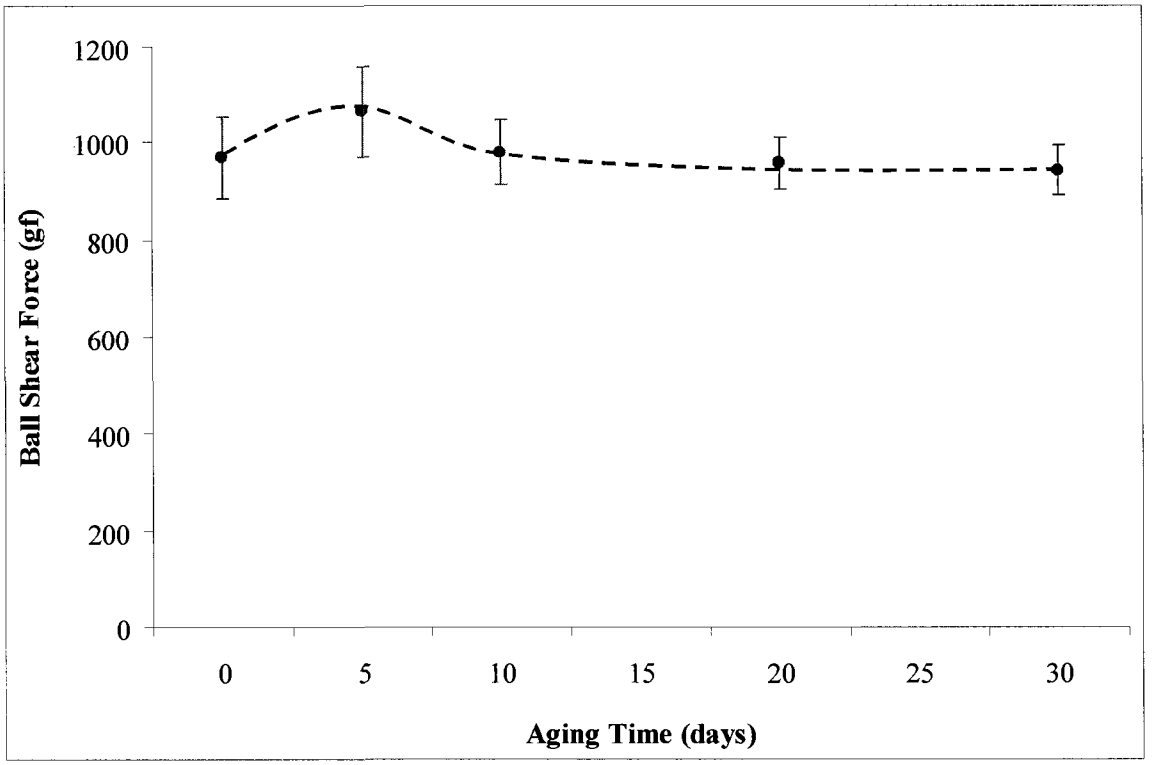

Figure C3. Ball shear force as a function of aging time for the OSP-coated specimens.

Paired Student t-Test

A paired student t-test is used to test the mean difference between paired observations (such as before and after measurements) when the paired differences follow a normal distribution [73]. This test matches responses that are dependent or related in a pairwise manner, which allows the investigator to account for variability between the pairs. This usually results in a smaller error, thus increasing the sensitivity of the hypothesis test or confidence interval.

To determine statistical significance, the p-test value is calculated. The p-value determines if it is appropriate to reject the null hypothesis and accept the alternative hypothesis instead [73]. It has values in the range of 0 to 1. When performing this test, an α-value is usually chosen. If the p-value of the test-statistic is less than the α-value, then the null hypothesis is rejected, and the alternative hypothesis is accepted. If the p-value is greater than the α-value, the null hypothesis is accepted.

Student t-test Results for the ImAg, ENIG, and OSP-coated Specimens

Table C4. Paired t-test between ImAg (no aging) and ImAg (5-day aging).

	N	Mean	StDev	SE Mean
Ag (0)	20	924.0	77.5	17.3
Ag (5)	20	839.8	101.3	22.7
Difference	20	84.3	146.8	32.8
95% Confidence Level for mean difference: (15.6, 152.9)				
T-Test of mean difference = 0 (vs not = 0): T-Value = 2.57, P-Value = 0.019				

Table C5. Paired t-test between ImAg (5-day aging) and ImAg (10-day aging).

	N	Mean	StDev	SE Mean
Ag (5)	20	839.8	101.3	22.7
Ag (10)	20	935.5	83.4	18.6
Difference	20	-95.8	140.6	31.4
95% CI for mean difference: (-161.6, -29.9)				
T-Test of mean difference = 0 (vs not = 0): T-Value = -3.05, P-Value = 0.007				

Table C6. Paired t-test between ImAg (10-day aging) and ImAg (20-day aging).

	N	Mean	StDev	SE Mean
Ag (10)	20	935.5	83.4	18.6
Ag (20)	20	911.8	103.4	23.1
Difference	20	23.7	163.6	36.6
95% CI for mean difference: (-52.8, 100.3)				
T-Test of mean difference = 0 (vs not = 0): T-Value = 0.65, P-Value = 0.524				

Table C7. Paired t-test between ImAg (20-day aging) and ImAg (30-day aging).

	N	Mean	StDev	SE Mean
Ag (20)	20	911.8	103.4	23.1
Ag (30)	20	908.3	62.9	14.1
Difference	20	3.5	133.6	29.9
95% CI for mean difference: (-59.0, 66.0)				
T-Test of mean difference = 0 (vs not = 0): T-Value = 0.12, P-Value = 0.908				

Table C8. Paired t-test between ENIG (no aging) and ENIG (5-day aging).

	N	Mean	StDev	SE Mean
ENIG (0)	20	1079.5	65.9	14.7
ENIG (5)	20	962.3	141.5	31.6
Difference	20	117.3	178.3	39.9
95% CI for mean difference: (33.8, 200.7)				
T-Test of mean difference = 0 (vs not = 0): T-Value = 2.94, P-Value = 0.008				

Table C9. Paired t-test between ENIG (5-day aging) and ENIG (10-day aging).

	N	Mean	StDev	SE Mean
ENIG (5)	20	962.3	141.5	31.6
ENIG (10)	20	998.0	86.5	19.4
Difference	20	-35.7	174.9	39.1
95% CI for mean difference: (-117.6, 46.1)				
T-Test of mean difference = 0 (vs not = 0): T-Value = -0.91, P-Value = 0.372				

Table C10. Paired t-test between ENIG (10-day aging) and ENIG (20-day aging).

	N	Mean	StDev	SE Mean
ENIG (10)	20	998.0	86.5	19.4
ENIG (20)	20	1022.5	71.3	16.0
Difference	20	-24.5	128.3	28.7
95% CI for mean difference: (-84.5, 35.5)				
T-Test of mean difference = 0 (vs not = 0): T-Value = -0.85, P-Value = 0.404				

Table C11. Paired t-test between ENIG (20-day aging) and ENIG (30-day aging).

	N	Mean	StDev	SE Mean
ENIG (20)	20	1022.5	71.3	16.0
ENIG (30)	20	921.8	81.4	18.2
Difference	20	100.8	119.4	26.7
95% CI for mean difference: (44.9, 156.6)				
T-Test of mean difference = 0 (vs not = 0): T-Value = 3.77, P-Value = 0.001				

Table C12. Paired t-test between OSP (no aging) and OSP (5-day aging).

	N	Mean	StDev	SE Mean
OSP (0)	20	969.5	84.5	18.9
OSP (5)	20	1065.3	93.8	21.0
Difference	20	-95.8	152.8	34.2
95% CI for mean difference: (-167.3, -24.2)				
T-Test of mean difference = 0 (vs not = 0): T-Value = -2.80, P-Value = 0.011				

Table C13. Paired t-test between OSP (5-day aging) and OSP (10-day aging).

	N	Mean	StDev	SE Mean
OSP (5)	20	1065.3	93.8	21.0
OSP (10)	20	980.8	65.8	14.7
Difference	20	84.5	81.7	18.3
95% CI for mean difference: (46.3, 122.7)				
T-Test of mean difference = 0 (vs not = 0): T-Value = 4.63, P-Value = 0.000				

Table C14. Paired t-test between OSP (10-day aging) and OSP (20-day aging).

	N	Mean	StDev	SE Mean
OSP (10)	20	980.8	65.8	14.7
OSP (20)	20	957.5	51.7	11.6
Difference	20	23.3	81.7	18.3
95% CI for mean difference: (-15.0, 61.5)				
T-Test of mean difference = 0 (vs not = 0): T-Value = 1.27, P-Value = 0.218				

Table C15. Paired t-test between OSP (20-day aging) and OSP (30-day aging).

	N	Mean	StDev	SE Mean
OSP (20)	20	957.5	51.7	11.6
OSP (30)	20	943.0	50.6	11.3
Difference	20	14.5	74.3	16.6
95% CI for mean difference: (-20.3, 49.3)				
T-Test of mean difference = 0 (vs not = 0): T-Value = 0.87, P-Value = 0.394				